FINAL REPORT

for

INTERPRETATION OF BAROCLINIC SYSTEMS
AND WIND FIELDS
AS OBSERVED BY NIMBUS II MRIR

(January 1967 - February 1968)

Contract No. NAS5-10334
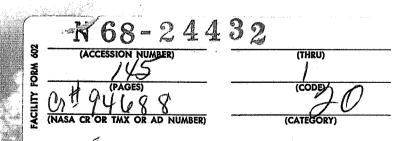
Donald W. Beran

Earl S. Merritt

David T. Chang

ALLIED RESEARCH ASSOCIATES, INC.
VIRGINIA ROAD   CONCORD, MASSACHUSETTS 01742

Goddard Space Flight Center
Greenbelt, Maryland

FINAL REPORT

INTERPRETATION OF BAROCLINIC SYSTEMS
AND WIND FIELDS
AS OBSERVED BY NIMBUS II MRIR

(January 1967 - February 1968)

Contract No. NAS5-10334

Goddard Space Flight Center

Contracting Officer: Mr. E.S. McLean

Technical Monitor: Mr. W. Bandeen

ALLIED RESEARCH ASSOCIATES, INC.
VIRGINIA ROAD   CONCORD, MASSACHUSETTS 01742

Project Manager: E.S. Merritt

Goddard Space Flight Center
Greenbelt, Maryland

FOREWORD

ABSTRACT

Detailed studies of the characteristics of the Nimbus II Medium Resolution Infrared Radiometer (MRIR) data, particularly from Channels 1 and 3 (6.4-6.9μ H_2O and 14-16μ CO_2) have revealed several important operational applications. These include:

1. Identification through the Channel 1 (6.4-6.9μ H_2O) areas of active descending motions in the upper troposphere and lower stratosphere which are frequently associated with jet streams and deepening upper tropospheric cyclones in both the extratropical and subtropical regions. These areas are identified by warm 6.4-6.9μ T_{bb} values in variously shaped patterns.

2. Identification through the conjoint use of both Channel 1 (6.4-6.9μ H_2O) and Channel 3 (14-16μ CO_2) data of intense jet stream locations in the extratropics.

3. Delineation of cirrus cloud areas not readily observed in either the television or atmospheric "window" (10-11μ) data. Channel 1 (6.4-6.9μ H_2O) T_{bb} values between 235°K and 240°K were frequently observed to be related to extensive independent cirrus areas. This information appears useful to early identification of the cirriform canopy in tropical storms.

Secondary findings reported on include: (1) the use of multichannel color presentations utilizing the 6.4-6.9μ H_2O, 10-11μ "window" and 0.2-4.0μ reflected data from the MRIR to assist in clear area delineation, locating cirrus blow-off from large cumulonimbus conglomerates and synoptic scale storm systems; and (2) a potential application of the 6.4-6.9μ H_2O data to delineation of areas of clear air turbulence, CAT.

TABLE OF CONTENTS

TABLE OF CONTENTS (cont)

LIST OF FIGURES

LIST OF FIGURES (cont)

LIST OF FIGURES (cont)

1. INTRODUCTION

Baroclinic weather system developments are frequently accompanied by dramatic changes in the upper tropospheric and lower stratospheric temperature and moisture distributions. The primary objective of the studies reported herein is the evaluation of the hypothesis that satellite radiometric measurements in the 6.3μ "H_2O" and 15μ "CO_2" atmospheric absorption bands can be used to detect these dramatic temperature and moisture changes. Satellite mapping of these changes may permit direct inference of the location and intensity of major baroclinic developments.

Studies based on TIROS measurements have demonstrated that satellite measurements in the 6.3μ H_2O and 15μ CO_2 spectral bands can detect atmospheric moisture and temperature variations. Moller and Raschke (1964) showed, in analyses of TIROS IV data, that the 6.3μ H_2O observation may be useful in moisture determination. Kennedy (1966) and others have demonstrated with TIROS VII 15μ CO_2 observations the ability to map the mean temperature of the lower stratosphere. Merritt and Chang (1965) showed that the TIROS VII 15μ CO_2 observations could detect the lower stratospheric warming associated with major baroclinic systems, e.g., jet streams and extratropical cyclones. The Nimbus II satellite offered the first opportunity to examine the hypothesis through the conjoint use of both the 6.4-6.9μ H_2O and 14-16μ CO_2 channels of the five-channel Medium Resolution Infrared Radiometer (MRIR).

The following sections of this report will: (1) examine the characteristics of the 6.4-6.9μ H_2O and 14-16μ CO_2 channels as they may influence the utilization of the data; this examination includes an evaluation of the influence of temperature and moisture changes as well as the influence of cloudiness, particularly thin cirrus on the observations, (2) present illustrative examples and models which demonstrate the validity of the two channel hypothesis to the diagnosis of jet streams, and extratropical and tropical baroclinic cyclones and (3) suggest auxilliary applications for the 6.4-6.9μ H_2O data to cirrus cloud delineation, clear air turbulence (CAT) area delineation and 700-400 mb precipitable water determination.

1

2. CHARACTERISTICS OF THE RADIOMETRIC MEASUREMENTS OF NIMBUS II

2.1 The Medium Resolution Infrared Radiometer (MRIR) Experiment

Nimbus II was launched into a nearly circular polar orbit on 15 May 1966. The satellite was north-bound over the daylight portion of the earth, and southbound during night. The orbit was nearly sun synchronous with ascending nodes occurring at 32 minutes before noon local mean solar time.

Nimbus II had onboard a number of meteorological experiments. In addition to an Advance Vidicon Camera System (AVCS), an Automatic Picture Transmission (APT) Camera, and a scanning High Resolution Infrared Radiometer (HRIR), the satellite carried a Medium Resolution Infrared Radiometer (MRIR). This last experiment was not on board Nimbus I.

The MRIR five channel radiometer system made simultaneous measurements in the following five spectral intervals:

$6.4-6.9\mu$	(water vapor absorption)
$10-11\mu$	(atmospheric window)
$14-16\mu$	(carbon dioxide absorption)
$5-30\mu$	("total" IR)
$0.2-4\mu$	(reflected solar radiation)

The radiometer had an instantaneous field of view of 5 x 5 milliradians, corresponding to a resolution on the surface of the earth of about 60 x 60 km at the satellite subpoint. A rotating mirror provided angular scanning perpendicular to the heading line of the satellite.

Besides the usual analog and digital format, the data from the MRIR are also available in a grey scale pictorial presentation. As part of the "on-line" processing, the data from the five channels are separately displayed on a cathode ray tube photo display together with a geographic reference grid. A calibration grey scale is also displayed coincidentally with the data. The CRT display is then photographed pro- viding a permanent record of the data. Examples of such presentations are found in subsequent sections of this report.

As stated in Section 1, this study is concerned primarily with the application of 6.4-6.9µ and 14-16µ data of the MRIR to meteorological analysis. The physical relationships between the measurements made by these two channels and meteorological parameters are analyzed in detail in this section. These analyses provide the bases for interpretation presented in subsequent sections of this report.

2.2 Equation of Radiation Transfer

The interpretation of satellite radiometric measurements is based on an equation of radiative transfer through the atmosphere. The energy received by a satellite radiometer is dependent on the radiation emitted by the earth and atmosphere, and by the absorption of this radiation during its passage through the atmosphere to the satellite. These processes may be expressed in a single equation:

$$\overline{N} = \frac{1}{\pi} \int_{\lambda=0}^{\lambda=\infty} \phi(\lambda)\tau_s(\lambda)B(\lambda, T_s)d\lambda$$

$$+ \frac{1}{\pi} \int_{\lambda=0}^{\lambda=\infty} \int_{z=0}^{z=\infty} \phi(\lambda) \frac{\partial\tau(\lambda, z)}{\partial z} B(\lambda, T(z))dzd\lambda \tag{1}$$

where:

$\overline{N}$	=	radiance measured by the satellite radiometer (effective radiance)
$\phi(\lambda)$	=	filter function corresponding to the channel in question
$\tau_s(\lambda)$	=	transmissivity of the atmosphere above the radiating surface
$\tau(\lambda, z)$	=	transmissivity of the atmosphere from level z upwards
$B(\lambda, T)$	=	Planck function
T_s	=	absolute temperature of the underlying radiating surface
$T(z)$	=	absolute temperature of the atmosphere at level z.

In Equation (1), the radiance contributions from the underlying surfaces, such as the surfaces of the earth or of thick clouds, and from the atmosphere are explicitly given. In the case of measurements made in an ideal atmospheric window,

4

the second term, describing the contribution from the atmosphere, vanishes. The radiance measured is then directly proportional to the emitting temperature of the underlying surface. While the 10-11μ region does not constitute a perfect window, nor do natural surfaces radiate as perfect blackbodies, it has often been assumed that such measurements correspond to surface (or cloud top) temperatures.

The interpretation of absorption band measurements, such as those made in the 6.4-6.9μ and 14-16μ regions, is less straightforward. The second term in Equation (1) contains the two terms, $B(\lambda, T(z))$ and $\partial \tau(\lambda, z)/\partial z$, which are dependent on the vertical distributions of atmospheric temperature and of the absorbing gas, both of which may be unknown. In the case of the carbon dioxide absorption band measurements, the vertical distribution of carbon dioxide may be assumed known, since it is a well mixed gas. $\partial \tau(\lambda, z)/\partial z$ can then be determined. The vertical distribution of water vapor, on the other hand, is highly variable, introducing further complications into the interpretation of measurements made by the 6.4-6.9μ channel.

In any event, the interpretation of absorption band measurements can be made from parametric analyses of Equation (1). In these analyses, Equation (1) is solved for a number of model atmospheres. The dependence of $\overline{N}$, and of

$$\overline{N}(z) = \frac{1}{\pi} \int_{\lambda=0}^{\lambda=\infty} \phi(\lambda) B(\lambda, T(z)) \frac{\partial \tau(\lambda, z)}{\partial z} d\lambda \qquad (2)$$

on variations in atmospheric structure are then determined. (The term, $\overline{N}(z)$, describes the radiance contributions from an infinitessimal atmospheric layer located at level z, and is known as the weighting function.)

Before proceeding to a discussion of the analysis of $\overline{N}(z)$, it is necessary to define a parameter known as the Effective Blackbody Temperature, denoted by T_{bb}. This parameter is defined as the temperature of an equivalent blackbody which would produce the same response as the measured radiance. If $\overline{N}$ is the radiance measured by the radiometer, then

$$\overline{N} = \frac{1}{\pi} \int_{\lambda=0}^{\lambda=\infty} \phi(\lambda) \tau_s(\lambda) B(\lambda, T_s) d\lambda + \frac{1}{\pi} \int_{\lambda=0}^{\lambda=\infty} \int_{z=0}^{z=\infty} \phi(\lambda) \frac{\partial \tau(\lambda, z)}{\partial z} B(\lambda, T(z)) dz d\lambda$$

$$= \frac{1}{\pi} \int_{\lambda=0}^{\lambda=\infty} \phi(\lambda) B(\lambda, T_{bb}) d\lambda$$

where

$$T_{bb} = \text{effective blackbody temperature}$$

Since $B(\lambda)$ is a known function of temperature for a perfect blackbody, and $\phi(\lambda)$ is a known function for a given radiometer, every measured $\overline{N}$ corresponds to a unique value of T_{bb}. N and T_{bb} may therefore be used interchangeably to specify the measured values.

2.3 Analysis of Weighting Functions, $\overline{N}(z)$

2.3.1 Computation Scheme
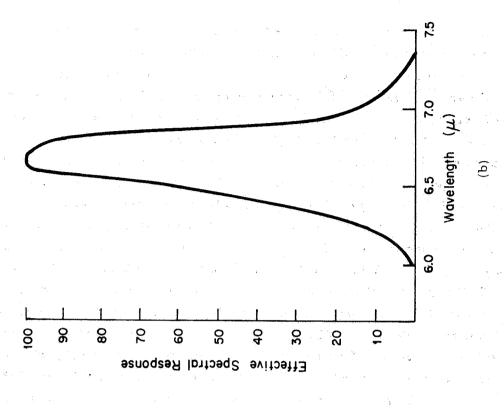
Computer programs were developed for the integration of Equation (1) to obtain $\overline{N}(z)$, $\overline{N}$, and T_{bb} for the 6.4-6.9μ and 14-16μ channels. The atmosphere was assumed to be stratified into layers of 1 km in thickness. The lower boundary was assumed to be a blackbody surface located at $z=0$ (the surface of the earth) or at $z=R$, where R is cloud top height. For the 14-16μ computations, the top of the atmosphere was assumed to be at $z = 50$ km. In the case of the 6.4-6.9μ calculations, the top of the atmosphere was set at 35 km. This was dictated by the lack of special moisture soundings above this level.
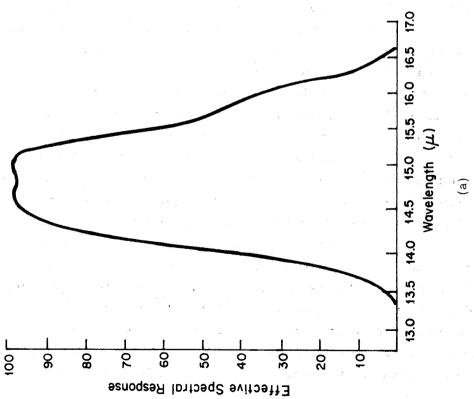
The transmissivity functions used in the computations were based on the data given in Moller and Raschke (1964). The filter functions, $\phi(\lambda)$, for the two channels were taken from the Nimbus II User's Guide and are shown in Figure 2-1. All computations were performed on the Bolt, Beranek and Newman Time Share Computer, with terminal keyboard and teletype facilities located at Allied Research Associates.

2.4 Water Vapor Channel Computations

2.4.1 An Example of T_{bb} Values for the 6.4-6.9μ (Water Vapor) Channel Computed from Radiosonde Data

Radiosonde data, concurrent with the MRIR data, provided a means of checking the accuracy of the computation scheme discussed in the previous section. While no independent data for checking computed weighting functions existed, it was assumed that, if the program could accurately reproduce the measured blackbody temperatures,

Figure 2-1 Effective Spectral Response Functions for the 14-16μ (a) and 6.4-6.9μ (b) Channels of the MRIR

the computed weighting functions were most likely correct. A number of these checks were performed, using United States and Canadian radiosonde data. In the following, the results of one particular set of computations are discussed.

Figure 2-2 shows a temperature and mixing ratio cross section from Great Falls (GTF), Montana, to Flint (FNT), Michigan. The data were taken from radiosonde data at 1200 GMT, 28 June 1966. The analysis shows that horizontal variations in temperature were minor. The mixing ratios, on the other hand, show a relatively dry upper troposphere between Bismark (BIS), North Dakota, and St. Cloud (STC), Minnesota, with the 0.5 g/kg line dipping to below 500 mb at STC. The soundings at Green Bay (GRB), Wisconsin, and at FNT, indicated saturation below, and clouds with tops at, approximately 470 mb and 450 mb, respectively. Surface observations at 1200 GMT and 1800 GMT reported that the area extending from GTF to BIS was clear. STC reported total obscuration while GRB had middle and low clouds.
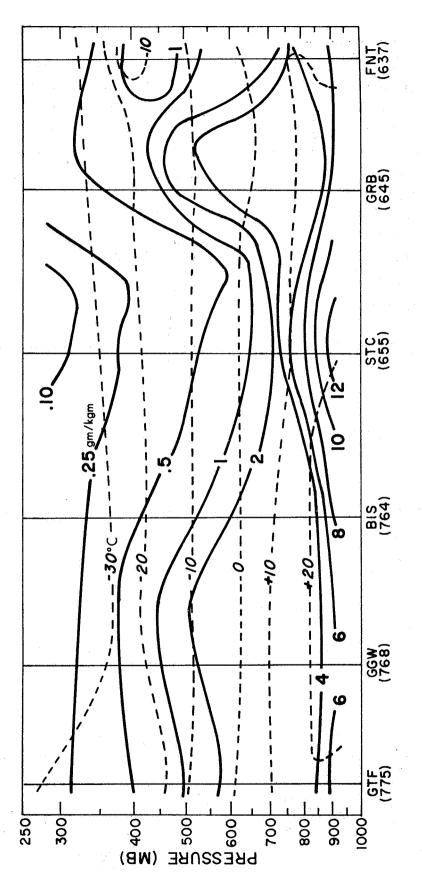
Figure 2-3 shows the 10-11μ channel T_{bb} values along the same cross section taken from orbit 592 (1600 GMT, 28 June 1966). These temperatures are in agreement with an apparently clear area that extended from GTF to BIS, with low cloudiness (~750 mb) over STC. The window channel temperatures over GRB and FNT give derived cloud top heights approximating those deduced from the radiosonde data.

Figure 2-3b shows the measured 6.4-6.9μ (H_2O) channel blackbody temperatures. It is interesting to note that this curve reflects the 0.5 g/kg line shown in Figure 2-2. The warmest temperatures are in the dry area between BIS and GRB, while colder temperatures are found over the apparently cloud free region between GTF and BIS, which has a uniform window channel temperature of 305°K.
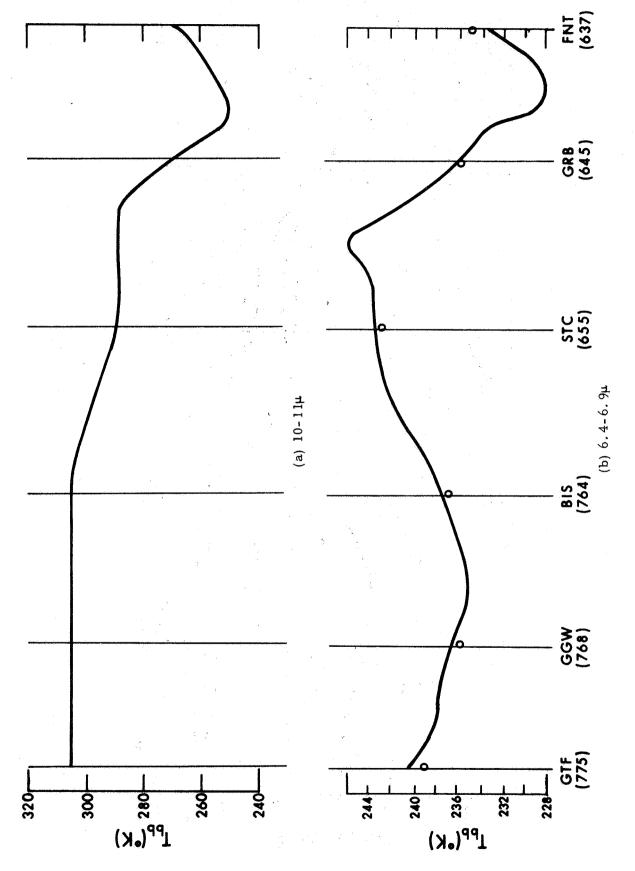
A further check of the 0000 GMT, 29 June radiosonde data for the stations along the cross section show no significant changes in either the moisture or temperature distribution. It was concluded, therefore, that the time difference between the satellite data and the 1200 GMT radiosonde data would not be a critical factor in the comparison of computed and observed 6.4-6.9μ channel temperatures.

Figure 2-4 shows the weighting functions and effective blackbody temperatures computed from the data shown in Figure 2-2. The computed T_{bb} values compare rather well with the measured values.
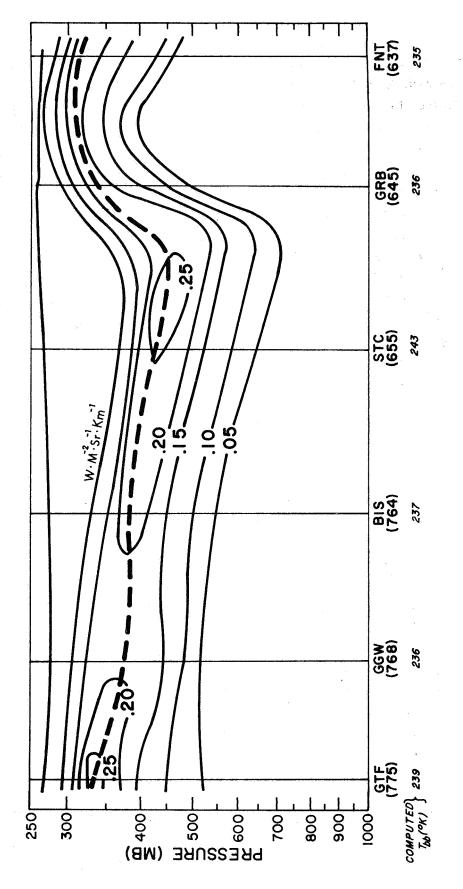
The analysis of the weighting function, $\overline{N}(z)$ in Figure 2-4 demonstrates the effect of moisture in the various layers of the atmosphere on the measured blackbody temperatures. (The isolines shown are in units of watts·m^{-2}· sr^{-1}· km^{-1} .) The heavy dashed line shows the locus of the peaks of the computed weighting functions. The analysis shows that the location of the weighting function peaks (i.e., where

Figure 2-2 Cross Section Analysis of Temperature and Mixing Ratio, 28 June 1966, 1200 GMT

9

Figure 2-3 Nimbus II T_{bb}'s for the 10-11μ (a) and the 6.4-6.9μ (b) Channels, Orbit 592, 28 June 1966, 1600 GMT.

(a) 10-11μ

(b) 6.4-6.9μ

Figure 2-4   Computed 6.3-6.9μ Weighting Functions and T_{bb}'s Based on Analysis Shown in Figure 2-2.

11

$\overline{N}(z)$ is maximum) is highly dependent on the moisture distribution in the upper troposphere and, in at least the case of GTF, on the upper tropospheric temperature profile. In the absence of pronounced temperature departures, the peak of the weighting function is lower over dry regions and higher over moist and/or cloudy regions. GTF, which had an apparently drier upper troposphere than Glasgow (GGW), Montana, had a weighting function peak at a higher altitude than GGW. This was most likely due to the warmer air temperatures above 250 mb.

The 10-11μ T_{bb} at STC was colder than that over BIS. The 6.4-6.9μ T_{bb}, on the other hand, was warmer. These conditions can be explained by reference to the mixing ratio analysis and the cloud reports discussed previously. The lower 10-11μ T_{bb} reflects the presence of low cloud over STC. However, the cloud tops were not high enough to affect the 6.4-6.9μ T_{bb}. This may be seen in the analysis of the weighting function over STC. The contribution from below cloud level was insignificant. On the other hand, the atmosphere above the cloud was extremely dry, giving rise to the warmer 6.4-6.9μ temperature.

The variations in the 6.4-6.9μ T_{bb} between GTF and BIS deserve some discussion. In this instance, both the surface observations and the 10-11μ temperatures tend to support the contention that cloud contamination was negligible. Indeed, the 6.4-6.9μ T_{bb} was approximated by computations which neglected clouds. It should be pointed out, however, that 6.4-6.9μ T_{bb} values between 240°K and 235°K can result from either a moist upper troposphere or the presence of thin cirrus (see Section 2.5). The question of thin cirrus cannot be resolved by reference to ground observation. The inability of ground observers to detect thin cirrus, especially at high sun angles, is fairly well established. The 10-11μ channel measurements are, apparently, not as readily contaminated by thin clouds as the 6.4-6.9μ measurements (see Section 2.4.4). Consequently, it is possible that 6.4-6.9μ T_{bb} values below 240°K reflect the presence of thin cirrus, rather than only an upper troposphere with a high moisture content.

There are three major factors which make it difficult to compare satellite measured T_{bb}'s with computed T_{bb}'s based on radiosonde measurements. These factors are: (a) scale or resolution (b) time differences and (c) the inadequacy of upper tropospheric moisture measurements.

The station spacing of the upper air network, even over the United States, is too great to resolve many of the subsynoptic scale features apparent in the digitized 6.4-6.9μ data. This is especially true in the case of bands of warm T_{bb} values often

found associated with jet streams (see Section 3). These bands are generally on the order of only a few degrees wide. A case in point is that shown in Figure 2-3b, in which the water vapor channel T_{bb} along the section extending from GTF to FNT has been extracted from digitized data and plotted. It is quite apparent that the T_{bb} maximum between STC and GRB, with values in excess of 245°K, is of a smaller scale than can be resolved by the station spacing.

The second difficulty arises from the orbital characteristics of Nimbus II in relation to the times at which regular radiosonde ascents are scheduled. Nimbus II is in a sun synchronous orbit, with satellite passage fixed near local noon and local midnight. Over the Eastern United States, these times correspond to approximately 1600 GMT and 0400 GMT. Radiosonde ascents are normally made at 1200 GMT and 0000 GMT. As a consequence, the time difference between radiosonde data and satellite data, over the United States, can be as much as four hours in the east and six hours in the west. In some instances, this time difference may not be significant, as in the case discussed in Section 2.4.1. On the other hand, when the situation under study involves rapid development, the time difference is a significant factor and must be considered.

The third difficulty encountered is most significant when attempts are made to compare measured T_{bb}'s which are greater than 250°K with computed values. Calculations based on model atmospheres (see Section 2.4.2) show that an extremely dry (with R.H. $<10\%$) upper troposphere (above 500 mb) is necessary to produce water vapor channel T_{bb} values in excess of 250°K. Such high values of T_{bb} were often found to be located in the vicinity of subtropical highs and baroclinic zones, where strong subsidence drying often exists. However, mixing ratios, deduced from the reported frost points, are often either absent or are almost always not low enough to account for the high T_{bb}'s measured by the satellite. Such discrepancies are not unexpected, since the accuracy of radiosonde dew point measurements at low temperatures and low relative humidities are known to be extremely poor.

2.4.2 Weighting Functions Computed from Model Atmospheres

Computations based on concurrent radiosonde data demonstrated that the technique discussed in Section 2.3.1 can reproduce the observed 6.4-6.9μ T_{bb}. The technique was then used to investigate the dependence of T_{bb} on atmospheric moisture and temperature by the use of model atmospheres.

13

Figures 2-5a and b show the basic models of the vertical distributions of mixing ratio and temperature used. The Washington, D.C. frost point hygrometer measurements of Mastenbrook (1966) for the summer months were averaged to obtain the mixing ratio profile shown in Figure 2-5a. The temperature profile shown in Figure 2-5b was taken from the midlatitude model given in the Handbook of Geophysics and Space Environments (Valley, S.L., Ed., 1965).
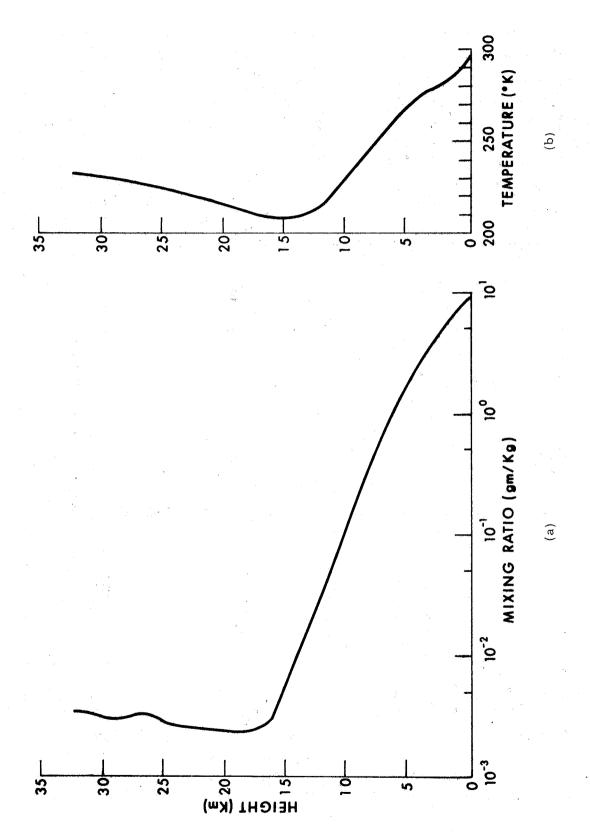
Figures 2-6a, b, and c show the general dependence of the water vapor weighting functions, for clear sky conditions, on temperature and mixing ratio distributions. In Figure 2-6a the mean midlatitude summer temperature distribution, $T_m(z)$, shown in Figure 2-5a was used. In Figures 2-6b (c), the temperature at each level was increased (decreased) by $3^\circ K$ above (below) $T_m(z)$. This $3^\circ K$ departure is the one sigma value of temperature deviation in the upper troposphere and lower stratosphere, as given by the Handbook of Geophysics and Space Environments. For each of the temperature profiles, weighting functions were computed for three mixing ratio (q) distributions. These were

$$q_1(z) = \text{mean midlatitude summer distribution (See Fig. 2-5a)}$$

$$q_2(z) = 0.5 q_1(z) \text{ for all } z$$

$$q_3(z) = 2 q_1(z) \text{ for all } z$$

The corresponding upper tropospheric relative humidities for these moisture distributions, in conjunction with the mean midlatitude summer temperature profile $T_m(z)$, would be:

Mixing Ratio	Relative Humidity
$q_1(z)$	$\sim 45\%$
$q_2(z)$	$\sim 20\%$
$q_3(z)$	$\sim 75\text{-}80\%$

Figures 2-6a, b, and c show an extreme dependence of the location of the $\overline{N}(z)$ peak on the mixing ratio distribution. Dependence on $T(z)$ is not apparent. For $q_3(z)$ (moist), the peak is located at ~ 9.5km (above 300 mb). For an atmosphere with a mean moisture, $q_1(z)$, this peak is located at ~ 9 km or 300 mb, i.e. about 0.5 km lower. It shifts very significantly further, to ~ 6.5 km (450 mb) for $q_2(z)$ (dry). In addition, the shape of the weighting function in the vicinity of the peak changes drastically from a moist atmosphere to a dry one. One way of describing

Figure 2-5   Mid-Latitude Model Distributions of Mixing Ratio (a) and Temperature (b).
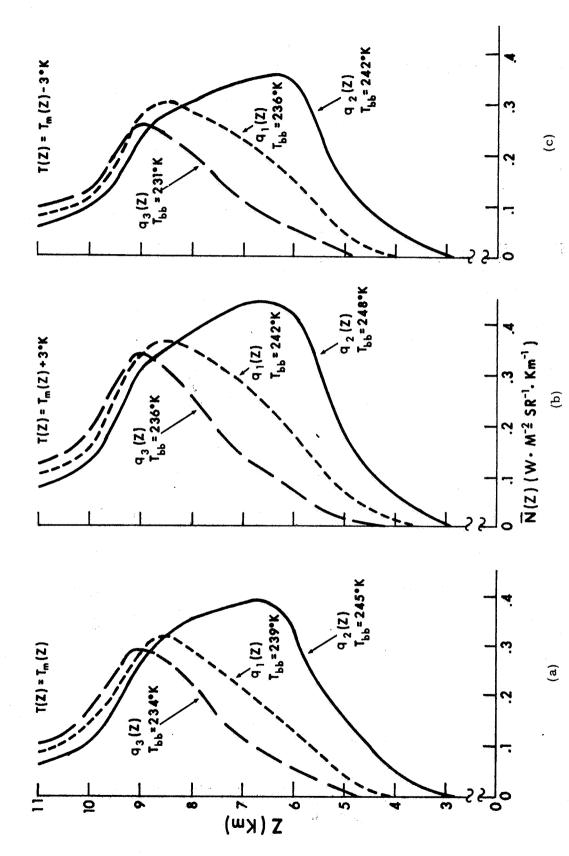
Figure 2-6   6.4-6.9μ Channel Weighting Functions Computed from Model Atmospheres.

this change in shape is in terms of the thickness of an arbitrarily chosen layer of maximum contribution centered at the peak. The following thicknesses, each containing about 60% of the total radiance, apply for $T(z) = T_m(z)$

$q_1(z)$ (normal) ~ 6.5-9.5 km, or about a 3 km layer

$q_2(z)$ (dry) ~ 5.5-9.5 km, or about a 4 km layer

$q_3(z)$ (moist) ~ 7-10 km, or about a 3 km layer

With decreasing moisture content, the layer not only thickens slightly, but also becomes less symmetrical about the peak. The rate of change of $\bar{N}(z)$ is far slower above the peak than below.

The dependence of the weighting function on temperature may be determined by comparing the weighting function for a given $q(z)$ at one temperature profile with the weighting function for the same $q(z)$ but at a different temperature profile. It is interesting to note that, at the accuracy and resolution used in the computations, the location of the weighting function peak does not seem to be very sensitive to changes in temperature profile. On the other hand, the dependence of $\bar{N}(z)$ on temperature, especially in the layer of maximum contribution, is apparent when comparisons of the absolute values of $\bar{N}(z)$ are made for the different models of $T(z)$.

Even for the driest and warmest model atmosphere used ($q_2(z)$, $T_m(z) + 3^\circ K$), contributions to the measured radiance are essentially zero below 3 km. It is, therefore, safe to say that water vapor channel T_{bb} are related to lower tropospheric moisture only if a correlation exists between lower and upper tropospheric moisture.

The computed T_{bb} values, as shown in Figure 2-6 range from $230^\circ K$ (moist and cold atmosphere) to $245^\circ K$ (warm and dry atmosphere). Examination of the digitized data for a number of orbits show values of T_{bb} in excess of $\sim 250^\circ K$. This would seem to indicate that none of the atmospheres used in Figure 2-6 were sufficiently dry and warm to depict such extreme conditions. Calculations show that, to obtain a T_{bb} of $255^\circ K$ by increasing $T(z)$ alone, the temperature profile must be $T(z) = T_m(z) + 10^\circ K$. A $10^\circ K$ temperature departure represents a 3 sigma departure from the mean. It is more likely, therefore, that the more frequent cause is an extremely low mixing ratio in the lower stratosphere and upper troposphere, coupled with at least some warming in these layers. This type of atmospheric structure is typically associated with upper level subsidence.

17

As stated in Section 2.4.1, radiosonde measurements of moisture are extremely poor for low values of relative humidity. Since it is expected that upper tropospheric relative humidities must be significantly lower than 20% to result in a $T_{bb} > 250^{\circ}K$, it becomes difficult, if not impossible, to confirm the moisture structure of the atmosphere, for these T_{bb} values, from concurrent radiosonde data. Inspection of the radiosonde data concurrent with $T_{bb} > 250^{\circ}K$ reveal one of the following: (a)"Motorboating" at high levels and/or (b) Mixing ratio and temperature distributions not drastically different from soundings through regions having measured T_{bb} values of $\sim 245^{\circ}K$.

The first of these conditions is certainly expected. "Motorboating" is an indication that the atmosphere was extremely dry at the time of the measurements. The second condition can often be explained in terms of the lag of the humidity sensor in responding to rapid decreases in moisture. More often than not, the radiosonde passed through a cloud layer at the bottom of the inversion typically associated with strong subsidence, thus becoming saturated. This can substantially increase the response time of the sensor.

Calculations were performed to determine the probable minimal conditions of the upper troposphere which would produce a water vapor channel T_{bb} of $250^{\circ}K$. This was done by an iterative scheme in which the mixing ratio was systematically decreased, and the temperature increased, to simulate a "subsidence inversion," until a computed T_{bb} of $250^{\circ}K$ was reached. Figure 2-7 shows an example of a "simulated" sounding. It should be pointed out that the upper tropospheric moisture distribution shown in Figure 2-7 is not unrealistic for extreme subsidence conditions. Sawyer (1958) and Murray (1956) have reported aircraft borne frost point hygrometer mixing ratios as low as 1 gm/kgm at 600 mb in the subsidence regions associated with baroclinic zones.

2.4.3 Effects of Clouds

Computations were made to estimate the effects of clouds on the $6.4-6.9\mu$ measurements. Clouds were assumed to radiate as blackbodies at a temperature corresponding to the cloud top temperature. For each of the values computed, it was also assumed that the field of view of the sensor was filled by a cloud of uniform cloud top altitude.

18
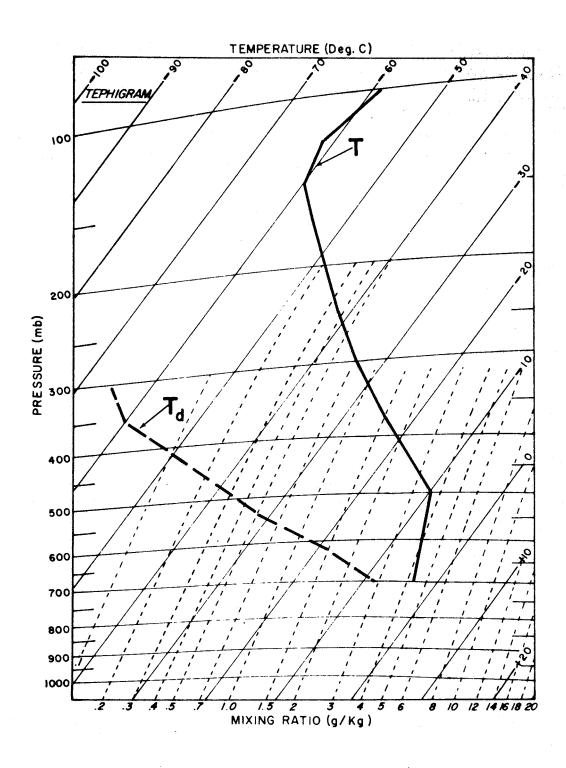
TEMPERATURE (Deg. C)

Figure 2-7   Simulated Sounding of Subsidence Condition

19

Figure 2-8a, b and c show the results of these calculations for the three temperature profiles used in the previous calculations of clear sky weighting functions. In Figure 2-8a, $T(z)$ was set equal to $T_m(z)$, while in Figures 2-8b and c, $T(z)$ was set at $T_m(z) + 3^\circ K$ and $T_m(z) - 3^\circ K$ respectively. These temperature profiles are shown in the respective figures by the solid curves. For each of the temperature profiles, computations of T_{bb} for a cloudy atmosphere were performed for the three mixing ratio profiles, $q_1(z)$, $q_2(z)$, and $q_3(z)$ discussed previously. The results are shown in the figures in which the computed T_{bb} values have been plotted against cloud top altitude indicated by the dashed lines.
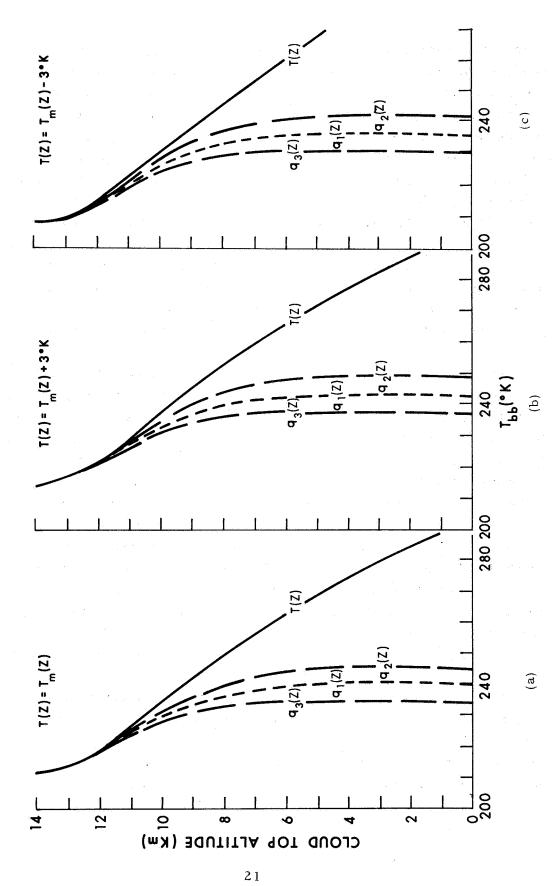
From these curves it may be seen that clouds with tops below 4 kms have little effect on the measured T_{bb}. This is an expected result since the weighting functions, shown in Figure 2-6, show that radiance contributions from below 4 kms are insignificant. Consequently, the raising of the lower boundary surface to 4 kms should not produce any significant changes.

A more interesting feature of the results shown in Figures 2-8a, b, and c is, with the exception of the dry atmosphere i.e. $q(z) = q_2(z)$, the presence of high and middle clouds results in $6.4-6.9\mu$ T_{bb} values $< 237K$. This is in virtual agreement with an empirical comparison study of measured T_{bb} values with concurrent cloud reports which showed that measured T_{bb}'s $< 235^\circ K$ are generally contaminated by multilayered clouds.

Since blackbody clouds were assumed, the results shown in Figures 2-8a, b, and c are not appropriate for thin cirrus. No attempt was made to investigate cirrus attenuation by analytical means. However, comparisons between measured T_{bb} values and concurrent cloud reports indicate that for $235^\circ K < T_{bb} < 240^\circ K$, cirrus contamination is highly probable. A case study of contamination by advected cirrus is discussed in detail in Section 2.4.4.

2.4.4 Evaluation of $6.4-6.9\mu$ H_2O Observations Along a Cirrus Cloud Trajectory

Cirrus clouds, visible from the ground and in Gemini X photography were apparently observed by the $6.4-6.9\mu$ channel of the Nimbus II MRIR. These cloud areas were not, however, obvious in the other channels of the MRIR, HRIR or AVCS. Resolution of this paradox is important to interpretation of MRIR data in general and bears on many possible applications of the $6.4-6.9\mu$ data in particular.

20

Figure 2-8 Cloud Contaminated 6.4-6.9μ Channel T_{bb}'s Computed from Model Atmospheres.

21
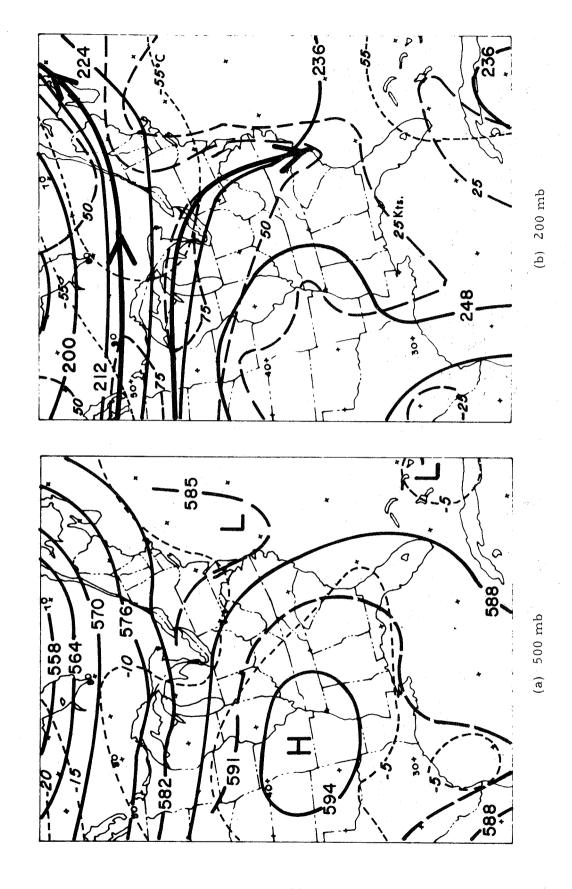
An initial evaluation was performed in a study of the $6.4-6.9\mu$ data and conventional observations along an isobaric trajectory. The trajectory extended from a dense cloud area in the Great Lakes region southward around the east side of a large anticyclone into the Florida panhandle region. The basic assumption was made that cirrus (ice crystals) or high level moisture were introduced into the upper troposphere (between 400 mb and 200 mb) by the active Great Lakes cloud system.

The fields of motion at 500 mb and 200 mb were changing very slowly during the analysis period, 17-19 July. Figures 2-9a and b show the 500 mb and 200 mb analyses for 1200 GMT, 18 July. The controlling wind field was the anticyclone centered over the Missouri—Oklahoma area. Isobaric trajectories for 500 mb and 200 mb (see Fig. 2-10) were constructed from streamline-isotach analyses at 12 hour intervals from 1200 GMT, 17 July to 1200 GMT, 19 July. Note that the two trajectories define an envelope. Air parcels starting at point X in Figure 2-10 at 1200 GMT on 17 July were found within the limits of the envelope area at the appropriate displacement point.

Nimbus II MRIR T_{bb} mappings for the $6.4-6.9\mu$ and $10-11\mu$ channels for 17-19 July are presented in Figure 2-11a, b and c. The trajectory envelope is superimposed on each analysis. Areas defining the most probable parcel location at the time of the satellite observation are indicated by the boxes along the trajectory. Note that, in general, the $6.4-6.9\mu$ values warm slowly with time. The $10-11\mu$ values, however, indicate marked changes.

The T_{bb} values for both channels within the areas along the trajectory are plotted in Figure 2-12. To minimize the possible effect of trajectory errors, the values plotted in Figure 2-12 are averages over the areas defined in Figure 2-10.

Calculated $6.4-6.9\mu$ T_{bb}'s using radiosonde data at or near the parcel locations are also shown. The top curve shows the calculated blackbody $6.4-6.9\mu$ temperature assuming no cloud. The lower curve shows similar values assuming a blackbody cloud at 9 km. The computed $6.4-6.9\mu$ values with no cloud assumed (i.e. based strictly on the observed vertical distribution of moisture and temperature) average some $5^{\circ}K$ warmer than the observed $6.4-6.9\mu$ values, while the values obtained assuming a blackbody cloud layer at 9 km, show reasonable agreement with the observed $6.4-6.9\mu$ values. The only $10-11\mu$ observation showing possible presence of cloud is at 1610 GMT, 18 July. The other observed T_{bb}'s from the $10-11\mu$ channel are near the expected surface shelter temperature. Ground observation also indicated the presence of a high level cirrus layer along the trajectory.

22

(b) 200 mb

(a) 500 mb

Figure 2-9   500 mb (a) and 200 mb (b) Analyses for 18 July 1966, 1200 GMT

23
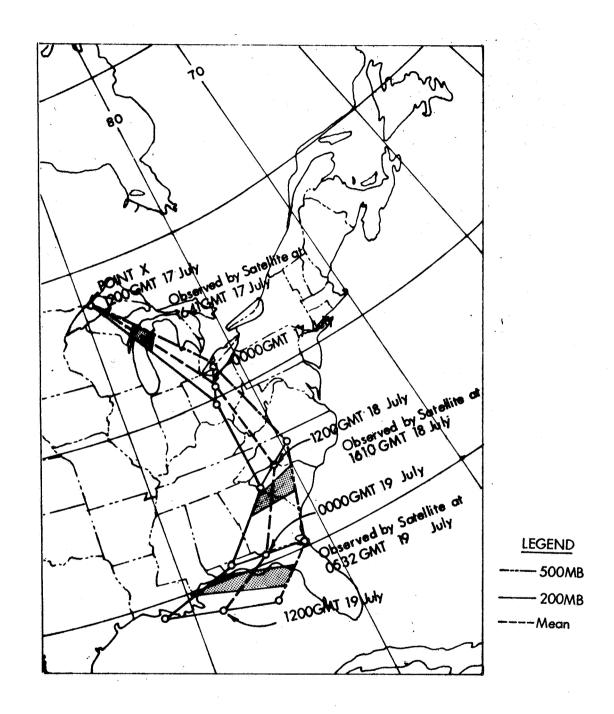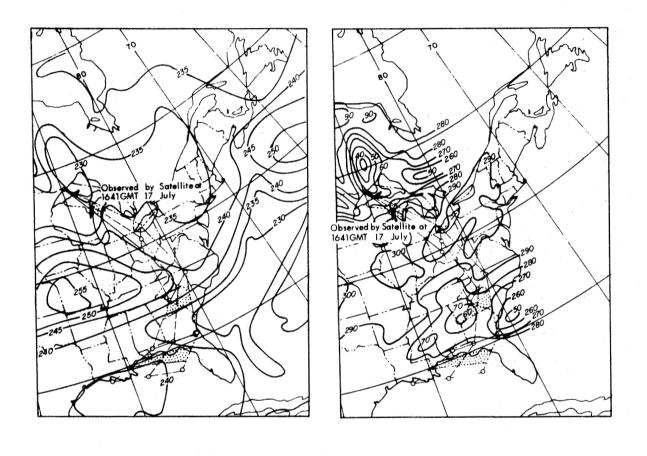
Figure 2-10 Isobaric Trajectories for 500 mb and 200 mb, 1200 GMT,
17 July to 1200 GMT, 19 July 1966.

24
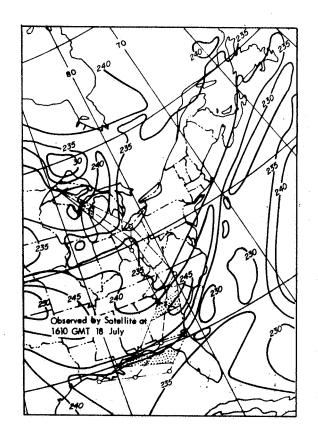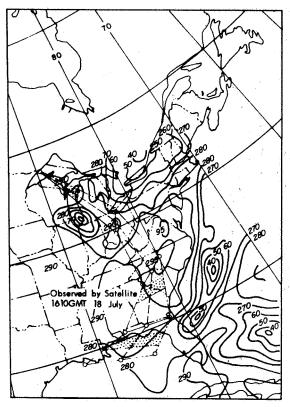
6.4-6.9μ   10-11μ

(a)   1641 GMT, 17 July 1966

Figure 2-11   Nimbus II MRIR Mappings for the 6.4-6.9μ
              and 10-11μ Channels for 17 through 19 July 1966.

25
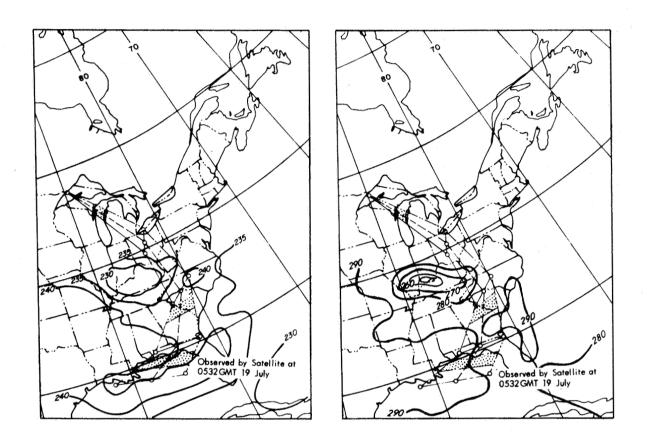
6.4-6.9μ

10-11μ

(b) 1610 GMT, 18 July 1966

Figure 2-11 Cont'd

6.4-6.9μ   10-11μ

(c) 0532 GMT, 19 July 1966

Figure 2-11 Cont'd

27
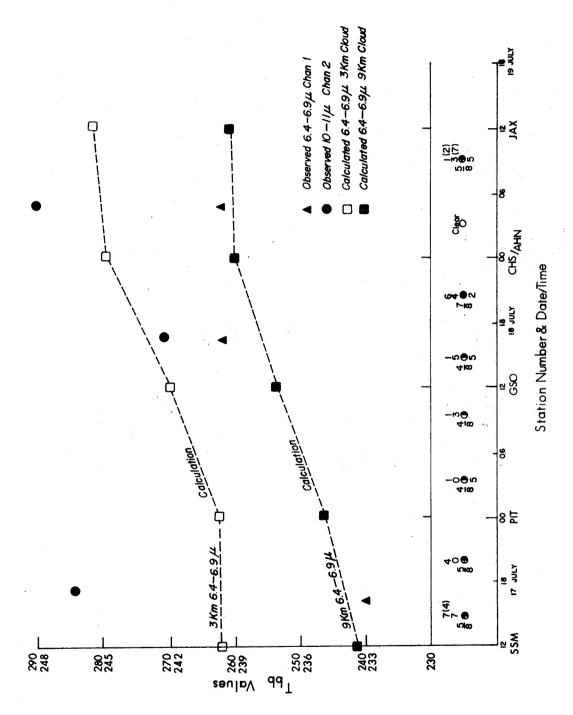
Figure 2-12 Averaged T_{bb} Values for the 6.4-6.9 and 10-11μ Channels over the Trajectory Defined in Figure 2-10.

A Nimbus APT photograph (Fig. 2-13) on 18 July at approximately 1610 GMT does not show this cirrus coverage. A Gemini X (Fig. 2-14) photograph on 19 July does appear to indicate the type of tenuous cirrus deck which is influencing the 6.4-6.9μ observations. It can be argued from this analysis that high level cirrus (or moisture) is detected by the 6.4-6.9μ channel while the 10-11μ channel effectively "sees" through such layers.

The radiosonde data from the stations along the trajectory were used to develop a space/time section which effectively indicated changes in the air column or parcel along its path. This procedure made it possible to investigate the possible reasons for the observed warming of the 6.4-6.9μ temperature.

Figure 2-15 shows the potential temperature and mixing ratios along the trajectory. If it is assumed that the potential temperature of a parcel between 500 and 200 mb is conserved, the analysis in Figure 2-15 indicates that descent was taking place between 200 and 500 mb. The mixing ratio values in Figure 2-15 do show a slight increase with time but the increase is not great enough to cause a significant change in the adiabatic assumption.

The analysis in Figure 2-15 provides a possible explanation for the warming 6.4-6.9μ temperatures. This isentropic analysis provides a possible explanation for the warming of the 6.4-6.9μ temperature along the trajectory. The descent, indicated in the analysis, would cause the cirrus particles to shift to lower levels where the radiating temperature would be correspondingly higher. In addition, the evaporation of cirrus particles (indicated by the increasing mixing ratio along the trajectory) would diminish the attenuating characteristics of the cloud. Either or both of these processes would result in a warming of the T_{bb} values along the trajectory.

2.4.4.1 Comparison of 6.4-6.9μ and 10-11μ Observations

The preceding section dealt with a parcel trajectory in the Lagrangian sense. This provided information about the changes within a volume or column as it moved from the source, near the Great Lakes, to the Florida panhandle.

A more complete picture of comparative 6.4-6.9μ and 10-11μ observations can be obtained by using a Eulerian system to investigate the regions near the parcel trajectory. The satellite data taken at 1610 GMT, 18 July provides information near the time when synoptic cloud observations were made.
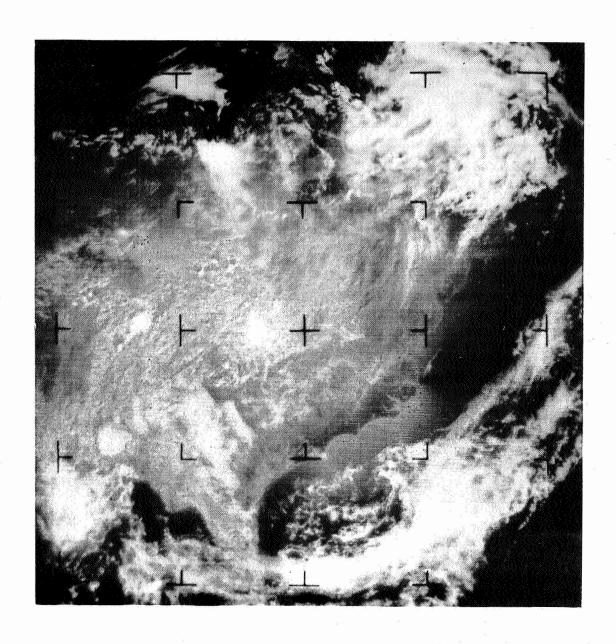
Figure 2-13 Nimbus II APT Photograph, 18 July 1966, ~ 1610 GMT.
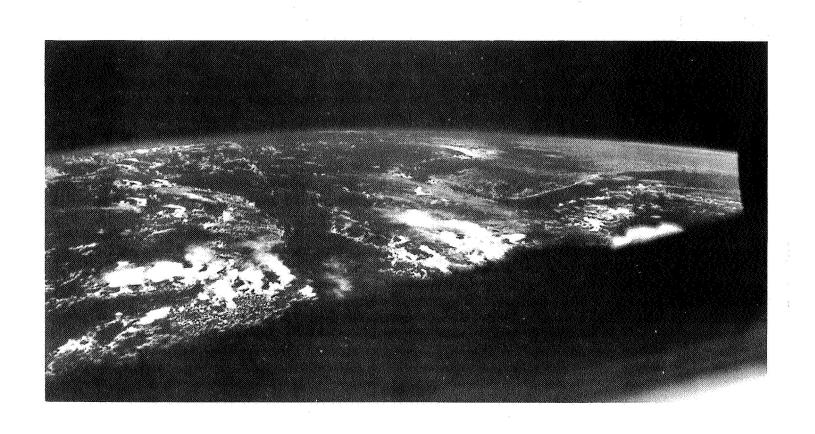
Figure 2-14   Gemini X Photograph, 19 July 1966.

31
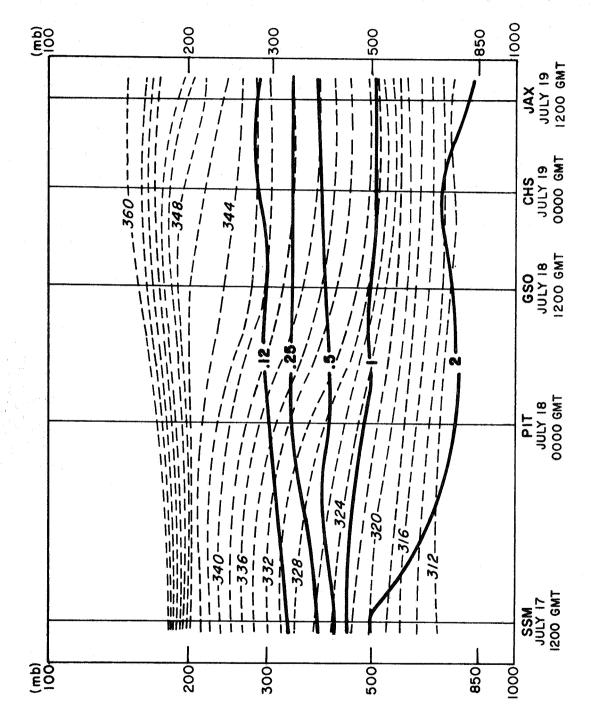
Figure 2-15 Potential Temperature and Mixing Ratios Along the Trajectory Defined in Figure 2-10.

A cross section (see Fig. 2-16) from station 630, the center of the storm at this time, to station 598 is shown in Figure 2-17. Cloud reports along this cross section are plotted at the bottom of the Figure. The 6.4-6.9μ and 10-11μ T_{bb} values, from orbit 856, are four hours after the surface cloud observation. Near the storm center the two channels sense the same temperature ($\sim$230K). South of this point along the cross section the 6.4-6.9μ temperatures remain cold with only a slight warming trend near the edge of the cirrus cloud. After the cloud edge is reached the 6.4-6.9μ temperatures warm to 245°K. On the other hand the 10-11μ temperatures increase some 15 or 20°K near the boundary between middle cloud and no middle cloud. The 10-11μ channel temperatures continue to increase along the cross section showing temperatures near the expected surface shelter temperature.

Figure 2-17 indicates that the 6.4-6.9μ channel was sensing cirrus cloud from the storm center to station 408 while the 10-11μ channel showed marked warming at the boundary between middle cloud and no middle cloud. The observations along this cross section support the contention that cirrus cloud not apparent in the 10-11μ channel data is detected by the 6.4-6.9μ channel.

2.4.4.2   Summary Discussion

Analysis of an isobaric trajectory (defined by trajectories at 500 mb and 200 mb) from a dense cloud area southward over the east side of a large anticyclone and a cross section from the dense cloud to a clear region has indicated the following items significant in interpretations and applications of 6.4-6.9μ H_2O observations.

a.   The 6.4-6.9μ channel is responsive to relatively thin cirrus (ice crystal) cloud layers. These layers are apparently visible from the ground and in Gemini photography but are not obvious in Nimbus photography. This analysis suggests that early summer T_{bb} values colder than 240°K may be influenced by cirrus (calculations shown in Section 2.4.2 indicate that a colder than standard moist atmosphere is required to obtain T_{bb} values less than 240°K without consideration of cirrus cloudiness). Furthermore with 6.4-6.9μ T_{bb} values colder than 230°K we can state, on the basis of this analysis, that cirrus clouds are influencing the observation. Other studies presented in this report show that 6.4-6.9μ values colder than 235°K are associated with multilayered cloud areas including cirrus.

33
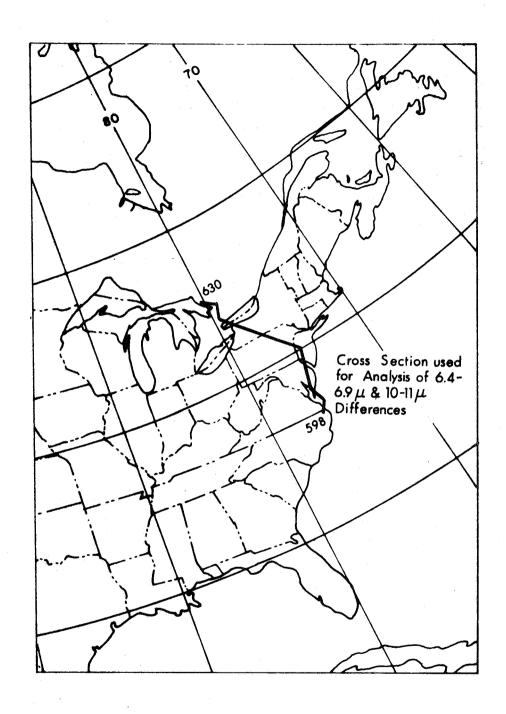
Figure 2-16 Cross Section 18 July 1966, 1610 GMT, Used for Analysis of 6.4-6.9μ and 10-11μ Differences in Figure 2-17.
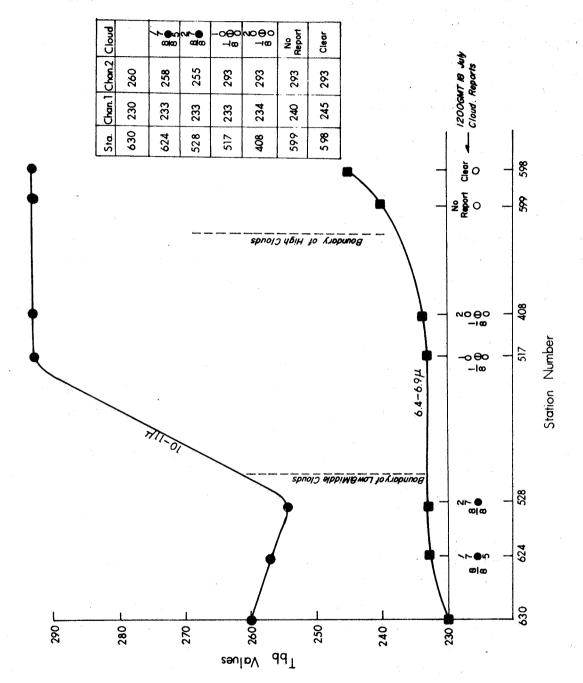
Figure 2-17 Analysis of 6.4-6.9µ and 10-11µ Differences 18 July 1966, 1610 GMT.

35

b. Slowly descending cirrus ice crystal clouds having an assumed particle size distribution in the 10-30μ range can be advected over great horizontal distances before complete sublimation or fall-out occurs. This supports the contention of Ludlam and Miller (1959) who stated, "the edge of an evaporating ice cloud may be anticipated to lie at least several hundreds of kilometers beyond the region where the cloud air begins its descent." Ground observations, Gemini photography and 6.4-6.9μ observations appear to verify that cirrus was present near 8-10 km over all but the extreme southern end of the parcel trajectory.

2.5 Carbon Dioxide Weighting Functions

The 14-16μ measurements are easier to interpret, at least from atmospheric structure viewpoint, than the 6.4-6.9μ measurements. This is due to the fact that, in this spectral interval, the weighting functions and measured T_{bb}'s depend primarily on the vertical distribution of temperature. Furthermore, the atmospheric layer of maximum contribution is confined to the lower stratosphere. The measured variations in the 14-16μ T_{bb} should, therefore, reflect variations in lower stratospheric temperatures.

Figure 2-18 shows the typical latitudinal variations in the 14-16μ weighting functions. These were computed at 15°N, 30°N and 60°N, based on model atmospheres at these latitudes given in the Handbook of Geophysics and Space Environments. It is interesting to note that the peaks of the weighting functions sloping upwards from the pole to the Equator, corresponding to the tropopause height.

Figure 2-18 shows the computed latitudinal variation of 14-16μ T_{bb}. The poleward increase in T_{bb} reflects the latitudinal variations in lower stratospheric temperature. These computed latitudinal variations are in general agreement with the data obtained by TIROS VII. The basic difference (apart from the improved sensor noise characteristics) lies in the fact that the spectral response of the MRIR 14-16μ channel extends further out into the wings of the 15μ CO_2 absorption band, where the atmosphere is slightly more transparent. As a consequence, the peaks of the weighting function are shifted further down into the atmosphere where cloud contamination becomes possible. Examination of the 14-16μ digital T_{bb} values for a number of orbits showed that, indeed cloud contamination was significant. Clouds with tops significantly below tropopause levels caused noticeable changes in the "normal" south-north gradient. When clouds extend high enough to influence the 14-16μ measurement, their dominating effects tend to mask any changes in lower stratospheric temperatures

36
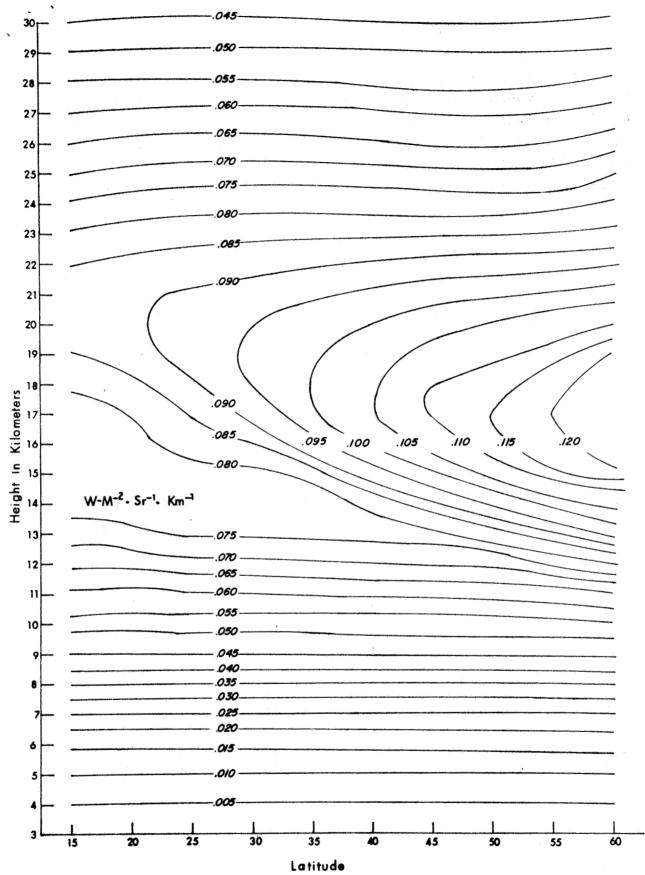
Figure 2-18 14-16µ Channel Weighting Function Computed from Model Atmospheres.

resulting from other dynamical effects (e.g. the lowering of the tropopause in the vicinity of storms). For example, it would require a 10°K warming in a deep layer of $\sim$5-8 km, and in the vicinity of the weighting function peak, to result in a measured T_{bb} increase of $\sim 4^{\circ}$K. This may be seen by comparing the computed T_{bb} values at 60°N and 45°N. The difference between these two values ($\sim 4^{\circ}$K) is due mainly to the difference in the lower stratospheric temperatures, which is of the order of $\sim 18^{\circ}$K in the layer from $\sim$5-8 km. These observations are in agreement with the results of Merritt and Chang (1966) for TIROS VII.

The basic result of this investigation of the 14-16μ channel is that the information contained in the data, in general, consists of the latitudinal variations in lower stratospheric temperatures, with cloud contaminated regions superimposed. However, in a number of instances, it was possible to relate some of the variations in the measured values to dynamical changes in the troposphere. These will be discussed in subsequent sections.

2.6 Summary of Computation Results

The results of the computation studies may be summarized as follows:

2.6.1 6.4-6.9μ Channel

1. Low level clouds and moisture apparently have little or no effect on the measurements.

2. In the absence of high and middle clouds, there seems to be an inverse correlation between the upper tropospheric precipitable water content and the measured temperature. For values of $T_{bb} > 245^{\circ}$K, the upper troposphere is most likely very dry and warm.

3. It is often difficult to distinguish cloud-free from cloud-contaminated data except by concurrent reference to window channel data, or in daytime to visible channel data or TV pictures. This problem is most acute in the presence of thin cirrus. Under certain conditions, the presence of such clouds are not revealed in the concurrent visible or 10-11μ channel data. It seems likely that cirrus contamination is the cause of much of the observed T_{bb} values in the range 235-240K.

4. While it is impossible to establish a specific T_{bb} value which delineates cloud free from cloud contaminated data, it is very probable that T_{bb}'s $> 240^{\circ}$K are free from significant cloud contamination and $T_{bb} < 235^{\circ}$K are contaminated by multi-layered clouds. At temperatures less than 235°K, the information content of the 6.4-6.9μ channel is redundant when concurrent 10-11μ channel data are also available. However, when the measured values are greater than 235°K they provide information regarding atmospheric structure that is generally not contained in the other channels.

2.6.2   14-16μ Channel

The wide spectral response of this channel makes contamination by high and even middle clouds a serious problem. In spite of this, it may still be possible to observe local differences in lower stratospheric temperatures associated with tropospheric dynamic effects, provided the lower stratospheric warming takes place through a substantial layer.

3. METEOROLOGICAL APPLICATIONS

This section deals with the relationships between the MRIR observations and such meteorological phenomena as baroclinic storms and jet streams. In general, the resolution of the MRIR sensors dictates the scales of motion which can be investigated. Features having a horizontal scale of less than 60 km cannot be resolved by the MRIR. For this reason, the following discussion will be limited to synoptic scale features.

3.1 The Structure of Atmospheric Systems

Most atmospheric motions are produced by, and modify, the thermal structure of the atmosphere. One way to specify the thermal structure as it applies to the generation of atmospheric motions is the baroclinicity, which is a measure of the isobaric-isosteric solenoids. Most important weather producing systems are associated with concentrations of these solenoids in regions of strong baroclinicity, or baroclinic zones.

Vertical motions related to these baroclinic regions often produce marked changes in the distribution of tropospheric moisture. The 6.4-6.9μ channel measures the radiant energy emitted due to an integrated effect of the temperature and moisture distribution in the middle and upper troposphere, as described in Section 2. It is thus appropriate to consider application of MRIR data, particularly the 6.4-6.9μ data, to analyses and interpretations of baroclinic systems in both the tropics and the extra-tropics.

3.1.1 Extratropical Jet Streams and Baroclinic Storms

3.1.1.1 Extratropical Jet Streams

Jet streams, strong narrow wind currents concentrated along a quasi-horizontal axis in the upper troposphere, and their related baroclinic zones have received much attention over the last two decades (Riehl, 1962, 1948; Reiter, 1963;[†] Bradbury and Palmen, 1953; Endlich and McLean, 1957; Riehl and Teweles, 1953; and others).

[†]   Reiter, 1963, provides a particularly comprehensive background reference.

The average strength and position of the jet stream reacts to seasonal fluctuations in the heat budget of the hemisphere, showing that the tropospheric jet stream is a phenomenon dependent on the thermal differences between pole and equator. The close connection between jet streams and the baroclinic zones (frontal surfaces) formed at the boundaries of the contrasting polar and tropical air masses is in accordance with the thermal wind relationship, which shows that a strong wind band must be balanced by a strong horizontal thermal gradient.

Variations in wind speed along the jet axis are produced by perturbation motions resulting from super-geostrophic and sub-geostrophic flow. These speed variations, combined with changing streamline curvature produce distinct patterns of vertical motion. These in turn lead to varying high level moisture concentrations near and along the jet axis.

Radiosonde measurements of moisture in the upper troposphere, especially near jet streams, are limited both in quantity and quality. These limitations have made it necessary to rely on measurements taken by aircraft, or deductions based on vertical motion calculations at high levels. The moisture distribution can be partially inferred from the vertical motion patterns, i.e., subsidence is associated with drying, and lifting generally with increased moisture, in the upper troposphere. Studies by Palmen (1958), and others, have established the synoptic scale patterns of vertical motion near cyclones. Reed and Danielsen (1959), and Danielsen (1964), have demonstrated that strong vertical motions are not confined to the troposphere. Their studies showed maximum sinking occurs near and below the jet stream, with the vertical transport coming from the stratosphere through the level of maximum wind. In this manner, dry stratospheric air is transported within the baroclinic zone into the middle troposphere (see Fig. 3-1). Calculations by Endlich (1953), using upper level charts, show very large values of vertical motion (up to 16 cm/sec for a three hour mean). The order of magnitude of these values was later confirmed by Brundidge (1958), and Reiter (1963). In all cases the centers of maximum vertical velocity were at, or near, the jet axis.

The investigations referred to above were primarily concerned with vertical motions near the jet stream, and the moisture distributions can only be inferred from the findings. Studies by Vuorela (1957), attempted to determine the vertical velocities from the observed differences between the dew point and the free air temperature. Vuorela's work provides a direct estimate of the moisture patterns in and near the

42
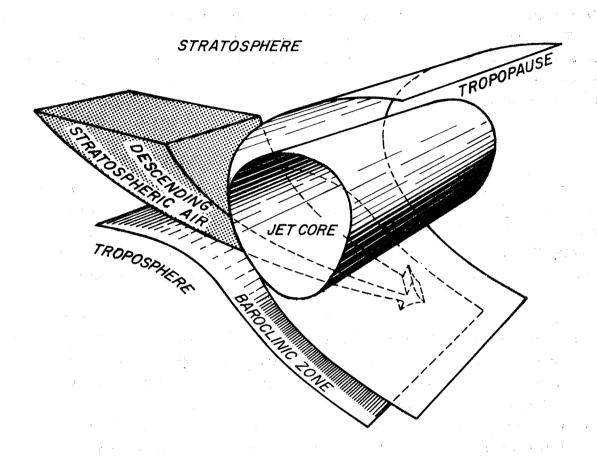
Figure 3-1 Schematic Representation of Stratospheric Air Descending
Under the Jet Core, Along the Baroclinic Zone.

jet stream. He observed extreme dryness within the frontal (baroclinic) zone, probably due to the intrusion of stratospheric air. British research flight measurements, analyzed by Sawyer (1958, 1955), and Murray (1956), supported Vuorela's findings. It is apparent from the above referenced studies that dry air of extremely low frost points is present underneath the jet core, along the frontal zone.

The observed sinking and drying associated with jet streams, combined with the capability of the MRIR water vapor channel to detect dry regions near the level of the jet, has formed the basis of a working hypothesis that jet streams can be located by a band of warm $6.4-6.9\mu$ temperature.

3.1.1.2 Extratropical Baroclinic Storms

Any discussion of extratropical cyclones must assume the existence of a jet stream, for the dynamics of the two features are closely related by the thermal gradient which support cyclogenesis and jet stream formation. As was pointed out by Teweles (1954): "Not every jet stream is accompanied by a cyclone; but, each cyclone is attached to a jet stream which is continuously changed by the life cycle of the cyclone."

Early attempts to describe atmospheric motions in terms of a circulation model resulted in the Norwegian Polar front theory (Bjerknes and Solberg, 1921), which emphasized the boundary surfaces between air masses of different characteristics. The model essentially consists of two bodies of air with different densities (temperature) meeting in a strong baroclinic zone or front. Perturbations in the wind field acting normal to the frontal surfaces cause a deformation in the front, which then amplifies through the stage of a wave disturbance into a closed vortex. This model serves to describe what is observed at the surface, but it does not explain why the convergence of flow associated with the wave formation on the baroclinic zone is associated with pressure fall rather than pressure rise. Neither can it explain the often observed occurrence of precipitation in the warm sector. Later work, culminating in the vorticity-advection theory, provided an explanation for these shortcomings.

Vorticity advection is defined by,

$$A_Q = - V \frac{\partial Q}{\partial S} \qquad (3)$$

where

Q = absolute vorticity = $VK_s - \frac{\partial V}{\partial n}$ + f (in natural coordinates)

V = wind speed along a streamline

s = distance along a streamline

n = distance normal to a streamline

K_s = curvature of the streamline (+ for cyclonic)

f = Coriolis parameter

The simplified relationship between vorticity and divergence (D) is $1/Q \; dQ/dt = - D$. Vorticity advection associated with jet streams provides the strong divergence and outflow aloft necessary to produce pressure falls in the region of low level convergence. The upper level divergence and vorticity patterns also offer an explanation for precipitation in the warm sector. This leads to the following basic model (see Fig. 3-2) which was used for comparison in the interpretation of the MRIR observations of extratropical baroclinic storms. The model shows the general positioning of jet stream related divergence and convergence as they relate to cyclone development.

Early research efforts involving the use of satellite data for analyzing cyclonic vorticities concentrated on the horizontal cloud field. This work has led to descriptions of the appearance of baroclinic storms at various stages of their development, Widger(1964), Sherr and Rogers (1965), Rogers and Sherr (1966). The earlier of these studies used satellite TV (visible spectrum) data, and conclusions were drawn from the shape, brightness and extent of the visible cloud field. Data from sensors operating in the 3.7μ and/or 10μ atmospheric windows were later used to determine cloud heights associated with cyclones and cyclone families.

Different aspects of the cloud field are detected in each of the MRIR channels. In the case of the $14-16\mu$ (CO_2) channel, only very high cumulonimbus cells are seen, while the $6.4-6.9\mu$ (water vapor) channel is capable of observing all but low clouds. The remaining channels (visible, $10-11\mu$ and $5-30\mu$) give a fairly complete picture of the entire cloud field.
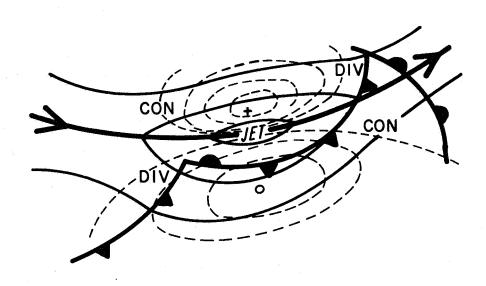
Figure 3-2   Schematic Representation of the Interaction Between the
Jet Stream and a Baroclinic System (Reiter 1961).

Because the general cloud field can be seen in the MRIR imagery, it would be duplication of effort to go through the process of reconstructing the horizontal cloud field patterns associated with a baroclinic storm. Rather, the case studies presented in later sections of this report will concentrate on those features that are unique to the MRIR presentation, especially the $6.4-6.9\mu$ and $14-16\mu$ channels.

3.2 Case Studies
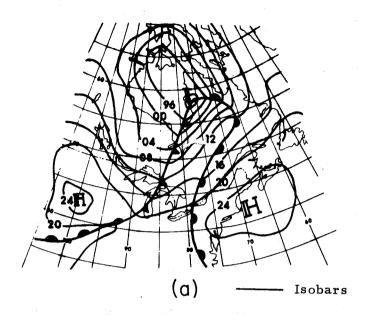
This section presents several cases depicting the MRIR observed radiation patterns associated with extratropical jet streams and baroclinic storms. Variations with different flow conditions, and time, are considered.

3.2.1 Jet Stream Analysis, 26 June 1966

On 26 June 1966, a rather typical synoptic pattern existed over the United States and Canada. Figures 3-3 and 3-4 present the surface, 500 mb and 200 mb analyses for 1200 GMT, 26 June and 0000 GMT, 27 June 1966. A major jet stream and frontal system extended in a broad arc from the central Rockies into the Hudson Bay region.

These analyses are based on data approximately four hours before and eight hours after the closest Nimbus observation (approximately 1600 GMT). The MRIR observations shown in Figure 3-5 from orbit 546 of Nimbus II, correspond most nearly in time to the analyses for 1200 GMT, 26 June. The jet stream position superimposed on the $6.4-6.9\mu$ channel analysis in Figure 3-5 was linearly interpolated from its positions in Figures 3-3 and 3-4 to account for the time difference. A similar procedure was used to locate the frontal positions, also shown in this figure. These frontal positions were checked against a nephanalysis of ground observed clouds made within an hour (at 1600 GMT) of satellite observation time. This check also indicated that the interpolated position of the jet stream axis at 1600 GMT is probably correct.

It is interesting to note, in Figure 3-5, that the warmest $6.4-6.9\mu$ T_{bb} ($> 250^\circ K$), and therefore, driest region corresponded to the location of the jet stream maximum. The 1600 GMT nephanalysis also shows a clear region which corresponded in shape and location to the warm band observed by the $6.4-6.9\mu$ channel.

(a) ——— Isobars

(b)

——— Contour heights (m)
– – – – – Isotherms (°C)

(c)

——— Contour heights (m)
– – – – – Isotachs (kts)
——► Jet axis
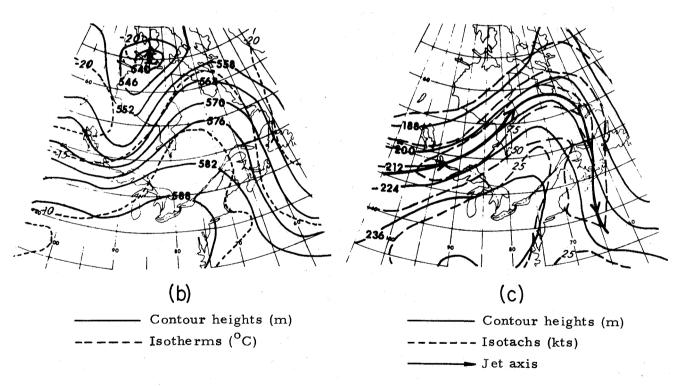
Figure 3-3   Surface (a), 500 mb (b) and 200 mb (c) Analyses for
1200 GMT, 26 June 1966.

48

(a)

(b)   (c)
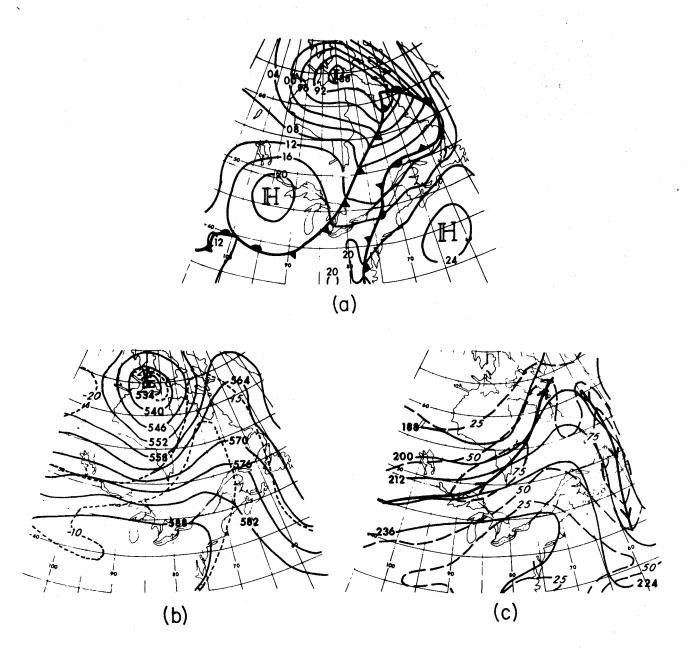
Figure 3-4   Surface (a), 500 mb (b) and 200 mb (c) Analyses for
0000 GMT, 27 June 1966.
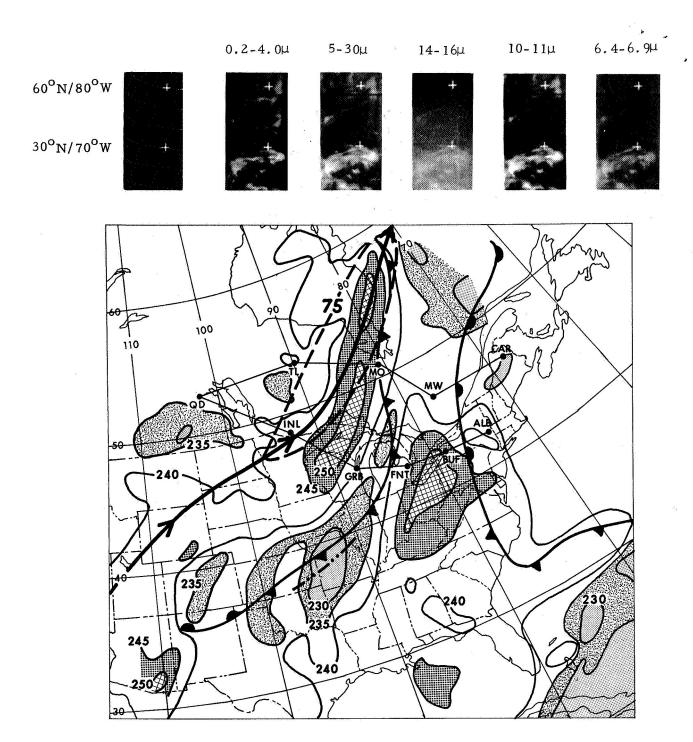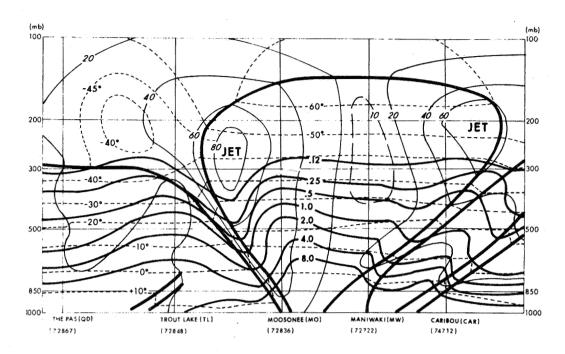
Figure 3-5   Analysis of $6.4-6.9\mu$ Channel T_{bb} at 1600 GMT, 26 June 1966
(The superimposed surface fronts and jet streams are adjusted
to the time of the satellite pass. Thin lines between stations
show the axis of cross section referred to in the text.)

No radiosonde ascents through this warmest T_{bb} region were available for this case. Based on the observed 250°K T_{bb}, however, it was inferred that the atmosphere must have been very dry and quite warm near the level from which the 6.4-6.9μ radiometer received its maximum contribution. An attempt was made to deduce the vertical distributions of temperature and moisture in the vicinity of the warm band, using the procedure described in the following paragraphs.
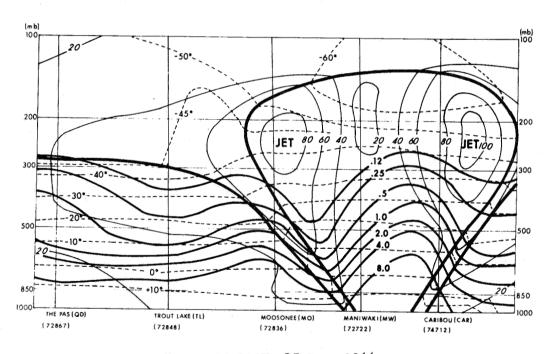
Cross sections of wind, temperature and mixing ratio were prepared from The Pas (QD), Canada, to Caribou (CAR), Maine, and from The Pas to Buffalo (BUF), New York. Two cross sections, valid at 1200 GMT, 26 June and 0000 GMT, 27 June, were analyzed along the northern cross section (see Figs. 3-6a and 3-6b). The southern cross section was analyzed for 1200 GMT, 26 June only. The stations along these cross sections were close enough to adequately depict the positions of the baroclinic zone and jet core; but, the large deviations in the moisture field, needed to produce a T_{bb} of 250°K, were not detected. This was not unexpected, since the warm band of T_{bb} was much narrower than the station spacings.

Procedures similar to those discussed previously were used to relate the position of the jet and the same dark band as it appeared in MRIR observations made 24 hours later, at 1600 GMT, 27 June. Curves representing the T_{bb} values along the northern cross section, at the times of the two satellite passes, are shown in Figure 3-7 by the solid lines. The peaks on these curves represent the positions of the warm band as observed by the satellite at 1600 GMT, 26 June and 1600 GMT, 27 June. By linear interpolation, the position of these peaks (warm bands) at 1200 GMT, 26 June and 0000 GMT, 27 June (the times of the standard radiosonde measurements used to prepare the cross sections in Figure 3-6) were interpolated and are shown by the dashed lines in Figure 3-7.

The interpolated positions of the dark bands correspond to the locations of the baroclinic zones shown in Figures 3-6a and 3-6b. Based on the interpolated positions of the peaks (warm band) and the established relationships between upper tropospheric moisture and 6.4-6.9μ T_{bb} (see Moller and Raschke, 1964, and Nordberg, et al, 1966), the mixing ratios in the vicinity of the baroclinic zone were re-analyzed. These analyses were then checked by computing the T_{bb} which would be measured by the 6.4-6.9μ channel of Nimbus II, using a computation procedure similar to that described in Section 2.2. This procedure was reiterated until the analyzed values agreed with the satellite observed T_{bb}. (The computed T_{bb} values from the radiosonde ascents

51
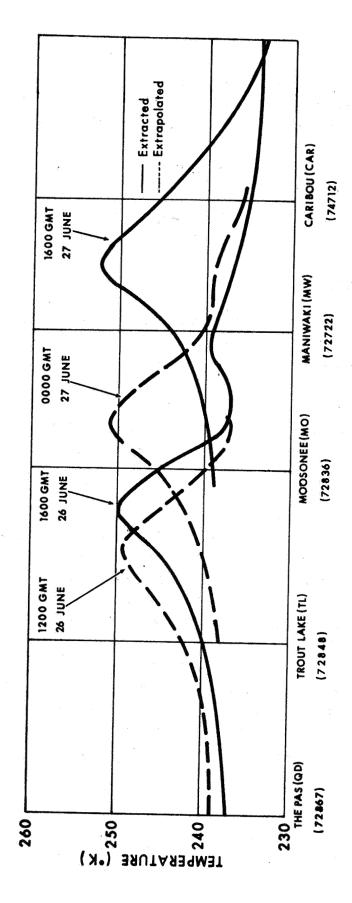
(a)   1200 GMT, 26 June 1966

(b)   0000 GMT, 27 June 1966

Figure 3-6   Cross Sections Normal to Warm Band at 1200 GMT,
26 June and 0000 GMT, 27 June 1966. (see Fig. 3-5).

Figure 3-7 6.4-6.9µ Channel T_{bb} Extracted from Digital Analysis and Extrapolated to Correspond to the Times of Cross Sections Shown in Figure 3-6.

corresponded to within 1 or 2°K of the interpolated satellite measured values shown in Figure 3-7, indicating a very good correlation between calculated and observed temperatures.) A similar method was used to produce the cross section shown in Figure 3-8.
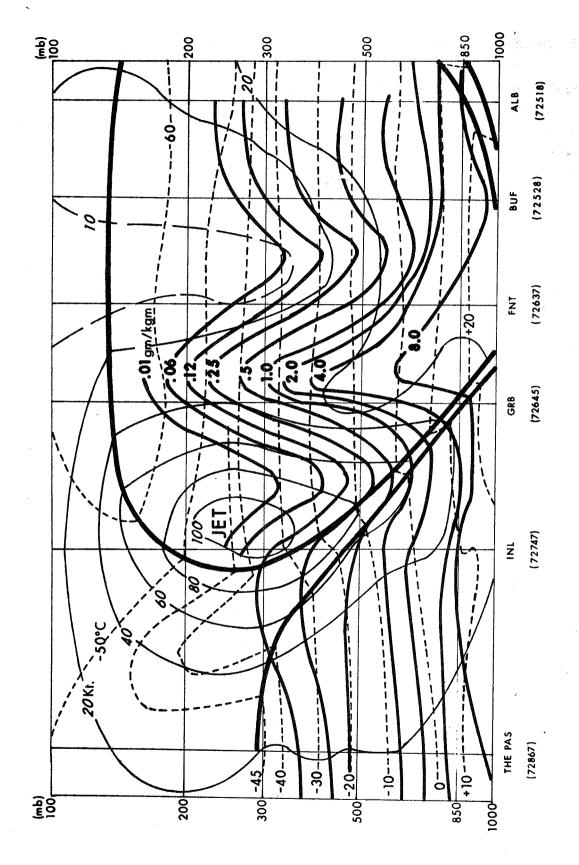
The deduced moisture and temperature fields within the baroclinic zones are in general agreement with classical models. Some differences do exist between Figure 3-6 (jet core center) and Figure 3-7 (entrance region). These differences are discussed in the next section.

3.2.1.1 Discussion

The analyses show a band of warm ($> 245^{\circ}$K) 6.4-6.9μ effective blackbody temperatures parallel to, and very near, the core of maximum winds along the jet stream axis. This region of warm T_{bb} was apparently associated with a strong baroclinic zone. Computations show that low mixing ratios in the upper and middle troposphere, must have existed. This is in agreement with the investigations referenced in Section 3.1.1.1 indicating that the dynamic mechanism responsible for this warm band of T_{bb} was the strong downward intrusion of stratospheric air into, and beneath, the jet stream.

The slight southeastward displacement of the warm band near the entrance region of the isotach maximum (see Figs. 3-5 and 3-8), between INL and GRB, implys a close relationship between the specific location of the region of warm T_{bb}'s and the shape of the baroclinic zone. Along the northern cross section (QD to CAR) the surface "frontal position" was near the jet axis, indicating a rather steep baroclinic zone; here, the warm band was directly under the jet axis. Along the southern cross section, the surface frontal position was farther from the jet axis, indicating a baroclinic zone with a rather shallow slope; here, the warm band was displaced to a position between the jet axis and the surface front.

There seems to be little question that in this case, the observations from the Nimbus II 6.4-6.9μ data revealed the location, and perhaps the intensity of jet stream related vertical motions. The rather common occurrence of these warm bands in the 6.4-6.9μ data suggests that jet stream positions, on a global basis are being shown.

Figure 3-8   Cross Section Normal to Warm Bands Near the Entrance Region of the Jet Core at
1200 GMT, 26 June 1966. (see Fig. 3-5.)

3.2.2   Jet Stream Case, 10 June 1966

Strong downward vertical motions to the east of an anticyclonically curved jet stream can also produce the upper tropospheric warming and drying necessary for the appearance of a band or area of warm T_{bb} in the 6.4-6.9μ data. Many such cases are observed in the Nimbus II MRIR data sample. In general, the warm bands to the east of these ridge positions appear to be associated with weaker upper tropospheric subsidence than is found near and to the east of troughs. An example of the warm band found to the east of a ridge is shown in Figure 3-9a. This warm area, centered at 48N, 55W, was located just to the east of the ridge accompanied by a very strong anticyclonically curving jet stream (strongest reported winds were 175 knots). As in the cases discussed previously, the major axis of the warm band was parallel to the jet stream, but was occurring on the eastern side of a ridge, rather than to the east of a trough. Generally, the most reliable way of differentiating the two types of bands is to note the relative orientation of their major axes. Near and to the east of the trough line the axis of the warm band will generally be northeast-southwest (in the Northern Hemisphere). East of a ridge, the direction will be northwest-southeast. This naturally follows the orientation of trough and ridge planetary flow and assumes an uncomplicated sinusoidal flow pattern.

Bands appearing east of trough lines cross from the equatorward side, near the trough line, to the poleward side at the downstream inflection point of the jet axis (see Fig. 3-5). On the other hand, those to the east of a ridge line have a tendency to be on the poleward side of the axis for their entire length.

The very warm band south of the Great Lakes in Figure 3-9a was situated near a trough line. Here the situation was similar to the November 1962 "shadow band" case analyzed by Oliver et al (1964), and Reiter and Whitney (1965). The November 1962 case showed a very long narrow dark band in a TIROS VI picture. It was determined that the dark strip was probably produced by the shadow of the high clouds, to the equatorward side of the jet axis, falling on lower clouds to the poleward side. The jet stream configuration during the November "shadow band" case included merging or crossing, (see Reiter and Whitney 1965) polar front and subtropical jets. Figure 3-9a shows the same merging of two jet stream systems in an MRIR-observed case. The very warm 6.4-6.9μ effective blackbody temperatures found near the confluence area of the two jet streams indicates very strong upper tropospheric subsidence.

It is interesting to note that the Nimbus II AVCS picture taken at the same time as the MRIR data in Figure 3-9a shows a dark band exactly where the shadow band should occur. Figure 3-9b shows this AVCS picture with the jet stream axis and the 6.4-6.9μ pattern superimposed. In the absence of other information or sun angle calculations, it would be difficult to be sure that this AVCS band was associated with the jet stream, but the juxtaposition of the MRIR pattern and the jet stream provide evidence which certainly suggests the presence of a shadow band.

This case again demonstrates an advantage of the water vapor channel in defining upper level wind systems. In order for the "shadow" to be detected in visible spectrum data (such as a TV picture), the sun angle and cloud fields had to be uniquely interrelated. Only when this happened, could a wind band area be identified. The upper tropospheric vertical motions inferred from the 6.4-6.9μ channel "warm bands" are capable of depicting a maximum wind band regardless of the lighting conditions or the cloud field.

3.2.3 Warm 6.4-6.9μ Bands Along Shear Lines

An interesting evolution of the warm bands takes place as the planetary flow wave amplitude increases and the wavelength decreases. Hsieh (1950) investigated the dynamics responsible for the formation of cutoff lows and shear lines ultimately associated with these wavelength and amplitude changes.

A schematic representation of upper shear-line development is shown by the 500 mb isotherms and contours in Figure 3-10 (from Hsieh 1950). It is apparent that the evolution from sinusoidal flow to the final configuration shown by Hsieh's schematic should cause the warm band east of the ridge to be brought into juxtaposition with the band east of the trough. When this occurs, a single warm band along the shear line should be produced. A second schematic from Hsieh's work (see Fig. 3-11) shows the distribution of vertical motions associated with the shear line. This figure, representing a cross section normal to the shear line, shows the most intense downward vertical motion along the shear line, occurs at about 400 mb. This is near the level of maximum response in the water vapor channel, and clearly should appear as a very warm region in the 6.4-6.9μ channel . A case showing the warm band along a shear line is presented in Figure 3-12. The jet stream axis and the stream line along the trough are superimposed on the digitized data from the 6.4-6.9μ
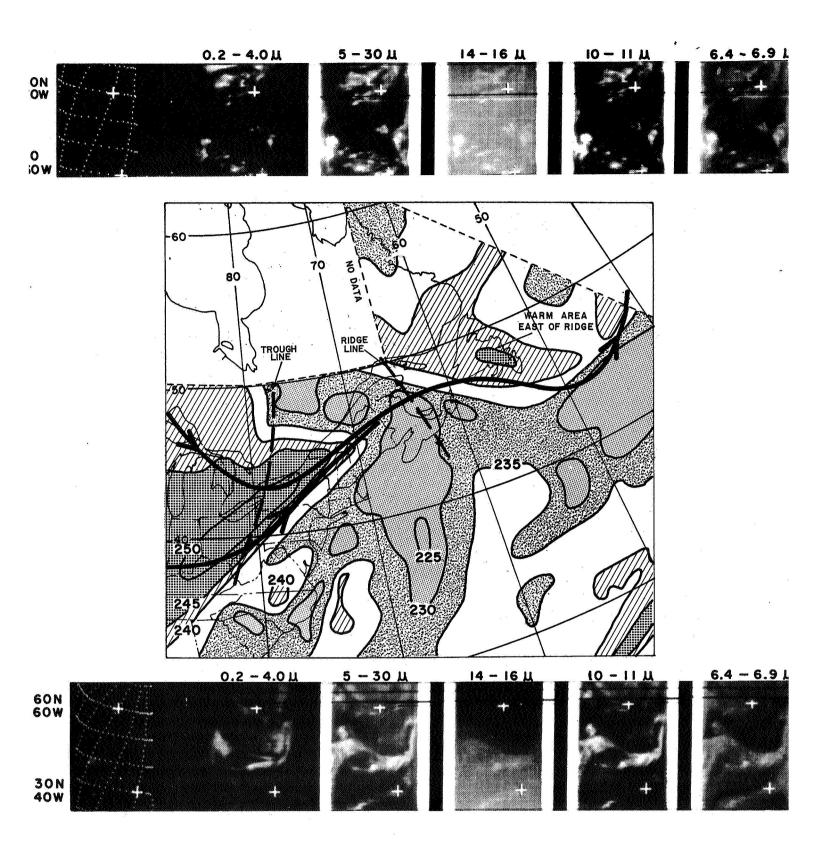
Figure 3-9a Analysis of 6.4-6.9μ Channel T_{bb} for 10 June 1966,
Nimbus II MRIR, Orbit 350 at 1415 GMT (top) and
Orbit 351 at 1603 GMT (bottom).
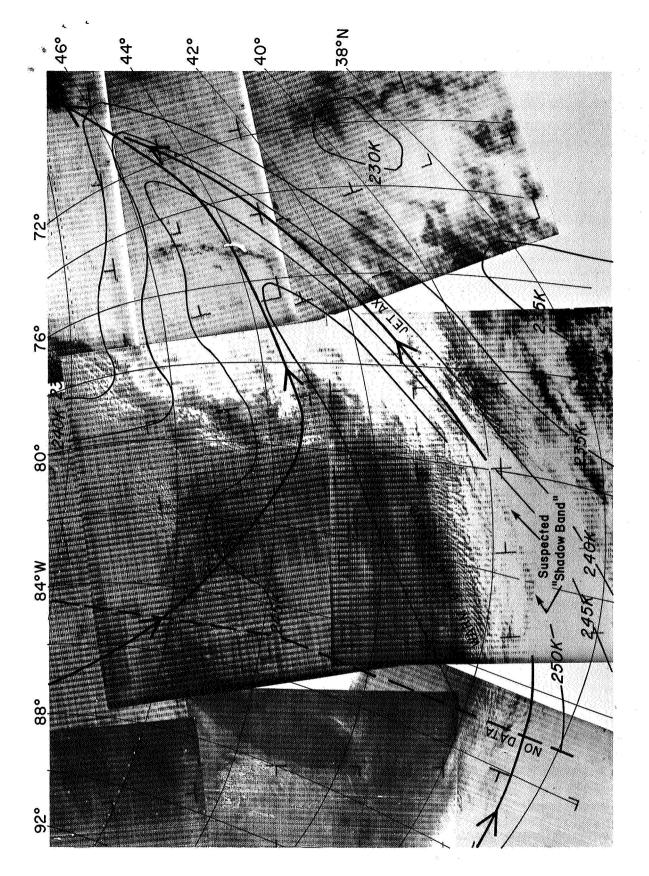
Figure 3-9b   Nimbus II AVCS Photograph, Orbit 351, 1630 GMT, 10 June 1966.   (6.4-6.9μ T_{bb} Analysis from Fig. 3-9a is superimposed.   Note apparent "shadow band" on equatorward side of warm >250K T_{bb}.)

—— 500 mb contour heights

- - - - Isotherms

(a)   **(b)**   **(c)**
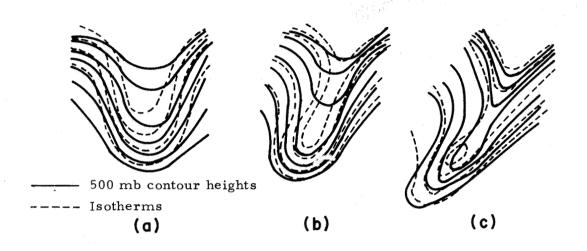
Figure 3-10 Schematic Representation of the Formation of a Shear
Line in the Upper Level Wind Field.
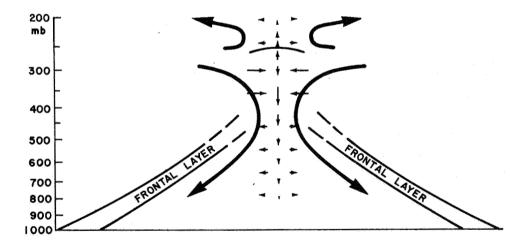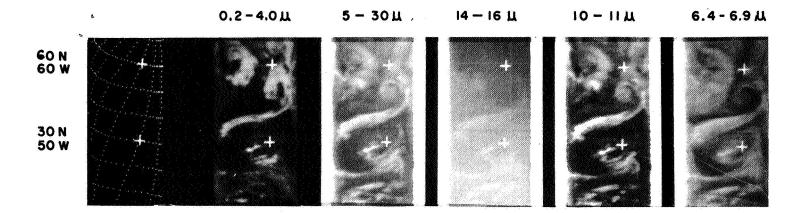
Figure 3-11 Schematic Representation of Vertical Motion and Divergence
During the Formation of a Shear Line. (Vertical and hori-
zontal velocities are proportional to the length of the arrows
Hsieh, 1950.)
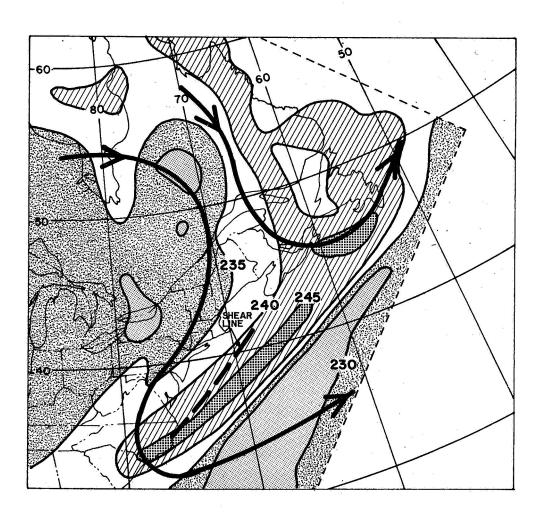
Figure 3-12 Analysis of 6.4-6.9μ Channel T_{bb} for 1440 GMT, 22 June 1966. Nimbus II, Orbit 510. (Note close agreement between the portion of the shear line and the warm >245K band of temperatures.)

channel. As is common in a situation of this type, wind speeds west of the trough were much stronger than those to the east. The axis of the warm area, from 42N, 63W to 34N, 79W, was apparently produced by subsidence along the shear line.

3.2.4 Baroclinic Storm Case, 23-25 May 1966

A low zonal index characterized the flow over North America during this period. On 23 May (Fig. 3-13) there was a strong trough near the Canadian Rockies and a ridge over Hudson Bay. During the following two days (Fig. 3-14 and 3-15) the trough axis changed from a north-south direction to a northwest-southeast orientation, with the sharpest streamline curvature over or near the Great Lakes. The ridge axis to the east rotated in a similar manner with the final pattern (Fig. 3-15) appearing much like an omega block. A surface low pressure and frontal system associated with the trough moved from central Canada to Hudson Bay, where it became stationary and began to occlude.

Excellent 12 hourly satellite coverage was available for this case. Figures 3-16 to 3-21 show the MRIR strip charts and digitized data taken at the times shown. The enlarged pictures show the $6.4-6.9\mu$, $10-11\mu$ and $14-16\mu$ channel data, taken from 1:10M digitized maps. The "time corrected" jet stream axis and surface fronts are superimposed on each of the digitized maps.

3.2.4.1 General Pattern Seen by MRIR

Many features relating to the developing baroclinic storm are shown in the MRIR data. Colder temperatures in the $6.4-6.9\mu$ and the $10-11\mu$ data clearly show the intense cloud development over the central United States. This narrow band of cloud was produced by the cold front and a squall line that developed on 24 May.

Despite the presence of a well organized low center the classic vortical cloud field did not appear in this case. A rather disorganized field of clouds east of the low center was the only recognizable cloud feature near the vortex center.

Perhaps the most significant feature of the general pattern is the information revealed in the $6.4-6.9\mu$ data over regions to the west of the cold front. This area was generally cloud free, as reflected by the generally warm $10-11\mu$ channel temperatures. In such clear regions, variations in the $10-11\mu$ channel temperatures more properly reflect differences in surface temperature.

(a)

(b)

(c)
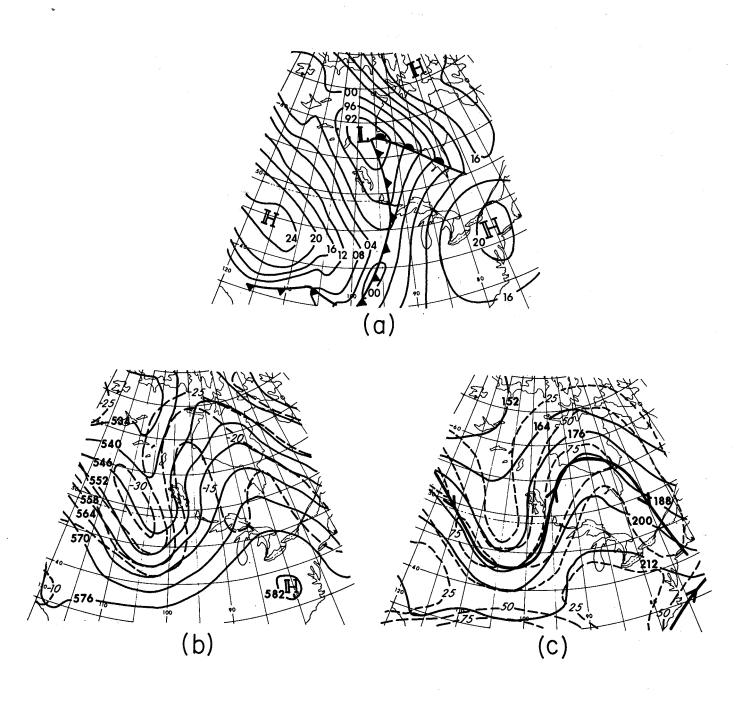
Figure 3-13 Surface (a), 500 mb (b) and 200 mb (c) Analyses for 1200 GMT,
23 May 1966.
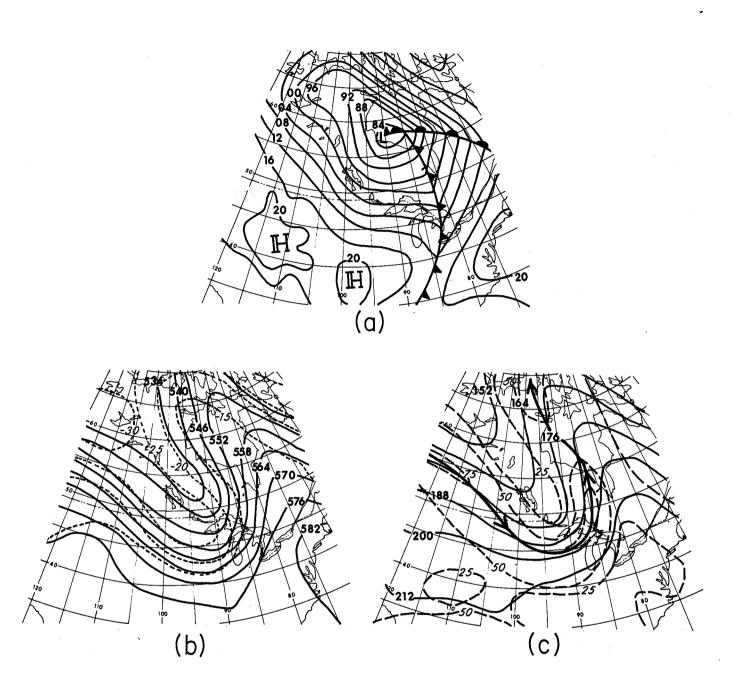
Figure 3-14 Surface (a), 500 mb (b) and 200 mb (c) Analyses for 1200 GMT, 24 May 1966.

(a)

(b)

(c)
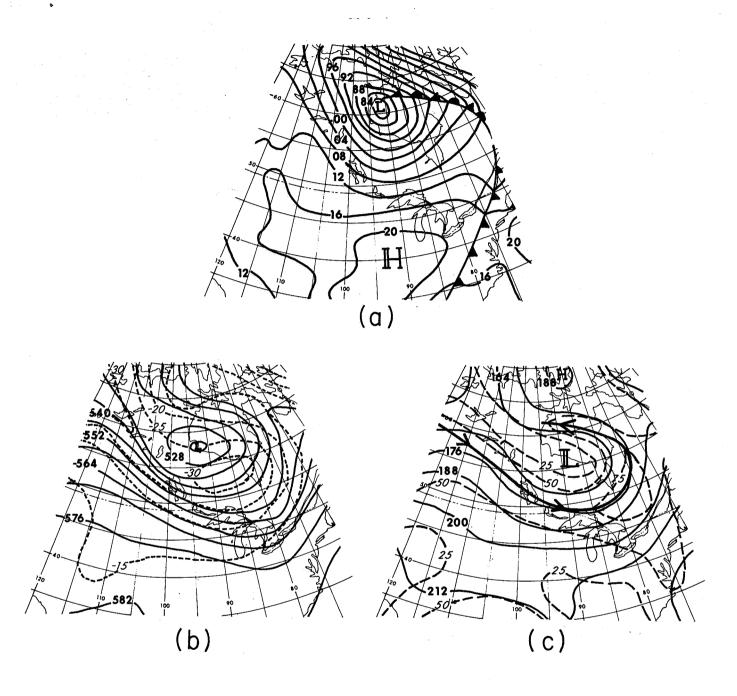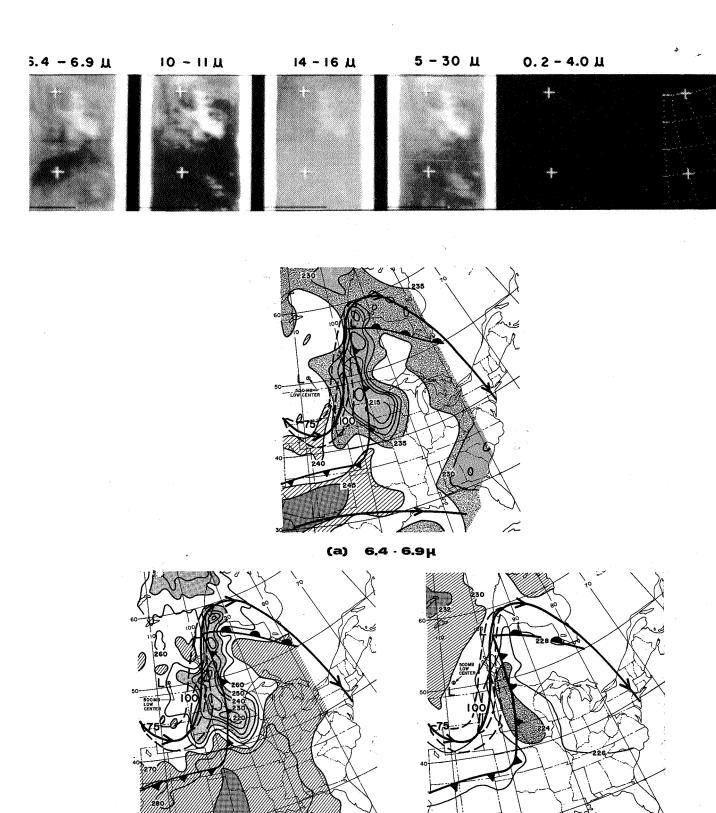
Figure 3-15 Surface (a), 500 mb (b) and 200 mb (c) Analyses for 1200 GMT,
25 May 1966.

5.4 – 6.9 μ   10 – 11 μ   14 – 16 μ   5 – 30 μ   0.2 – 4.0 μ

60N
100W

30N
110W

(a)   6.4 · 6.9μ

(b)   10 · 11μ

(c)   14 · 16μ

Figure 3-16   Analysis of the 6.4-6.9μ (a), 10-11μ (b) and 14-16μ (c) Channel
Tbb's for 0650 GMT, 23 May 1966. Nimbus II, Orbit 107.
(Time corrected jet axes, surface fronts and 500 mb low center
are superimposed.)

0.2 - 4.0 μ   **5 - 30 μ**   **14 - 16 μ**   **10 - 11 μ**   **6.4 - 6.9 μ**

(a)   6.4 · 6.9 μ

(b)   10 · 11 μ   **(c)   14 · 16 μ**
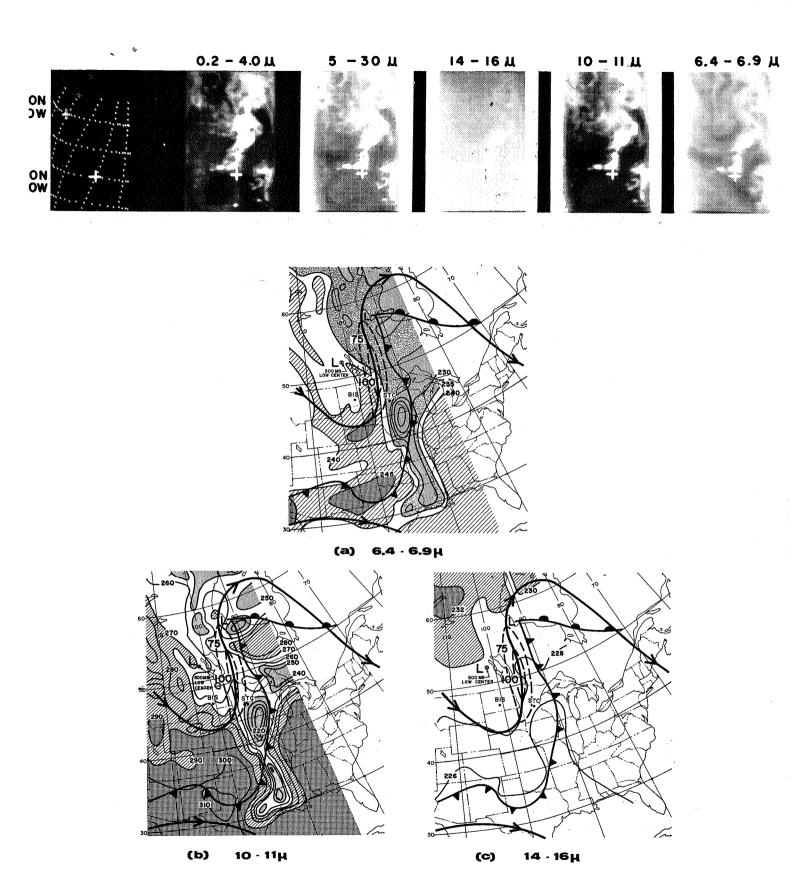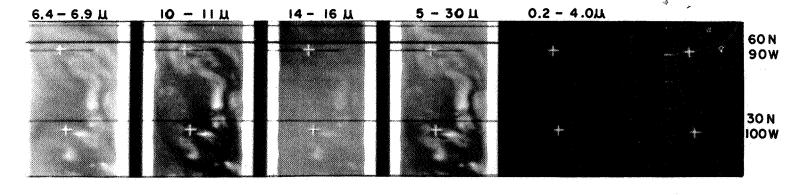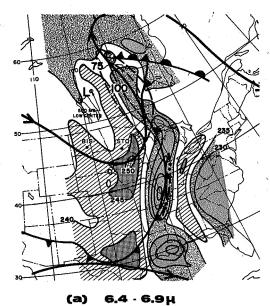
Figure 3-17   Analysis of the 6.4-6.9μ (a), 10-11μ (b), and 14-16μ (c) Channel
T_{bb}'s for 1713 GMT, 23 May 1966. Nimbus II, Orbit 112.

6.4 - 6.9 μ   10 - 11 μ   14 - 16 μ   5 - 30 μ   0.2 - 4.0 μ

60 N
90 W

30 N
100 W

(a)   6.4 - 6.9 μ
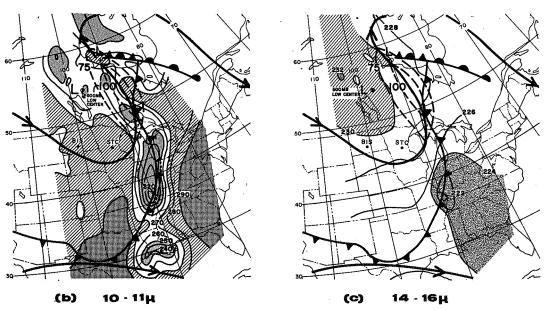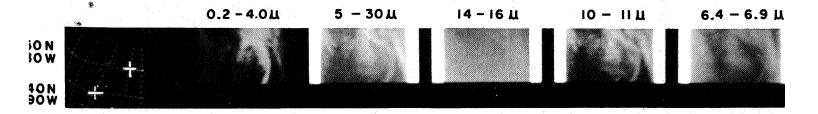
(b)   10 - 11 μ

(c)   14 - 16 μ

Figure 3-18   Analysis of the 6.4-6.9μ (a), 10-11μ (b) and 14-16μ (c) Channel
T_{bb}'s for 0618 GMT, 24 May 1966. Nimbus II, Orbit 120.

68

(a) 6.4 - 6.9μ
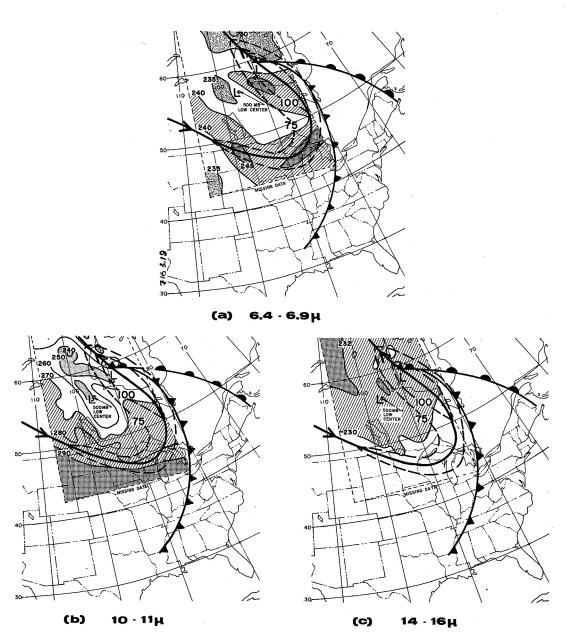
(b) 10 - 11μ

(c) 14 - 16μ

Figure 3- 19   Analysis of the 6.4-6.9μ (a), 10-11μ (b) and 14-16μ (c) Channel T_{bb}'s for 1645 GMT, 24 May 1966. Nimbus II, Orbit 125.

(a)   6.4 · 6.9 μ

(b)   10 · 11 μ   (c)   14 · 16 μ
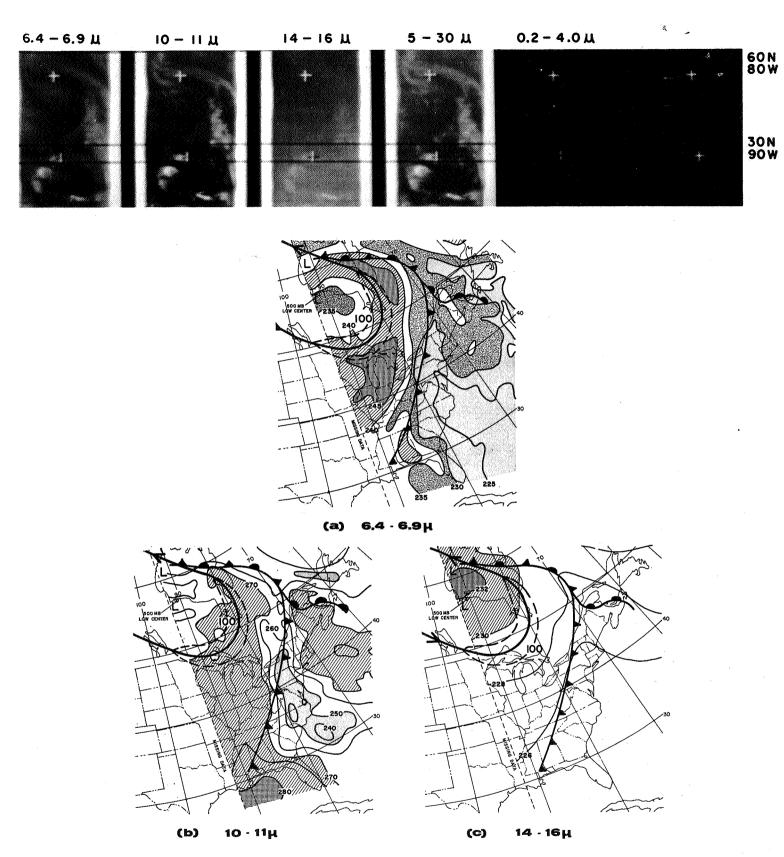
Figure 3-20   Analysis of the 6.4-6.9μ (a), 10-11μ (b) and 14-16μ (c) Channel T_{bb}'s for 0540 GMT, 25 May 1966. Nimbus II, Orbit 133.

70
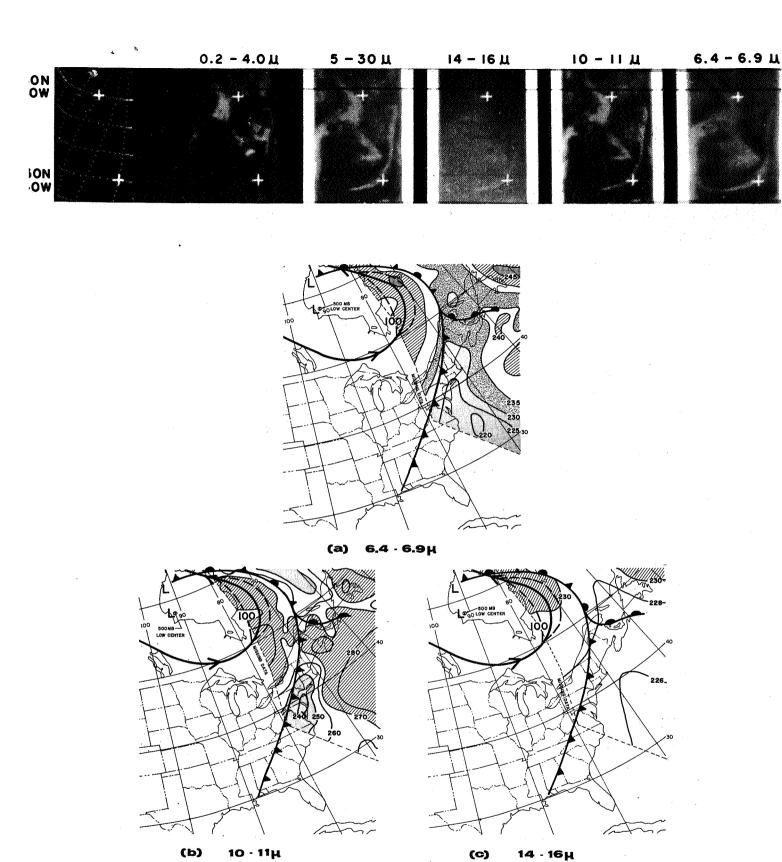
Figure 3-21 Analysis of the 6.4-6.9μ (a) 10-11μ (b) and 14-16μ (c) Channel T$_{bb}$'s for 1414 GMT, 25 May 1966. Nimbus II, Orbit 137.

In Figures 3-16 to 3-21, however, it may be seen that the 6.4-6.9μ data show a very marked region of warm temperatures at the trough line of the upper level flow. This warming pattern gives a fairly clear indication of strong descent to the rear of the baroclinic storm. This feature of the storm could not have been specifically deduced from either the 10-11μ data or visible data, since it is not directly depicted by the cloud field. (Although the nearly complete absence of cloud in this region might have led to some inferences in this regard.)

3.2.4.2 Temporal Changes and the Conjoint Relationship of the MRIR Channels

This case demonstrates interesting changes in the MRIR data as the storm progressed and deepened. At 0650 GMT on 26 May, the pattern (See Fig. 3-16) shows a fairly well organized cold 6.4-6.9μ T_{bb} region along the frontal position south of the low center in Canada. Warm 6.4-6.9μ T_{bb} values over Wyoming, although only slightly greater than 240°K, conformed to a region of negative vorticity advection (see Section 3.2.4.3). The 10-11μ data show an analogous T_{bb} distribution, but the region of descending motion behind the cold front does not have the detail shown in the 6.4-6.9μ data. As is generally true, the 14-16μ data were characterized by a lack of small detail indicating that this channel was sensing only the gross motions associated with the storm system. The region of cold temperatures ($< 224^{\circ}$K) in the 14-16μ channel was probably caused by the contamination from very high clouds along the frontal surface. It should be noted however, that this was also a region with a very high tropopause which could also produce the colder temperatures. This contention is supported by the observation that a tongue of colder 14-16μ temperatures extends well north of the very active cloud development and nearly parallels the jet stream axis in an area where a high tropopause should be present. Warmer 14-16μ temperatures were occurring over the tropospheric low, indicating sinking of the tropopause and stratospheric subsidence.

By 1800 GMT, 23 May (Fig. 3-17) the cold temperatures, representing the cloud tops along the front had organized into an elongated band with very intense convective activity indicated over Iowa. The warm 6.4-6.9μ T_{bb} at the trough line, now over Nebraska, had increased to greater than 245°K. The 240°K and warmer area had developed into a cyclonically curved band paralleling the jet stream axis.

By 0615 GMT, 24 May (see Fig. 3-18) the 6.4-6.9μ warm region near the trough has increased still further in size and intensity, with temperatures greater than 240°K now extending northward, on a line parallel to the jet stream axis, to a position just west of the surface low. The very cold temperatures seen in all channels over Illinois reflect the appearance of a squall line on the surface analysis.

The area covered by, and the intensity of the 6.4-6.9μ warm temperatures continued to increase as the storm matured. One probable reason for this pattern intensification might be that the subsidence at the trough, and along the jet stream, continued to introduce very dry air into the upper troposphere. As the storm matured a larger and larger region was affected by the drying, until the storm was occluded and subsidence was less active. Subsidence would normally be expected over a larger region of the cold air mass than was indicated by the narrow bands of 6.4-6.9μ warm temperature. This was shown by the large warm (clear) area in the 10-11μ data. It is speculated that cirrus, in regions of only moderate descent, contaminated the 6.4-6.9μ data, providing a possible explanation as to why a larger subsidence region was not observed. High level cirrus advected into the region of the cold air mass from other active baroclinic systems or around the northern side of the same storm could have contaminated the 6.4-6.9μ data over the cold dome, where only moderate subsidence was occurring.

Aerological soundings taken at St. Cloud, Minnesota, and at Bismark, North Dakota, indicated the differences between the atmospheric structure in the region of strong 6.4-6.9μ warming and the cooler temperatures further to the west of the cold front. Figures 3-17 and 3-18 show that St. Cloud was very near the warmest 6.4-6.9μ temperatures at about 0600 GMT, 24 May, while Bismark was under a region of temperatures colder than 240°K. The soundings in Figure 3-22 show the atmospheric structure over St. Cloud at 0000 GMT and 1200 GMT, 24 May. While the warmest temperatures were over St. Cloud between these two times, the soundings still show the strong subsidence inversion and dry upper troposphere necessary for very warm 6.4-6.9μ temperatures. The 0000 GMT, 24 May sounding at Bismark (see Fig. 3-23) shows a fairly dry upper troposphere but there is a moisture increase just above 400 mb, indicating the presence of a high level moisture or cirrus cloud layer. This was substantiated by Bismark's surface report of one-eighth cirrus at 0000 GMT, 24 May. This increase in moisture, and the presence of cirrus near the layer of peak 6.4-6.9μ contribution, would certainly produce the cooler temperatures seen by the 6.4-6.9μ channel. The cirrus was apparently not dense enough to be detected by the 10-11μ channel.
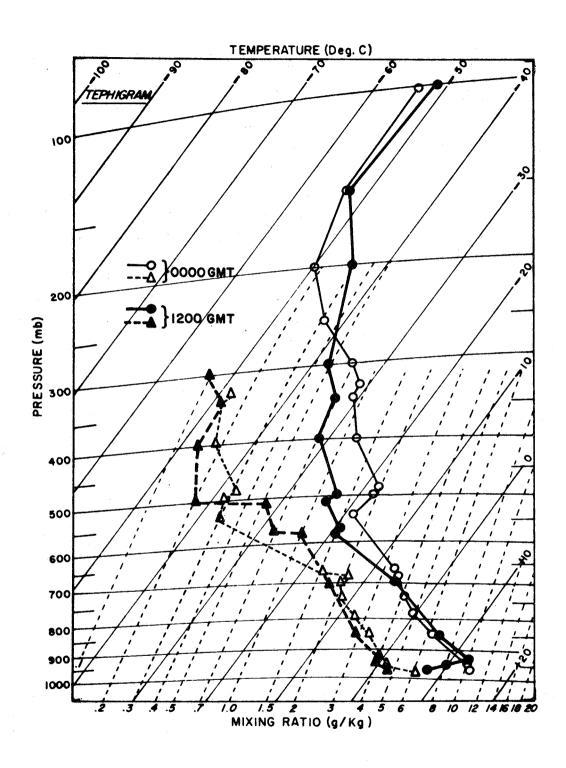
Figure 3-22 Soundings for St. Cloud, Minnesota, 24 May 1966.
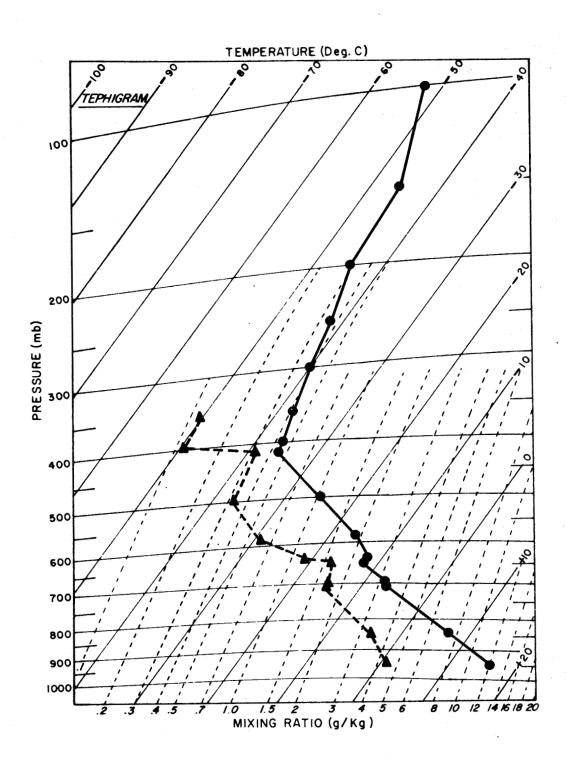
Figure 3-23   Sounding for Bismark, North Dakota, 0000 GMT, 24 May 1966.

In later stages of the storm, when a cut-off low was formed, the cirrus was advected around the closed low and not over it, effectively eliminating the cirrus source. The remaining moderate subsidence could have been strong enough to clear the upper troposphere of any remaining ice crystals, producing an area of increasing T_{bb} values to the rear of the storm.

Although the 14-16μ channel receives its maximum radiance from a layer in the stratosphere, the patterns shown in Figures 3-16 to 3-21 indicate that it is still useful for locating and analyzing atmospheric motions near the tropopause. The strip chart presentation of the 14-16μ data generally lacks the relatively large grey scale contrasts seen in other channels. However, when a deep tropospheric cyclone is present, the lowering of the tropopause level creates a region of warmer temperatures that are detected by the 14-16μ channel.

The gradient between the 14-16μ warm and cold regions is depressed southward along tropospheric troughs, and is found further to the north over ridges, following the general planetary flow pattern. The juxtaposition of warmer 14-16μ temperature regions over low level baroclinic storms provides a unique method of locating areas of active development. Since the gradient is also closely related to the tropopause break, it can be used to confirm locations of jet streams as determined from warm bands in the water vapor data. In this case, the region of warmer 14-16μ temperatures followed the progression of the storm system as it moved from the Rocky Mountains to Hudson Bay. The stronger gradient, mentioned above, was seen near the jet stream axis to the east of the warmer area, with a weaker gradient to the south. The lack of a tighter gradient in regions away from the cumulonimbus cloud area may be due to the averaging processes used to produce the digitized maps. Indeed the pictorial representations of the 14-16μ data, seen in the strip charts, seem to show a clearer delineation between the warm and cold regions.

Further studies using the non-averaged data from the 14-16μ channel are in order. If the apparent gradient does occur at the tropopause break, then the conjoint use of the 6.4-6.9μ and 14-16μ data provides a unique method of locating maximum wind bands as well as developing extratropical storms. These matters are discussed in more detail in the model development section of this report (see Section 3.3.1).

3.2.4.3 Vorticity Considerations

The strong sinking motions responsible for the warm bands of 6.4-6.9μ T_{bb}'s discussed in the earlier jet stream cases were caused by a combination of the wind shear ($\partial V/\partial n$) and the curvature of the stream lines (K_s) in the vicinity of the jet axis. The relationship of these terms is demonstrated in the vorticity advection relationship (see Equation 3).

Vorticity advection is closely related to vertical motions, providing a good indication of areas of existing or probable cyclonic development. It will be recalled that the jet stream cases of 26 June and 10 June each had a wind maximum near an area of maximum curvature. In the developing baroclinic storm case shown in Figures 3-16 to 3-21, the jet axis had a very sharp cyclonic curvature, but with the wind maximum displaced downstream from the trough. The curvature term of the vorticity equation was dominant near the trough line, leading to a maximum of negative vorticity advection at the trough line, and hence strong subsidence in that region. Vorticity advection (A_Q) was calculated for 1200 GMT, 23 May, using Equation (3), and the resulting pattern is shown in Figure 3-24. Very strong positive vorticity advection is found near the inflection point east of the trough with a region of negative vorticity advection near the point of maximum streamline curvature in the trough. This pattern compares favorably with that seen in the 6.4-6.9μ data. The very warm temperatures indicating strong subsidence are found near the trough line, and the very cold temperatures are related to the intense cloud development associated with the positive vorticity advection.

3.2.5 Discussion

The cases presented in the foregoing sections demonstrate that measurements taken by the Nimbus II MRIR radiometer are very useful for determining and analyzing the structure of the atmosphere. If the sensors are assessed in terms of their ability to add new information about the synoptic patterns not obtainable by other means, the water vapor (6.4-6.9μ) channel is by far the most valuable.

In addition to dense middle and high level clouds, the 6.4-6.9μ channel senses concentrations of water vapor and ice crystals not otherwise observed. Because water vapor and ice crystal concentrations are sensitive to vertical and horizontal motions at high levels, the 6.4-6.9μ channel provides a good indicator of atmospheric motions.

77
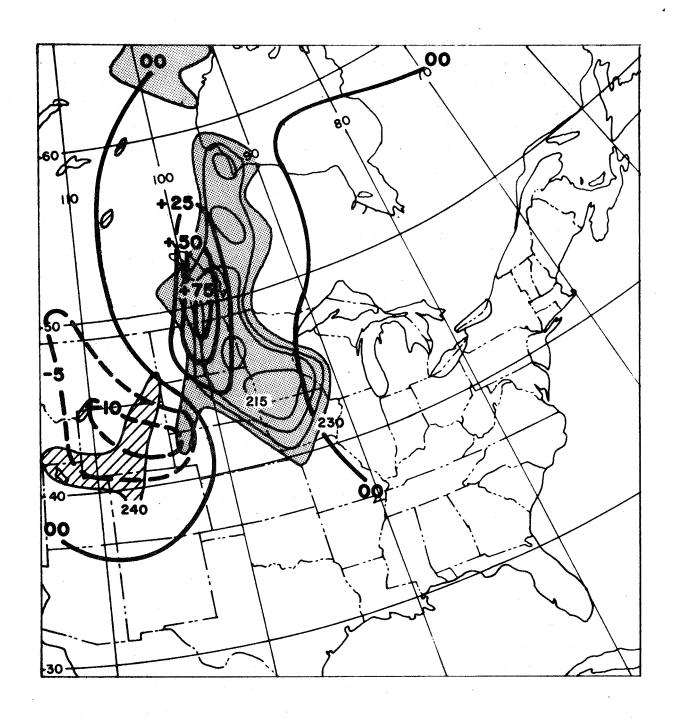
Figure 3-24 Vorticity Advection Pattern (hr^{-2}) for 0600 GMT, 23 May 1966
(6.4-5.9μ Channel T$_{bb}$ analysis for 0650 GMT superimposed,
see Fig. 3-16.)

Warm bands in the 6.4-6.9μ pattern correlate very well with the position of some portions of the jet stream axis. Various combinations of wind shear and streamline curvature produce regions of strong downward, as well as upward, vertical motion in accordance with the vorticity advection. Based on these relationships, subsidence can be expected along the leading (eastern) edge of ridges, and to the poleward side of the jet axis near and downstream from troughs. These regions show the expected 6.4-6.9μ warm areas. The warmest temperatures, and the regions of strongest subsidence, are found nearly parallel to the jet axis near the trough line. This is in agreement with past studies, which have shown this to be a region where very dry stratospheric air is introduced into the troposphere along the baroclinic zone under the jet stream.

In apparently cloudless areas further from jet streams, the 6.4-6.9μ temperatures are generally colder. This indicates that thin cirrus or high level layers of moisture, not otherwise observed, are being detected. The ability of the 6.4-6.9μ channel to sense these invisible layers, thereby allowing inference of upper tropospheric vertical motions, makes it uniquely adaptable for upper tropospheric research.

The importance of the 6.4-6.9μ measurements to deductions of atmospheric motion from satellite observations cannot be overemphasized. In the middle and upper troposphere it provides essentially the same information, with regard to upward vertical motions strong enough to produce clouds, as the 10-11μ and visible data. In the absence of cloud however, the 6.4-6.9μ data can be used to infer both the intensity and sign (upward or downward) of the vertical motion field in the upper troposphere from spatial and temporal variations of temperature. Thus, in cloud free regions, they provide data not specifically present in other satellite observations.

When interpreting the 6.4-6.9μ data, the possibility that high level cirrus clouds have contaminated the measurements must be considered. There is evidence that cirrus can be advected for great distances in the absence of strong subsidence. This cloud may produce a T_{bb} colder than that which would be expected from the ambient water vapor in the upper troposphere. Since the upper tropospheric mixing ratio is related to vertical motions at the same levels, the presence of cirrus may produce a false estimate of the mixing ratio. Upward vertical motions that were not actually present might therefore be inferred from cirrus contaminated data.

79

It is unlikely that cirrus will remain in regions of strong subsidence, and regions of strong ascent will produce dense high clouds that are defined by very cold T_{bb} values in both the 10-11μ and 6.4-6.9μ data. This would indicate that cirrus is a problem only in regions of moderate vertical motion, and in fact, may tend to enhance areas of strong subsidence by producing a sharper gradient of T_{bb} between areas of strong descent and only moderate vertical motions in either direction. The problem of cirrus contamination has not been fully resolved, and certainly deserves more attention in future research

The 14-16μ channel senses changes of the temperature structure of the lower stratosphere, and is particularly well suited for observing changes in tropopause height. The lowering of the tropopause over an extratropical cyclone can be correlated with warmer 14-16μ temperatures, and the break formed between the high tropical tropopause and the lower polar tropopause appears as a sharper gradient of 14-16μ temperatures.

When this information is used in conjunction with 6.4-6.9μ data with both showing warming due to strong subsidence near the jet stream, and its associated baroclinic zone, positive identification of areas of intense baroclinic activity can be made.

3.3   Jet Stream Model

From what was learned in the preceding case studies, it has been possible to develop a tentative model of the relative configurations of the jet stream and the warm bands seen in the water vapor clouds. This model, and a more detailed analysis of its significant regions, is presented in the following sections.

3.3.1   Tentative Model

The 6.4-6.9μ patterns in the previous case studies agreed well with the expected vertical motion fields near jet streams. Regions of ascent appeared cold because of the associated cloud field, while subsidence areas were characterized by very warm temperatures. For jet streams having fairly uniform sinusoidal flow patterns, these regions of warm and cold temperatures will generally occur at the same positions relative to the jet axis and the trough and ridgelines.

In developing the model, the following assumptions were made:

1.   Upper tropospheric vertical motions can be correlated with $6.4-6.9\mu$ warm areas where descent has occurred, and with cool areas where ascents have occurred.

2.   Very dry stratospheric air moving under the jet axis and along the associated baroclinic zone will be detected by the $6.4-6.9\mu$ channel.

3.   The strongest downward vertical motions occur near the jet stream axis, and are controlled by the streamline configuration and shear.

The model is shown in Figure 3-25. It corresponds most nearly to the pattern observed with the polar front jet stream, when the associated baroclinic zone extends to the surface.

The warm band near and usually east of the trough line (in Region A) will normally be warmer (darker) and narrower than the band in Region B. The width of the warm band is largely dictated by the presence of the clouds that form the cold area to the equatorward side of the jet axis.

The warm area east of the ridge generally is not as well organized as the more intense band near the trough. At times it may even appear as only a group of small warmer areas along the axis of a generally warm region.

The upper level dynamics necessary to produce strong downward vertical motions are also present along the subtropical jet axis. However, since the associated baroclinic zone is confined to upper levels, subtropical jet streams do not always develop the active cloud line necessary for giving a sharp equatorward boundary to the warm band near the trough. Because of this difference in the baroclinic zones the bands associated with the subtropical jet stream are generally wider, and extend for much greater distances along the band of strong winds.

The model shown in Figure 3-25 does not consider the effect of the isotach maximum location along the jet axis. Variations in the wind shear along the different jet axes may produce variations in the vertical motion field. In general, however, the curvature of the streamlines will be the dominant feature and the shear term tends only to intensify or slightly shift the basic pattern.

It should be remembered that the warm bands, regardless of where they occur, are manifestations of the upper tropospheric vertical motion field. They are related to jet streams only because strong vertical motions almost always occur near regions of maximum wind. A region where downward vertical motion of lesser intensity has been taking place for several days may also produce the conditions

81
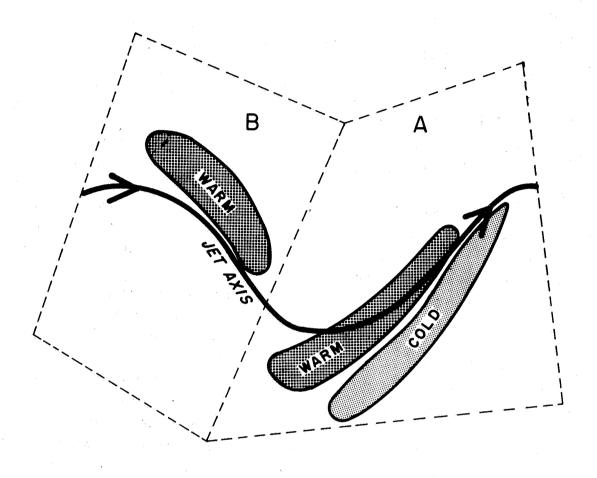
Figure 3-25 Schematic of Tentative Polar Front Jet Stream and 6.4-6.9μ
Warm Band Model Showing the General Configuration of the
Warm Areas and the Jet Axis

necessary for warm effective blackbody temperatures in the 6.4-6.9μ data (see for example, the warm area south of Lake Erie in Fig. 3-5). Therefore, the existence of a warm band, in and of itself, is not sufficient evidence for locating a jet stream. Examination of many MRIR 6.4-6.9μ observations over various parts of the world suggests that the warm areas can be separated into two general categories: (1) those associated with maximum wind bands, and (2) those associated with large high pressure areas where broad scale subsidence is present. As a first approximation, it appears that the two types can be separated on the basis of shape; i.e. elongated bands seem to be related to the dynamics associated with strong wind bands, while those related to large high pressure regions are more rounded. An example of this shape difference is shown in Figure 3-5. The warm band along the jet axis shows the elongated shape, while the one located south of Lake Erie (produced by the subsidence in the anticyclone over the eastern half of the United States) is more rounded in appearance.

As suggested earlier (see Section 3.2.5), a more satisfactory method of identifying the two types of warm areas may be the conjoint use of the 14-16μ channel and the 6.4-6.9μ channel. The 14-16μ sensor receives its maximum response from radiation emitted by CO_2 in the lower stratosphere, (see Section 2.6) although the data are at times contaminated by very high cumulonimbus or other clouds penetrating to levels near the tropopause. Two aspects of the 14-16μ channel data may make it useful for delineating jet stream associated warm bands appearing in the 6.4-6.9μ data.

1.   Lifting along the baroclinic zone associated with the jet stream is an ideal mechanism for producing clouds with tops near an otherwise high cold tropopause. Rather thin lines of cold T_{bb}, appearing in the 14-16μ imagery, are then probably associated with active baroclinic zones in the troposphere. A band of cold T_{bb} values, due to such clouds, may be seen in the 14-16μ imagery shown in Figure 3-5.

2.   Sinking motion in the stratosphere, on the cyclonic side of the jet, will appear as a rather broad region of warmer 14-16μ temperatures. These sinking motions, and hence the warm temperatures, at times lead to a clearly discernible gradient along the tropopause break.

Both of these features are closely related to jet stream positions, making it possible, by comparing the 6.4-6.9μ pattern with the 14-16μ pattern, to differentiate between the extratropical jet stream produced warm bands and those related to other phenomena.

3.3.2   Correlation of Warm Bands and Jet Streams

The model of the relationships between jet stream and the $6.4-6.9\mu$ pattern shown in Figure 3-25 is divided into two regions, with the configuration in Region A being more persistent and easier to identify. As a test of the model, portions of jet streams similar to that shown in Region A were analyzed to determine if the $6.4-6.9\mu$ patterns were consistent enough to be reproduced in the mean. This section describes the procedure and results of that investigation. All the cases selected were over the United States and Canada and were, of course, limited to the summer season of 1966. These factors should not unduly restrict the results, as the relationship is based on dynamic and kinematic relationships that remain reasonably constant for all seasons.

As previously noted, the vertical motion field near a jet stream is dependent on such factors as: (a) streamline curvature, (b) locations of isotach maxima and (c) locations of regions of strong shear. Since the $6.4-6.9\mu$ patterns are related to vertical motions, which are in turn highly sensitive to changes in, and different combinations of, the above factors, care was exercised in selecting cases for this statistical analysis. Only jet streams having moderate cyclonic curvature, and maximum winds near 100 knots at the point of maximum curvature, were selected.

3.3.2.1   Approach

Six cases, having jet stream configurations as described above, were selected. The coordinate system (see Fig. 3-26) used the isotach maximum along the jet axis as the center. The jet stream axis served as the abscissa, with the ordinates positioned normal to the jet axis at all points (i.e., the coordinate system along the jet axis was orthogonal but not rectilinear).

The $6.4-6.9\mu$ data were transferred to Lambert Conformal maps. Jet stream and isotach positions, corrected for the time difference between the conventional observations and the satellite pass, were superimposed on the $6.4-6.9\mu$ data.

Based on the following criteria, three points along the jet axis (see Fig. 3-24) were selected:

1.   The first point, located at the center of the isotach maximum along the axis, served as the center of the coordinate system.

2.   Points upstream and downstream from the central point were determined by taking 75% of the maximum wind along the axis. The resulting values defined unique points along the abscissa, upstream and downstream from the center.

84
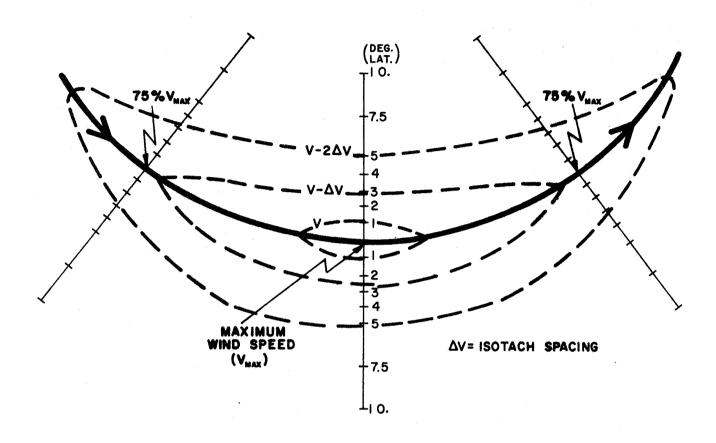
Figure 3-26 Coordinate System Used to Extract Wind Speeds and 6.4-6.9μ
Temperatures Relative to a Moderately Curving Jet Axis in the
Region of Maximum Wind Speed.

This procedure provided points along the jet axis that were dependent on the relative magnitudes of the wind speeds. Lines normal to the jet stream axis, at the three points defined above, were then constructed. The wind speeds and estimated blackbody temperatures were recorded at the axis, and along each of the three lines at 1°, 2°, 3°, 4°, 5°, 7.5° and 10° of latitude on both sides of the jet axis. The distance of the surface front from the jet axis, at the three points, was also recorded. Values from the individual cases, at the points defined by the above coordinate system, were averaged to determine the mean configuration of the 6.4-6.9μ pattern, and the mean position of the surface front, relative to the jet axis.

3.3.2.2 Derived Pattern

The mean values of wind speed and blackbody temperatures at each point of the coordinate system were plotted and analyzed. The resulting pattern is shown in Figure 3-27. This pattern is in good agreement with the patterns observed in the individual cases.

The terms used to describe the 6.4-6.9μ T_{bb}'s of various areas are relative, but serve to indicate what is observed in the strip chart presentation of the 6.4-6.9μ MRIR data. Areas labeled as warm (dark) have effective blackbody temperatures greater than 245°K, cold (white) areas represent temperatures less than 235°K. "Dark" and "white" refer to the appearance of the areas in strip chart pictures. The elongated warm band, which splits near the entrance region of the isotach maximum, is nearly parallel to the jet stream axis. Splitting of the warm band, as shown in the mean pattern, was observed in only a few actual cases. The fact that it appears in the mean pattern is probably due to the cases selected and the averaging used. It is possible that the large variability of the warm band position near the entrance region of the jet maximum produced a fictitious splitting of the warm band, and one should not be surprised if the feature is found in only a limited number of actual cases. However, when splitting is observed, it is most probably caused by the presence of cirrus cloud, opaque in the 6.4-6.9μ channel, near the jet stream axis (Whitney et al., 1966). When this occurs, the warm band appears to be split near the entrance region of the wind maximum.
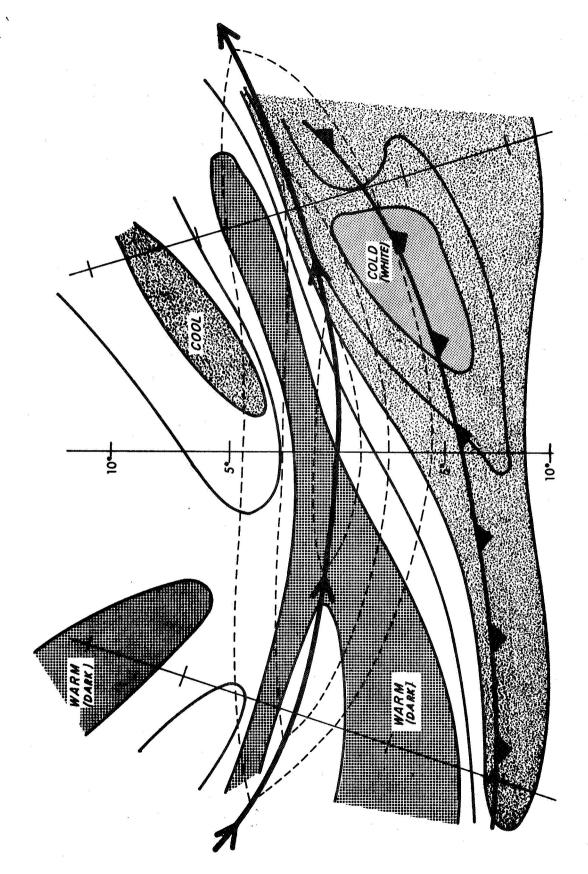
Figure 3-27 Mean Pattern Derived from Coordinate System. (Warm (dark) areas represented 6.4-6.9μ T_{bb} values generally >250K, cold (white) areas include T_{bb} values generally <230K, cool areas are between 230K and 240K.)

87

Colder temperatures are found along the surface frontal position, on the anticyclonic side of the jet stream, and because of higher clouds near the point of occlusion they become more intense near the exit region of the isotach maximum.

This model applied only to situations when the jet stream axis has moderate cyclonic curvature, with the maximum wind located near the maximum curvature. As was pointed out earlier, the pattern is highly sensitive to the vertical motion field generated near the jet stream, and this field can be altered by simply shifting the region of maximum winds, and hence the location of maximum shear, along the jet stream axis, or by changing the curvature of the streamlines. This will in turn lead to a greater or lesser modification in the radiation pattern shown in Figure 3-25.

3.4 Tropical Applications

Meteorological phenomena of the tropics have been, in general, poorly observed and understood. Meteorological satellites are now providing, on a regular basis, the observations required for the improved understanding and subsequent modeling of both large and small scale tropical phenomena.

The Nimbus II satellite provided an improved view of the field of composition and motion of the tropics through the infrared "eyes" of the Medium Resolution Infrared Radiometer (MRIR). The 6.4-6.9μ channel permitted a novel look at the integral of composition and motion in the tropical atmosphere, i.e., middle and upper troposphere, where features significant to both general tropical analysis and tropical storm development occur. The following two sections will demonstrate the potential of the 6.4-6.9μ observations for:

1. Delineation of major baroclinic features of the tropical upper troposphere, i.e., upper tropospheric baroclinic cyclones and the subtropical jet stream.

2. Describing certain aspects of the dynamics of tropical storm development.

3.4.1 Upper Tropospheric Baroclinic Systems

The existence of cyclonic cells in the upper troposphere over the subtropical surface anticyclones during the summer season, has been acknowledged for some time. Only since the advent of satellites has the overall character of this zone been examined in any detail. Sadler (1962) presented examples of TIROS photographs over the Pacific for this zone, which showed trains of cyclonic cloud producing vortices which only rarely had any surface reflection. Sadler (1967) proposed that these

cyclone trains in the upper troposphere were responsible for many of the typhoons which had heretofore been assumed to develop from easterly waves. Ramage (1962) and Orgill (1963) showed that extratropical cyclonic activity was, in part, responsible for changes in intensity of these cyclonic cells through downtrough advection of energy. Merritt (1967) has tentatively shown a correlation between the location of upper tropospheric cyclones in the Atlantic and ITCZ type hurricane development. These various studies suggest that accurate definition of the field of motion of the upper troposphere is significant to accurate prediction in the tropics.
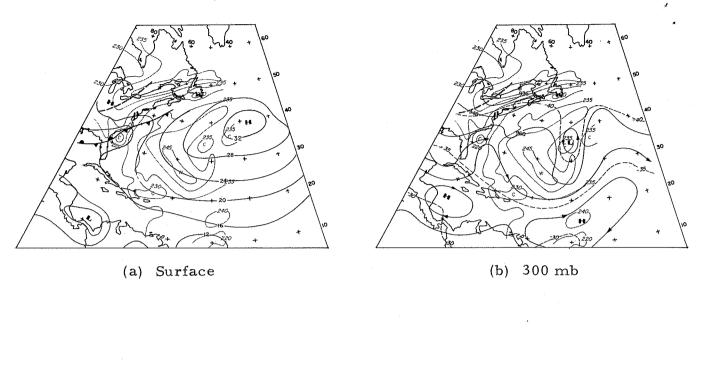
3.4.1.1 Applications of 6.4-6.9μ Data To Upper Tropospheric Analysis

The general aspects of the circulation pattern over the subtropical and tropical Atlantic between 19 and 21 June 1966 are fairly well depicted by the analysis for 20 June (see Figs. 3-30 and 3-31).

The synoptic features significant to this case are those in the area between 10°N and 50°N from the United States coastline to about 35°W. Note in particular the cyclonic circulation at both 300 and 200 mb, almost directly above the surface subtropical anticyclone. Note that the AVCS montage shows generally clear to scattered conditions in this area. The following discussion demonstrates how, and perhaps why, the 6.4-6.9μ observations provide a unique indication of the presence and level of intensity of this type of tropical upper tropospheric baroclinic cyclone.

3.4.1.2 1200 GMT, 19 June

Analyses for the surface, 300 mb, and 200 mb, and cloud observations, all at 1200 GMT, 19 June, are presented in Figures 3-28a, b, c, and d respectively. The digital mapping of the 6.4-6.9μ observation is superimposed on each analysis. Note that the band of T_{bb} values greater than 240°K along the United States' east coast parallel the Polar Front Jet, as described in Section 3.2 of this report. The "fish-hook" shaped pattern of T_{bb} values greater than 240°K where a direct indication of the divergence and associated descent occurring on the east side of the upper tropospheric ridge which was centered near 65°W at 35°N, at 200 mb. Confirmation of this implied descent is provided from the sounding at Bermuda for 1200 GMT, 19 June (Fig. 3-29). The deep dry layer between 850 mb and 200 mb was caused

89

(a) Surface

(b) 300 mb

(c) 200 mb

(d) Cloud observations

Figure 3-28   Surface (a), 300 mb (b), 200 mb (c), and Cloud Observations (d)
Analyses for 1200 GMT, 19 June 1966. (6.4-6.9μ Channel T_{bb}
superimposed.)

Figure 3-29 Sounding for Bermuda, 1200 GMT, 19 June 1966.

91

Figure 3-30 Surface (a), 300 mb (b) 200 mb (c) and Cloud Observations (d)
Analyses for 1200 GMT, 20 June 1966. (6.4-6.9μ Channel T$_{bb}$
superimposed.)

Figure 3-31 Montage of Nimbus II AVCS Photographs, ∼ 1200 GMT,
20 June 1966.

93

by subsidence throughout. Further indirect evidence is provided by the cloud observations beneath the area enclosed by the 240°K isotherm, which are presented in Figure 3-28d. The predominant cloud is a low type one (this is defined generally as fair weather cumulus, showing no vertical development).

East of the 200 mb cyclone center, we see small centers of T_{bb} values colder then 235°K. Discussions in Section 2.4 have pointed out that 6.4-6.9μ values which are 235°K or colder are almost invariably associated with multilayer cloudiness. The cloud observations in Figure 3-28d show that multilayer clouds did exist in this area. The probable cause of these clouds was upward vertical motion, due to advection of positive (cyclonic) vorticity poleward along the east side of the upper cyclone. The cool strip (less than 235°K) extending from 20°N, 50°W to 25°N, 40°W appears to be related to the Sub Tropical Jet stream (STJ) which had ar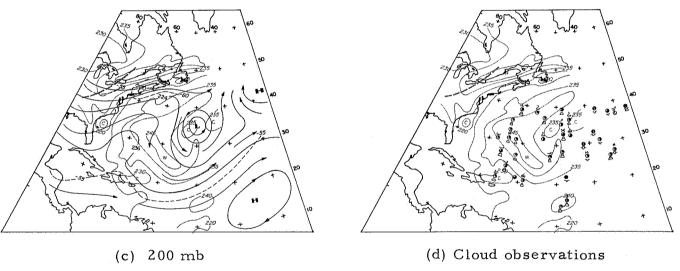rived around the south side of the cut-off baroclinic cyclone. The connection between this cool strip and the ITCZ region over the northeast coast of South America suggests advection of cirrus and/or moisture at upper tropospheric levels, from the ITCZ into the STJ.

3.4.1.3 1200 GMT, 20 June

Only very slight changes in the synoptic pattern occurred over the 24-hour period from 1200 GMT, 19 June to 1200 GMT, 20 June. The surface, 300 mb, 200 mb, and observed cloud analyses are presented as Figures 3-30a-d respectively, while Figure 3-31 shows a montage of Nimbus II AVCS photographs for approximately the same time. The digital mapping of the 6.4-6.9μ T_{bb} observations are superimposed on each. The changes in the 6.4-6.9μ pattern, while not great, are still significant. If it is assumed that the 6.4-6.9μ channel responds to changes in the moisture and temperature field induced by both advection and vertical motion, then the full synoptic change must have been more significant than is obvious from the differences between Figures 3-28 and 3-30.

Height change analyses (not reproduced) showed slightly increased contour heights to the west and north of the cyclone, near station Echo (35°N-48°W). These height increases appear to have been associated with increased ridging in the streamline pattern. Subsidence within this ridge was probably responsible for the warmer 6.4-6.9μ T_{bb} values near 39°N, 50°W. The translation of the "fish-hook" T_{bb} pattern to near 24°N, 47°W on 20 July was probably just that, i.e., translation of the existing pattern. The pattern could however have been influenced by some adjustment of the vertical motion distribution around the cyclone, due in part to some

94
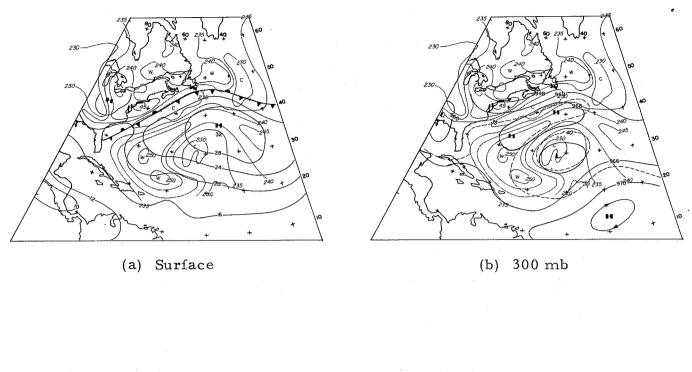
increase in the anticyclonic circulation at 300 mb, southeast of the 200 mb cyclone. The small area of $235^{O}K$ T_{bb}' s, centered at $30^{O}N$, $55^{O}W$ could have been related to vertical motion ahead of the 300 mb trough, or to a 200 mb cyclone forming to the southwest of the primary center. The cool strip of T_{bb} values less than $235^{O}K$ with a northern edge extending from $20^{O}N$, $60^{O}W$ to $18^{O}N$, $50^{O}W$ and to $25^{O}N$, $35^{O}W$, suggests that a weak STJ may have been in the area. The $235^{O}K$ value suggests that cirrus was in the suggested STJ area. The AVCS photograph in Figure 3-31 does not show the cirrus which is believed to have been present. The cold ($< 230^{O}K$) T_{bb} area extending northward from $10^{O}N$, $57^{O}W$ appears to have been a continuation of the cirrus advection from an ITCZ disturbance, as mentioned during discussion of the 19 June pattern. The warm ($> 240^{O}K$) T_{bb} area near $15^{O}N$, 40° to $50^{O}W$ lies along the center of the 200 mb and 300 mb equatorial anticyclone.

3.4.1.4   1200 GMT, 21 June

There were no significant changes from the overall 20 June synoptic pattern. Figures 3-32a, b, c, d present the surface, 300 mb, 200 mb and cloud observation analyses for 1200 GMT. The cyclone center which was near $32^{O}N$, $48^{O}W$ at 300 mb on the 1200 GMT, 20 June analysis appears to have shifted west southwest to $28^{O}N$, $53^{O}W$. Conventional data were not available to verify this location; however, the 6.4-6.9μ T_{bb} pattern near $30^{O}N$, $55^{O}W$ suggests that an extensive area of upward motion, due to advection of positive vorticity was lifting the air. This produced multi-layer clouds near $30^{O}N$, $55^{O}W$, and extensive cirrus over the remainder of the less than $235^{O}K$ T_{bb} area. The cloud observations in Figure 3-32d provide general support for these inferences.

3.4.1.5   0000 GMT, 22 June

The 6.4-6.9μ T_{bb} pattern superimposed on the 300 mb and 200 mb analyses for 0000 GMT, 22 June, twelve hours after Figures 3-32, is shown in Figure 3-33. Note in particular the warm ($240^{O}K$) area centered at $28^{O}N$, $53^{O}W$. This area was apparently composed of dry air which had descended and which was then advected around the 200 mb cyclone under conditions of only slight upward vertical motion. Similarly, the area of cold ($230^{O}K$) T_{bb} values centered near $22^{O}N$, $52^{O}W$ was primarily advected cloud, although this area may have been experiencing increased upward motion due to positive (cyclonic) vorticity advection on the east side of the cyclone.

(a) Surface

(b) 300 mb

(c) 200 mb

(d) Cloud observations

Figure 3-32 Surface (a), 300 mb (b), 200 mb (c) and Cloud Observations (d) Analyses for 1300 GMT, 21 June 1966. (6.4-6.9μ Channel T_{bb} superimposed.)
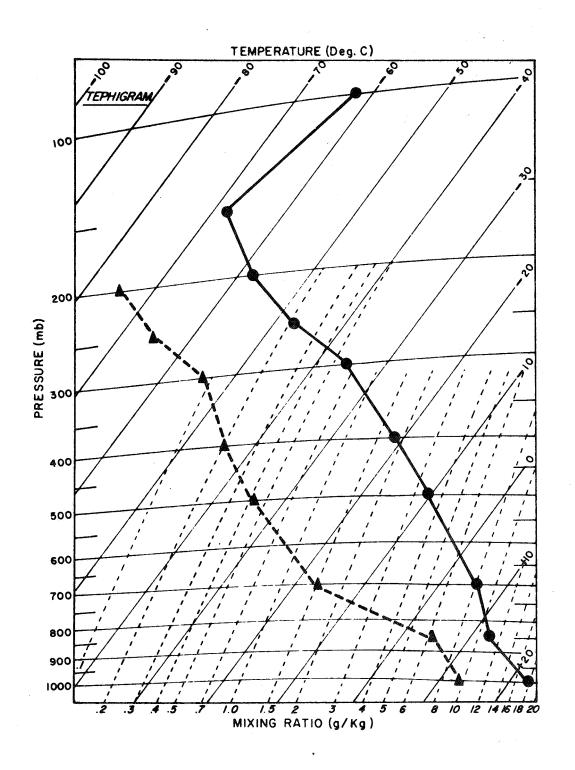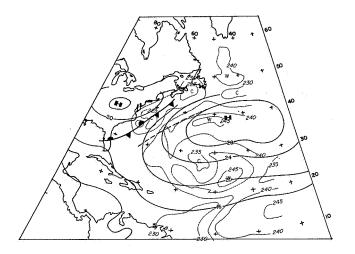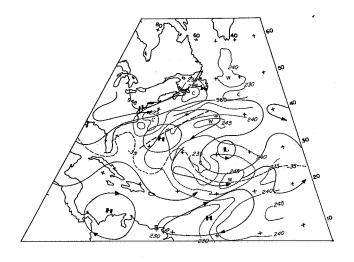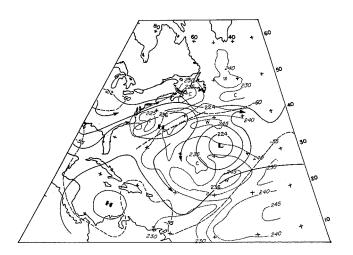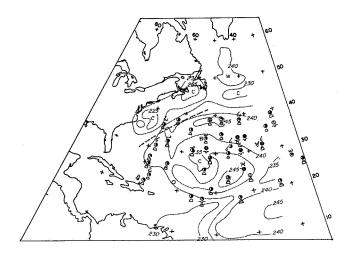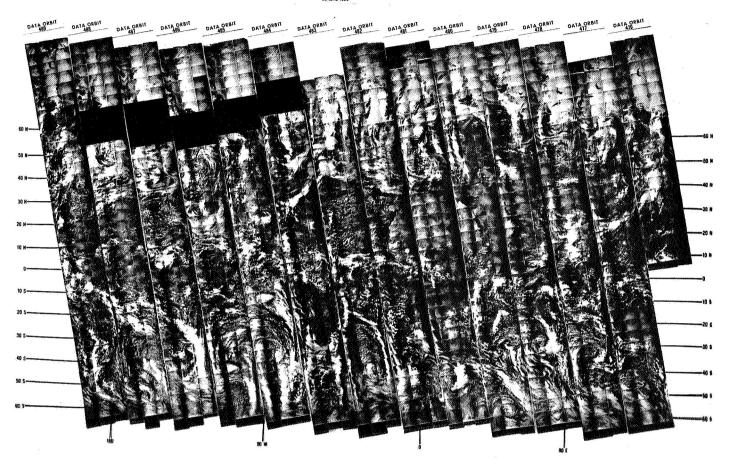
300 mb

200 mb

Figure 3-33 300 mb (a) and 200 mb (b) Analyses for 0000 GMT, 22 June 1966.
(6.4-6.9μ Channel T_{bb} superimposed.)

3.4.1.6 1200 GMT, 22 June
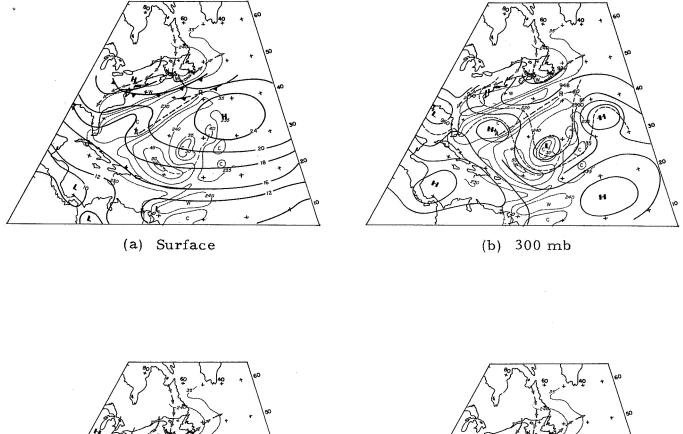
T_{bb} observations from the 6.4-6.9µ channel for approximately 1330 GMT, 22 June, are superimposed on Figures 3-34a-d, the analyses of the surface, 300 mb, 200 mb, and cloud observations for 1200 GMT, 22 June. The T_{bb} analysis shows a return to the "fish-hook" pattern present on 12 June. The return of this pattern should imply a return to an upper tropospheric field of motion somewhat analogous to that of 1200 GMT, 19 June. Comparison of the 300 mb and 200 mb analyses for the two days indicates that this was, in general, true. Primary differences were: (a) the 200 mb/300 mb cyclonic center was southwest of its position on the 1200 GMT, 19 June analyses; (b) the 200 mb/ 300 mb ridge which was near 30°N, 65°W on 1200 GMT, 22 June was narrower than 1200 GMT, 19 June; and (c) cyclonic curvature at 300 mb, near 20°N, 60°W, appears to be more pronounced at 1200 GMT, 22 June than at 1200 GMT, 19 June. These differences appear to be clearly reflected in the 6.4-6.9µ T_{bb} pattern. For example, the warm ($> 250^{\circ}$K) area at 22°N, 62°W on 22 June suggests increased descent, associated with the increased cyclonic curvature in that area.

3.4.1.7 Summary

This case study provides an illustration of the excellent potential of the 6.4-6.9µ data for aiding analyses of the fields of motion and moisture in the upper troposphere for the subtropics and tropics. The conventionally observed changes in the field of motion appear to be directly related to the 6.4-6.9µ T_{bb} patterns.

Comparisons of the cloud observation analyses and the 6.4-6.9µ T_{bb} patterns indicate that areas of T_{bb} warmer than 240°K are usually areas where scattered low clouds (type 1, fair weather cumulus) prevail, while T_{bb} areas colder than 235°K are areas of multilayered cloudiness, generally including cirrus. These observations, coupled with the streaky appearance of those 6.4-6.9µ bands which were colder than 235°K and extended poleward from the ITCZ suggest that advected cirrus (ice crystal) cloudiness may provide a means for tracking Lagrangian field of motion of the upper troposphere in the tropics and subtropics using consecutive observations from the 6.4-6.9µ channel.

(a) Surface

(b) 300 mb

(c) 200 mb
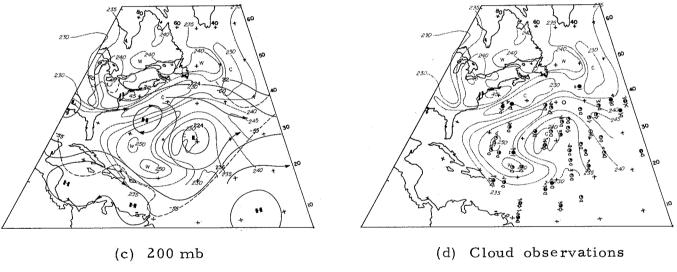
(d) Cloud observations

Figure 3-34 Surface (a), 300 mb (b), 200 mb (c) and Cloud Observations (d) Analyses for 1200 GMT, 22 June 1966. (6.4-6.9μ Channel T_{bb} superimposed).
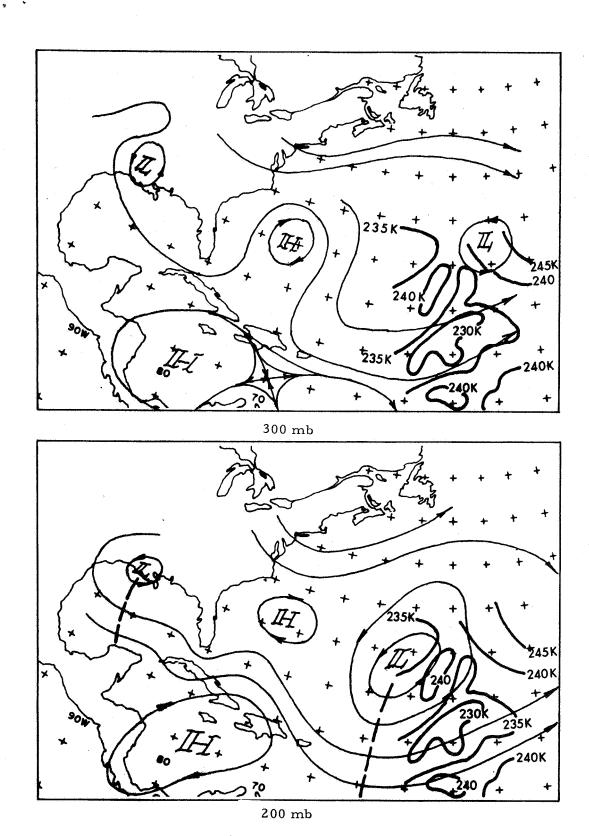
99

3.4.1.8 Tentative Model

A survey and analysis of approximately eighteen different cases of subtropical upper tropospheric baroclinic cyclones has permitted the development of a tentative, large scale geometric model of typical $6.4-6.9\mu$ T_{bb} patterns observed over the Atlantic during May, June and July and their relationship to the concurrent upper tropospheric flow pattern (see Fig. 3-35). The validity of the model pattern is reinforced when it is compared with the results of studies by Merritt (1967), which correlated 200 mb circulation and satellite cloud observations for the 1963 and 1965 June-October seasons. The jet stream-related warm area suggests strong descent centered near 40°N, 60°W and extending on a NE to SW line. The cold areas of frontal-related cloudiness, centered near 30°N, 60°W, implies both upward vertical motion and advection of high level cloudiness in the frontal zone. The "fish-hook" shaped warm area centered near 23°N, 57°W indicates moderate descent on the east side of the ridge. The cold strip extending northward from the ITCZ region is believed indicative of northward transport of high level moisture and/or cirrus from an active ITCZ region. This cirrus and/or high level moisture appears to become entrained in a subtropical jet stream, which frequently has a wind maximum south of the 200 mb cyclone centered at 25°N, 50°W.

3.4.2 Dynamical Aspects of Tropical Cyclone Development

Merritt and Wexler (1967) and Merritt (1967) have shown that the rate of change in size of the cirrus canopy over a developing tropical cyclone can be directly related to: (a) the field of motion (horizontal and vertical) in and around the cirrus canopy; and (b) the percentage area distribution of penetrative cumulus "hot towers" in the storm area. Merritt (1967) further showed, in the case of Alma, 1966 that there was an observable difference in the size of the visible and "window" canopies. As an extension of this work we have made a brief examination of the development of hurricane Celia, 1966 as observed by various Nimbus sensors, including the $6.4-6.9\mu$ H_2O channel and Gemini X.

100
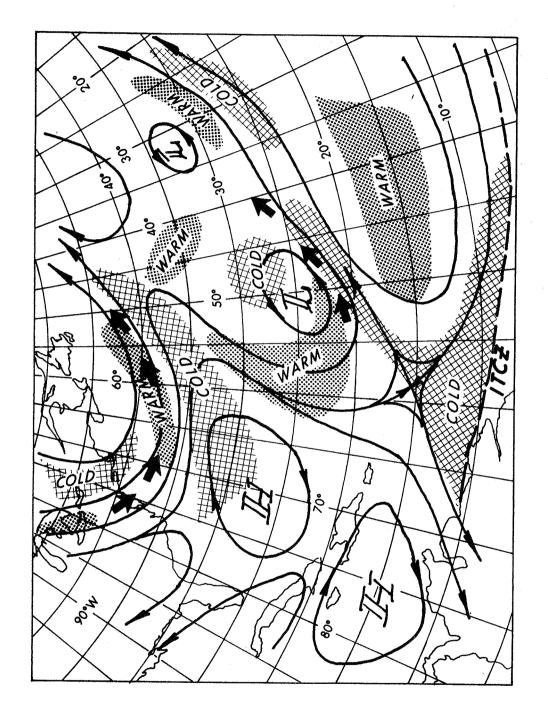
Figure 3-35   Tentative Model of 6.4-6.9μ T_{bb} Patterns of Summer Baroclinic Cyclones over the Atlantic.

3.4.2.1 General Discussion

Hurricane Celia was first identified as a depression about 200 miles north-northeast of the Leeward Islands at 1200 GMT on 13 July 1966. An interesting quote from the U.S. Navy Annual Tropical Storm Report for 1966 states:

"It is interesting to note that prior to 13 July 1966, there was no history of a well defined easterly wave or similar synoptic features as is usually the case in the formation of a tropical storm."

This fact implies that the original impetus for Celia may have been in the middle and upper troposphere as discussed by Sadler (1967) for the Pacific and Merritt (1967) for the Atlantic. Merritt used the term "composite origin" to describe these storms.

Following the initial development, Celia degenerated to a disturbed area on 15 July. This situation persisted until late on 18 July. The two day interval 18-19 July during which major changes occurred in intensity, forms the subject for this brief study.

3.4.2.2 18 July 1966

On 18 July, a Nimbus II APT photograph, Figure 3-36, received at Goddard Space Flight Center, presented a dramatic view of the incipient storm area. Two features pertinent to this discussion are present: (a) the apparent wave disturbance marked A just southeast of Hatteras and the relatively disorganized cloud mass marked B. The cloud area at B will evolve into a tropical storm in 24 hours and a hurricane in 48 hours.

Digital mappings of $6.4\text{-}6.9\mu$ channel and $10\text{-}11\mu$ channel T_{bb} 's for 18 July at approximately 1600 GMT are presented as Figure 3-37. A corresponding photo-facsimile strip is also included as part of Figure 3-37. Note the cold $6.4\text{-}6.9\mu$ and $10\text{-}11\mu$ T_{bb} values corresponding to the bright cloud areas shown in Figure 3-36 at points A and B. Cloud heights inferred from the $10\text{-}11\mu$ T_{bb} values are about 30,000 feet at both points A and B. The $6.4\text{-}6.9\mu$ T_{bb} over point B is $220^{\circ}K$ compared with $225^{\circ}K$ at point A. This difference suggests that a high relatively thin cirrus layer exists over B. Careful examination of Figure 3-36 indicates such a thin cirrus layer may be present.

Surface isobaric and 200 mb streamline analyses for 1200 GMT, 18 July shown in Figure 3-38 present a rather dramatic contrast. The rather intense appearing (in the satellite photograph), formative wave cyclone at point A appears to be associated with a very weak surface low with a 1015 mb central pressure. The area around the potential Celia disturbance at point B indicates nothing but a broad, very flat, surface pressure gradient. A streamline analysis might indicate some cyclonic curvature. Prior analyses had forced a rather marked easterly-wave pattern into the area.

At 200 mb in Figure 3-38, the wave cyclone pattern at point A appears to be closely related to an area of strong cyclonic curvature and shear which is perhaps more like what one might expect from the satellite photograph in Figure 3-36. At point B there are several solutions to the analysis, the anticyclonic outdraft appears reasonable both from the radiosondes and the satellite photograph.

3.4.2.2.1 Discussion

The relative positions of the 200 mb cyclone near Hatteras and the potential Celia disturbance at point B appears to be common in developing cyclones. Merritt (1967) showed that both ITCZ and so-called "composite-origin"[†] hurricanes in 1963 and 1965 had a 200 mb cyclone within 15 degrees to the north in the case of ITCZ-type developments and within 5 to 7 degrees in the case of "composite-origin" developments. The significant dynamic implication of this juxtapositioning — is not clear but we may speculate two roles; (a) to provide increased mass divergence from the developing lower tropospheric cyclone and (b) by, in certain areas, providing increased synoptic scale vertical motion through positive vorticity advection, hence a more favorable climate for the development of penetrative cumulus over the northern portion of the storm area. The $6.4-6.9\mu$ observations, by permitting observation of both vertical motion and advection, provides some basis for speculation on which of the mechanisms might be operative in this case. We observed $6.4-6.9\mu$ T_{bb} values of $245^{\circ}K$ just west of the apparent wave cyclone at point A. Prior studies of jet streams and the subtropical baroclinic upper cyclones in

---

[†] "Composite-origin" hurricanes usually appear to form north of $20^{\circ}N$. They are frequently related to an upper tropospheric cyclone centered in a layer near 200 mb.
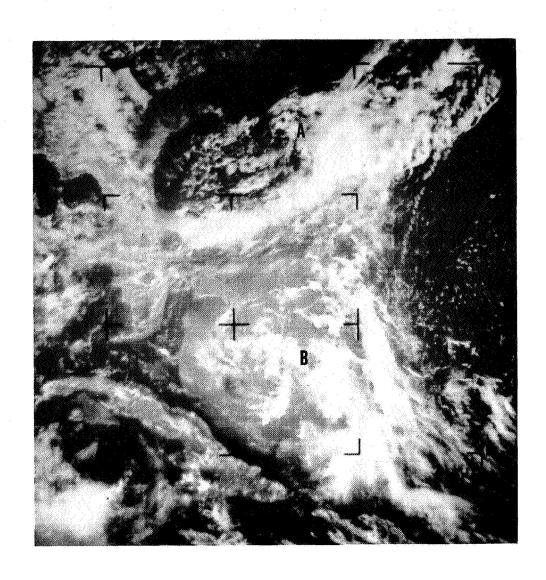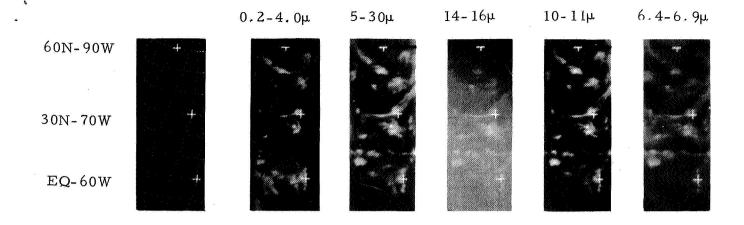
Figure 3-36 Nimbus II APT Photograph 1620 GMT, 18 July 1966.

| 0.2-4.0μ | 5-30μ | 14-16μ | 10-11μ | 6.4-6.9μ |

60N-90W

30N-70W

EQ-60W
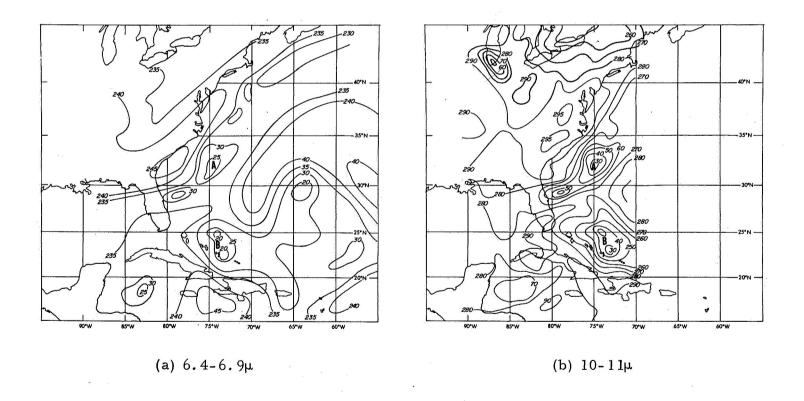
(a) 6.4-6.9μ

(b) 10-11μ

Figure 3-37   Analysis of 6.4-6.9μ (a) and 10-11μ (b) Channel T_{bb}'s, 1610 GMT, 18 July 1966.

105
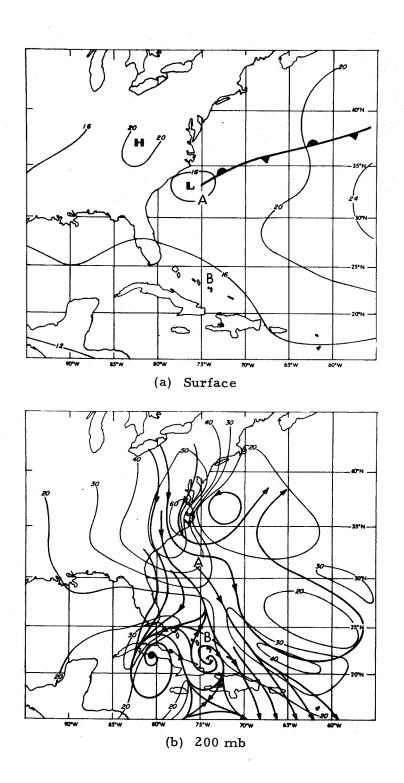
(a) Surface

(b) 200 mb

Figure 3-38 Surface (a) and 200 mb (b) Analyses, 1200 GMT, 18 July 1966.

Sections 3.1 through 3.4 have shown that T_{bb} values of 245°K and greater are invariably associated with regions of strong descent associated with divergence and/or anticyclonic vorticity advection.

3.4.2.3   19 July

On 19 July the satellite observations show a vastly different picture than that existing on 18 July. Figure 3-39 presents a Gemini X photograph which includes most of the western edge of Celia. Florida and the U.S. East coast are near the horizon. Note the large heavy cirrus area which appears to be in the area of the relatively weak scattered area marked point B on the 18 July Nimbus photograph in Figure 3-36.

The digital T_{bb} mappings of the 6.4-6.9μ and 10-11μ channels shown in Figure 3-40 presents the overall view of the developing Celia system. Note the large increase in area of the 220°K T_{bb} values on the 6.4-6.9μ mapping and a similar increase in 230°K T_{bb} values on the 10-11μ mapping. Another significant change is to be seen in the apparent southeast movement of the warm > 240°K area west of the heavy clouded region.

Surface isobaric and 200 mb streamline analyses for 1200 GMT, 19 July (Fig. 3-41) indicate changes which are parallel to those observed by the satellite. The surface analysis shows a 1010 mb low centered near 26°N, 76°W. This is directly in the area of the 215°K T_{bb}† area on the 6.4-6.9μ mapping and close to the 220°K area on the 10-11μ mapping.

At 200 mb the deep zone of cyclonic curvature and shear appears to extend farther southward and one might expect strong positive vorticity advection into the area of heavy cloudiness. The Celia depression still appears related to a small anticyclonic outflow although the data are not sufficient to confirm this analysis interpretation. Southwest flow at 200 mb over the area centered near 28°N, 71°W is probably advecting cirrus, produced over the Celia depression, toward the 200 mb ridge line which lies along 66°W between 29°N and 34°N. Descent on the east side of this ridge probably evaporates most, but not all, of the advected cirrus. Therefore, the measured 6.4-6.9μ T_{bb} values were near 240°K.

---

† Calculations shown in Section 2.4.3 for a model atmosphere indicate that 215°K temperatures would be found with a blackbody cloud at about 13 km.
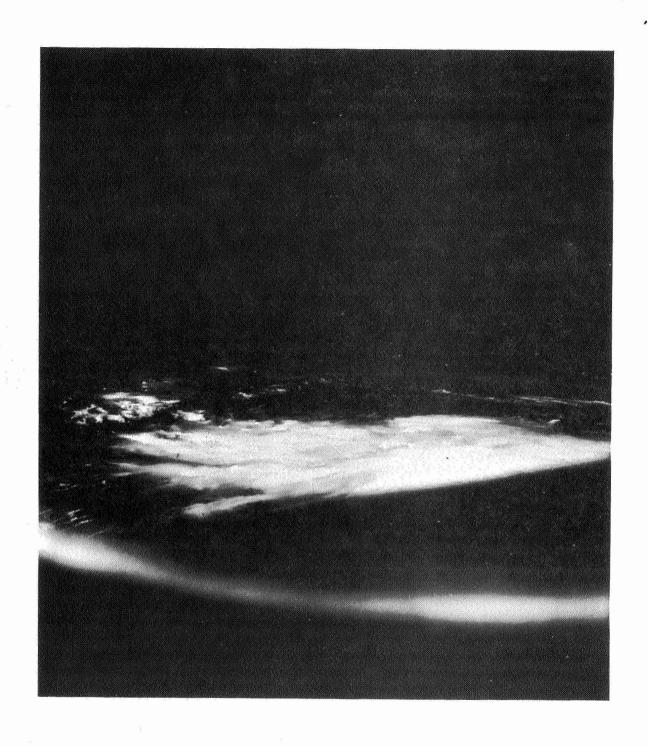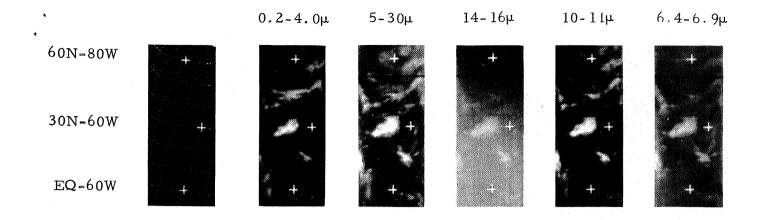
Figure 3-39   Gemini X Photograph, 19 July 1966.

| | 0.2-4.0μ | 5-30μ | 14-16μ | 10-11μ | 6.4-6.9μ |

60N-80W

30N-60W

EQ-60W
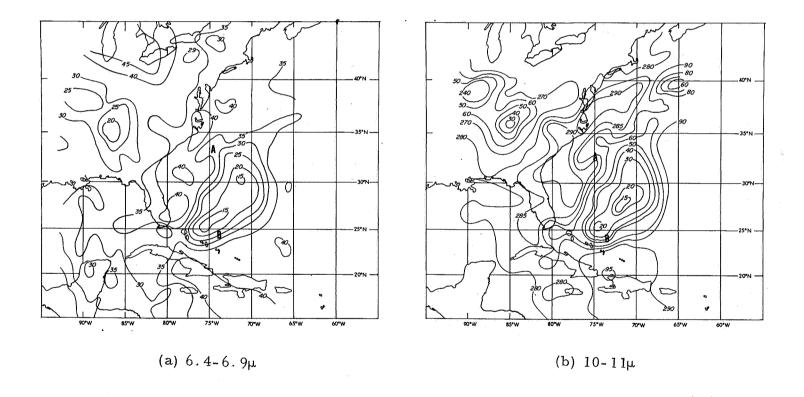
(a) 6.4-6.9μ

(b) 10-11μ

Figure 3-40   Analysis of 6.4-6.9μ (a) and 10-11μ (b) Channel T_{bb}'s, 1545 GMT, 19 July 1966.
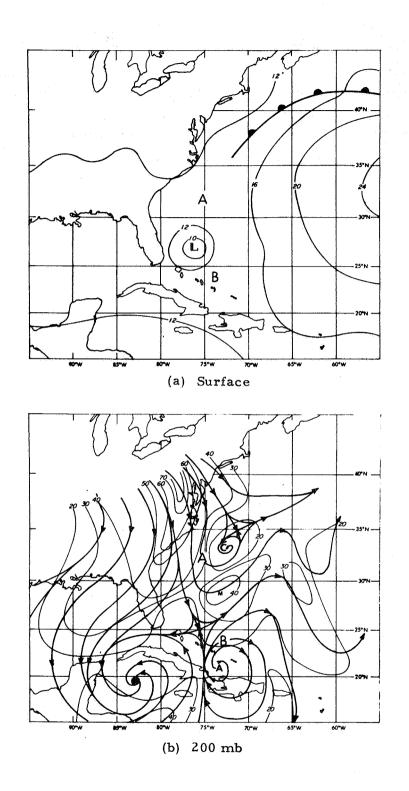
(a) Surface

(b) 200 mb

Figure 3-41 Surface (a) and 200 mb (b) Analyses, 1200 GMT, 19 July 1966

3.4.2.3.1 Discussion, 19 July

In the 24 hour period from ~1200 GMT, 18 July to ~1200 GMT, 19 July extensive changes in cloud cover occurred over the area encompassing the potential Celia development. These changes were of the type usually associated with increasing intensity in a tropical storm, i.e., dramatic increases in apparent cirriform coverage. There is a suggestion, however, that the radical increase in cirrus over areas north of about 28°N was due more to the vertical motion associated with positive vorticity advection from the deep 200 mb trough along the coast, rather than from the direct vertical transport with penetrative cumulus in the Celia disturbance centered near 25°N.

If this speculation is valid (only extensive radar observations can establish the existence and organization of the penetrative cumulus) then the rebirth of Celia is more of an extratropical development than tropical.

3.4.2.4 Summary

In this case, example of the rebirth and development stages of hurricane Celia, the 6.4-6.9μ information proved useful in the following ways:

1.   Establishing that a thin cirrus canopy existed over the Celia area on 18 July

2.   Defining the regions where strong downward vertical motion occurred on 18 July

3.   Defining the horizontal extent and maximum height (13 km) of the cirrus canopy on 19 July

4.   Providing indications of the subsidence on the west side of the potential Celia development region on 19 July.

Satellite observation of hurricane and tropical storms are, in general confined to the patterns presented by the cirrus canopy, the eye (if there is one), peripheral clearing and spiral bands. The 6.4-6.9μ information permits a better description of the cirrus canopy and the intensity of peripheral subsidence regions. These parameters appear significant to interpretation of storm intensity and future history.

4. SUMMARY

4.1 Basic Sensor Considerations

4.1.1 6.4-6.9μ H_2O Channel

The 6.4-6.9μ H_2O channel "sees" vertical distributions of water vapor, temperature and cloud above about 3 km. The measured T_{bb} value is a complex integral of all of these factors. Empirical analyses and sample computations suggest that T_{bb} values below $235^{\circ}K$ are found only over extensively layered clouds, including cirrus. T_{bb} values greater than $240^{\circ}K$ appear in areas with only low cloud below 3 km. The T_{bb} range $235^{\circ}K$-$240^{\circ}K$ seems to occur in areas where independent cirrus layers are common. These cirrus layers are observed from the ground but are not "obvious" in Nimbus II AVCS photographs, MRIR "window or visible" observations or revealed by radiosonde soundings.

4.1.2 14-16μ CO_2 Channel

The 14-16μ CO_2 channel "sees" vertical distributions of temperature and middle and high clouds. The primary operational application of this channel appears to be in its ability to detect the dynamic "warmings" in the lower stratosphere which are often found in association with intense baroclinic systems, i.e., jet streams and associated cyclonic systems. The cloud influences, limit the use of the 14-16μ observation for general stratospheric absolute temperature determination.

4.2 Operational Meteorological Applications

4.2.1 Extratropical Jet Streams

The 6.4-6.9μ H_2O and 14-16μ CO_2 channels provide information on atmospheric structure not easily obtained in other ways. Because water vapor and ice crystal concentrations are sensitive to vertical and horizontal motion at middle and upper tropospheric levels, the 6.4-6.9μ channel observations provide a good indication of atmospheric motions. Warm 6.4-6.9μ banded patterns correlate very well with

113

specific areas of the jet stream axis. When the $6.4-6.9\mu$ shows a marked warm band pattern and the $14-16\mu$ shows a marked large scale temperature gradient, it may be possible for unique determination of an intense jet stream location.

4.2.2 Baroclinic Cyclones

Development of an intense baroclinic cyclone is accompanied by marked changes in the $6.4-6.9\mu$ and $14-16\mu$ T_{bb} patterns. In the early stages of development the $6.4-6.9\mu$ warm bands were confined to the immediate jet stream area. As the development proceeded toward the cut-off stage at 500 and 300 mb, the $6.4-6.9\mu$ warm areas became larger, reflecting subsidence over more extensive areas. The $14-16\mu$ channel shows a similar though less marked development pattern. The "cut-off" stage is marked by an isolated warm T_{bb} area near the center of the 500/300 mb cyclone.

4.2.3 Upper Tropospheric Cyclones in the Subtropics

Upper tropospheric baroclinic cyclones which commonly occur over the subtropical oceanic anticyclones are clearly delineated in the $6.4-6.9\mu$ T_{bb} patterns. A characteristic "fish-hook" pattern of T_{bb} values greater than $240^{o}K$ extends around the west side of the cyclone area. Strips of cold T_{bb} values ($< 240^{o}K$) extend around the equatorward sides of the cyclone area where maximum winds are found in the Sub Tropical Jet stream (STJ). When the equatorial 200 mb anticyclone is split, cold T_{bb} strips appear between the ITCZ and the STJ.

4.2.4 Dynamic Aspects of Hurricane Development

The $6.4-6.9\mu$ H_2O data provide useful information for diagnosis of some aspects of tropical cyclone development. These aspects are, in general, restricted to two areas: (a) determination of the extent of the cirrus canopy and (b) determination of the location and general magnitude of peripheral subsidence areas.

5. RECOMMENDATIONS

The studies of the $6.4-6.9\mu$ H_2O and $14-16\mu$ CO_2 data from the Nimbus II MRIR have revealed features of the data which are directly applicable to operational meteorology. Similarly many questions have been raised which require further investigation. The most pertinent of these are listed in the following paragraphs.

5.1 Thin Cirrus

The $6.4-6.9\mu$ H_2O channel appears to be influenced by relatively thin cirrus layers which are not obvious in either the television (AVCS or APT), visible $(0.2-4.0\mu)$ or window $(10-11\mu)$ observations. This property greatly reduces or eliminates the use of the $6.4-6.9\mu$ data to determine water vapor distribution. A study program is required which would include aircraft, radiometersonde ascents and ground based LIDAR observations during satellite passage over ostensibly clear or cirrus covered areas. The objective of the study would be the determination of the range of cirrus particle size and number densities existing in various areas and measurement of their influence on the $6.4-6.9\mu$ H_2O radiances. This study would be extremely valuable to definition of the influence of satellite-observed cloudiness, television, visible and infrared radiometric, on earth albedo and related heat flux computations.

5.2 Jet Streams

The $6.4-6.9\mu$ H_2O data do reveal warm bands which are often directly associated with the vertical motions of the jet stream. On the other hand, warm areas were observed without jet stream activity. The shapes of the warm bands seem to be indicative of the type of atmospheric field of motion related to the warm area, i.e., narrow bands were frequently associated with jet streams while broad, rounded zones were associated with anticyclone descent areas. More study is required to uniquely define the shapes associated with jet streams. A potential approach using the conjoint of the $6.4-6.9\mu$ H_2O and the $14-16\mu$ CO_2 seems to provide a unique jet stream location in cases of intense extratropical jets. A series of analyses of winter time MRIR observation over the United States or Europe may provide a definitive solution.

5.3 Baroclinic Cyclones

The vertical motions associated with upper tropospheric baroclinic cyclones in both the extratropics and subtropics is dramatically revealed in the $6.4-6.9\mu$ data. Intense extratropical cyclonic developments are also well marked in the $14-16\mu$ data. A study is recommended to examine the possibilities for delineation of tropospheric/ stratospheric dynamic interaction processes. This study should address itself to the suggestion that tropospheric forcing is responsible for some types of stratospheric warmings.

A second recommended study would utilize the capabilities of the $6.4-6.9\mu$ H_2O observations to assist in description of the upper troposphere of the subtropics. The field of motion in this area appears to exert a major influence on tropical storm intensification as well as on the overall transport processes to and from the equatorial regions.

5.4 Multi-Channel Applications

Presentation of the MRIR $0.2-4.0\mu$, $10-11\mu$ and $6.4-6.9\mu$ data in a three-color presentation appears useful for definition of clear areas, e.g. the sea surface temperature study (Contract No. NASW-1157, being conducted at ARA) uses this approach to delimit areas where HRIR-derived sea surface temperature will not be cloud contaminated. A study of applications of this approach to the Earth Resources Satellite is recommended.

A further application of the three-color presentation technique is in the satellite cloud wind direction determination problem. Current techniques examine the cirrus blow-offs from cumulonimbus. The use of multichannel presentation, including $6.4-6.9\mu$ data may permit definition of more extensive cirrus plumes or small plumes not apparent in the television photographs.

5.5 CAT Area Delineation

The apparent ability of the $6.4-6.9\mu$ H_2O channel to define baroclinic areas provides a partial basis for CAT area delineation. A study of CAT occurrences and CAT indices, e.g. $V\Delta\alpha/\Delta z$, in warm band regions might permit useful identification of CAT areas through the use of future $6.4-6.9\mu$ observations.

116

REFERENCES

Bjerknes, V. and H. Solberg, 1921: "Meteorological Conditions for the Formation of Rain," Geofysiske Publikasjoner, Oslo, 2, 60 pp.

Bradbury, D. and E. Palmen, 1953: "On the Existence of a Polar Front at the 500 mb Level,' Bulletin of the American Meteorological Society, 34, pp. 56-62.

Brundidge, K.C., 1958: "A Preliminary Study of Eleven Project Jet Stream Flights; 1956-1957 Phase," Final Report Wind Field Near the Tropopause, Texas A and M, Dept. of Oceanography and Meteorology, Contract No. AF 19(604)-1565, pp. 86-108.

Danielsen, E.F., 1964: Project Springfield, Contract No. DA-49-146-XZ-079, Defense Atomic Support Agency.

Endlich, R.M., 1953: "A Study of Vertical Velocities in the Vicinity of Jet Streams," Journal of Meteorology, 10(6), pp. 407-415.

Endlich, R.M. and G.S. McLean, 1956: "The Structure of the Jet Stream Core," Journal of Meteorology, 14, pp. 543-552.

Fleet Weather Facility, 1967: Annual Tropical Storm Report - 1966, U. S. Navy, Jacksonville, Florida, OPNAV Report 3140-9.

Hsieh, Y.P., 1950: 'On the Formation of Shear Lines in the Upper Atmosphere," Journal of Meteorology, 7(6), pp. 382-387

Kennedy, J.S., 1966: An Atlas of Stratospheric Mean Isotherms Derived from TIROS VII Observations, NASA Report No. X-622-66-307, Goddard Space Flight Center.

Ludlam, F.H., and L.I. Miller, 1959: Research in the Properties of Cloud Systems, Final Report, Contract No. 6(514)-1292, AFCRL.

Mastenbrook, H.J., 1966: Water Vapor Observations at Low, Middle and High Latitudes During 1964 and 1965, NRL Report No. 6447, Naval Research Laboratory.

Merritt, E.S. and D. Chang, 1966: Synoptic Studies of Satellite Measurements in the 15μ CO_2 Band, Final Report, Contract No. N189(188)-59192A, Allied Research Associates, Inc.

Merritt, E.S., 1967: Atlantic Upper Tropospheric Circulations and Tropical Cyclone Development, Final Report, Contract No. N 189(188)-60598A, Allied Research Associates, Inc.

Merritt, E.S. and R. Wexler, 1967: "Cirrus Canopies in Tropical Storms," Monthly Weather Review, 95(3), pp. 111-120.

Moller, F. and E. Raschke, 1964: Evaluation of TIROS III Radiation Data, NASA Contractor Report No. CR-112, National Aeronautics and Space Administration.

Murray, R., 1956: "Some Features of Jet Streams as Shown by Aircraft Observations," Great Britain Meteorological Office, Geophysical Memoirs, No. 97.

Nordberg, W., A.W. McCulloch, L.L. Foshee, and W.R. Bandeen, 1966: Preliminary Results from Nimbus II, NASA Report No. X-620-66-349, Goddard Space Flight Center.

Oliver, V.J., R.K. Anderson and E.W. Ferguson, 1964: "Some Examples of the Detection of Jet Streams from TIROS Photographs," Monthly Weather Review, 92(10), pp. 441-448.

Orgill, M.M., 1960: An Investigation into the Relationship of Monthly Circulation Indices and Anomalies to Typhoon Development in the Western Pacific, Sci. Report. No. 2, Contract AF 19(604)-7229, Hawaii Inst., Geoph. Rept. No. 11.

Palmen, E., 1958: "Vertical Circulation and Release of Kinetic Energy During the Development of Hurricane Hazel into an Extratropical Storm," Tellus, 10(1), pp. 1-23.

Palmer, C.E., 1953: "The Impulsive Generation of Certain Changes in the Tropospheric Circulation," Journal of Meteor., 19(1), pp. 1-9.

Ramage, C.S., 1959: "Hurricane Development," Journal of Meteor., 16(3), pp. 227-237.

Reed, R.J. and E.F. Danielsen, 1959: "Fronts in the Vicinity of the Tropopause," Archiv fur Meterologie, Geophysik und Bioklimatologie, Serie A, Wien, 11, pp. 1-17.

Reiter, E.R., 1963: Jet Stream Meteorology, The University of Chicago Press, Chicago and London, 515 pp.

Reiter, E.R. and L.F. Whitney, 1965: <u>Subtropical or Polar Front Jet Stream,</u> <u>Project WISP</u>, Report No. 1, Contract No. Cwb-10879, Dept. of Atmospheric Science, Colorado State University.

Riehl, H., 1948: "Jet Stream in Upper Troposphere and Cyclone Formation," <u>Trans-</u> <u>actions of the American Geophysical Union,</u> <u>29</u>(2), pp. 175-186.

Riehl, H. and S. Teweles, Jr., 1953: "A Further Study on the Relation Between the Jet Stream and Cyclone Formation," <u>Tellus,</u> <u>5</u>(1), pp. 66-79.

Riehl, H., 1962: <u>Jet Streams of the Atmosphere</u>, Tech. Report No. 32, Dept. of Atmospheric Science, Colorado State University.

Rogers, C.W.C., and P.E. Sherr, 1966: <u>Toward the Dynamic Interpretation of</u> <u>Satellite-Observed Extratropical Vortical Cloud Patterns,</u> Final Report, Contract No. Cwb-11123, Allied Research Associates, Inc.

Sadler, J.C., 1962: <u>Utilization of Meteorological Satellite Cloud Data in Tropical</u> <u>Meteorology</u>, Meteorological Research Note, AFCRL and Proceedings of the International Symposium on Rocket and Satellite Meteorology.

Sadler, J.C., 1967: <u>The Tropical Upper Tropospheric Trough as a Secondary Source</u> <u>of Typhoons and a Primary Source of Tradewind Disturbances</u>, Final Report, Contract No. AF 19(628)-3860, Hawaii Institute of Geophysics, University of Hawaii.

Sawyer, J.S., 1955: "The Free Atmosphere in the Vicinity of Fronts: Analysis of the Observations by the Meteorological Research Flight 1950-1952," Great Britain Meteorological Office, <u>Geophysical Memoirs</u>, No. 96.

Sawyer, J.S., 1958: "Temperature, Humidity and Cloud Near Fronts in the Middle and Upper Troposphere," <u>Quarterly Journal of the Royal Meteorological</u> <u>Society,</u> 84(362), pp. 375-388.

Sherr, P.E., and C.W.C. Rogers, 1965: <u>The Identification and Interpretation of</u> <u>Cloud Vortices Using TIROS Infrared Observations</u>, Final Report, Contract No. Cwb-10812, ARACON Geophysics Company.

Teweles, S., Jr., 1954: "Jet Stream Detail with Respect to Other Meteorological Factors," American Meteorological Society, <u>Proceedings of the Toronto</u> <u>Meteorological Conference,</u> September 1963, pp. 188-192.

(Valley, S. L., Ed.), 1965: Handbook of Geophysics and Space Environments, AFCRL, Office of Aerospace Research, USAF.

Vuorela, L. A., 1957: "A Study of Vertical Velocity Distribution in Some Jet Stream Cases Over Western Europe," Geophysica, 6(2), Helsinki, pp. 68-90.

Warnecke, G., 1967: The Remote Sensing of Stratospheric Temperatures and Some Results from the Nimbus II Satellite Experiment, NASA Report No. X-622-67-471, Goddard Space Flight Center.

Whitney, L. F., et al., 1966: "On Locating Jet Streams from TIROS Photographs," Monthly Weather Review, 94(3), pp. 127-138.

Widger, W. K., Jr., 1964: "A Synthesis of Interpretations of Extratropical Vortex Patterns as Seen by TIROS," Monthly Weather Review, 92(6), pp. 263-282.

APPENDIX A

A.1 Correlation of Upper Tropospheric Moisture with Water Vapor Channel T_{bb}'s

Moller and Raschke (1964) have proposed the joint use of the H_2O and "window" channel data to obtain mean relative humidities of the upper troposphere. It appears probable, based on the preceding discussion, that the data from the H_2O channel alone may be correlated to the integrated water vapor amount (precipitable water) in the upper troposphere, at least in cloud free regions. Precipitable water is dependent on mixing ratio. Unlike relative humidity, mixing ratio is a quasi-conservative property of the atmosphere.

Furthermore, since $\tau_\lambda(z)$ and $\partial\tau_\lambda/\partial z(z)$ are both dependent on the vertically (downward) integrated value of mixing ratio (i.e. precipitable water), it would seem appropriate to seek a correlation between T_{bb} and upper tropospheric precipitable water. Such a correlation can only be established through a statistical study involving a large number of data points. In this section, the results of a limited correlation study are presented. While no claim is made for the absolute validity of these results, the study does indicate that a useful correlation exists.

It has been demonstrated that, for a "clear" atmosphere with 6.4-6.9 T_{bb}'s higher than $\sim 240°K$:

1. Measured T_{bb} is independent of the moisture and temperature distributions below ~ 700 mb.

2. Measured T_{bb} is dependent on the distribution of moisture and temperature in the mid and upper troposphere.

3. The high variability of upper tropospheric mixing ratios, compared to the variability of upper tropospheric temperatures (in midlatitudes), suggests that differences in T_{bb} reflect mainly upper tropospheric moisture differences, rather than differences in temperatures.

4. Regions which show pronounced positive temperature departures in the upper troposphere are often the result of both warming and drying, taking place on a large scale in the upper troposphere, probably produced by strong subsidence. Since both warming and drying result in a higher T_{bb}, this class of phenomena would tend to enhance the correlation.

A.2 Choice of Upper Tropospheric Layer

An upper tropospheric layer was defined. Its lower boundary was dictated by the fact that moisture and temperature distributions below 700 mb have little or no effect on the measured T_{bb}. The upper boundary was dictated by the availability of upper tropospheric moisture measurements. Radiosonde moisture measurements, even if available, are seldom accurate above 400 mb. The layer chosen was thus defined as that between 400 and 700 mb.

A.3 Procedure

Four days of data were arbitrarily chosen for analysis. These included two days in May (19 and 20 May) and two days in June (26 and 27 June). The 1200 GMT radiosonde data over the United States for these days were used to compute the 700-400 mb precipitable water, W_{7-4}, where:

$$W_{7-4} = \frac{1}{gD} \int_{700}^{400} q(p)\, dp$$

where

$$
\begin{aligned}
q &= \text{gravitational acceleration}\\
D &= \text{density of liquid water}\\
q(p) &= \text{mixing ratio (gms/gm) at pressure p}\\
W &= \text{precipitable water (cm)}\\
p &= \text{pressure (dynes/cm}^2\text{)}
\end{aligned}
$$

The computed value of W_{7-4} at the several stations were then tabulated against the corresponding measured T_{bb}'s, determined from the analyzed digital mappings.

It should be pointed out that, in the tabulation of the data, no attempts were made to delete cloud contaminated data, nor to take into account the time difference between the radiosonde and satellite data.

A.4 Results

Figure A-1 shows the result, in the form of frequency distribution. The measured T_{bb}'s have been divided into increments of $5\,^{\circ}K$. W_{7-4} are increments of 0.5 cm. These initial results show that a linear regression line of the form:
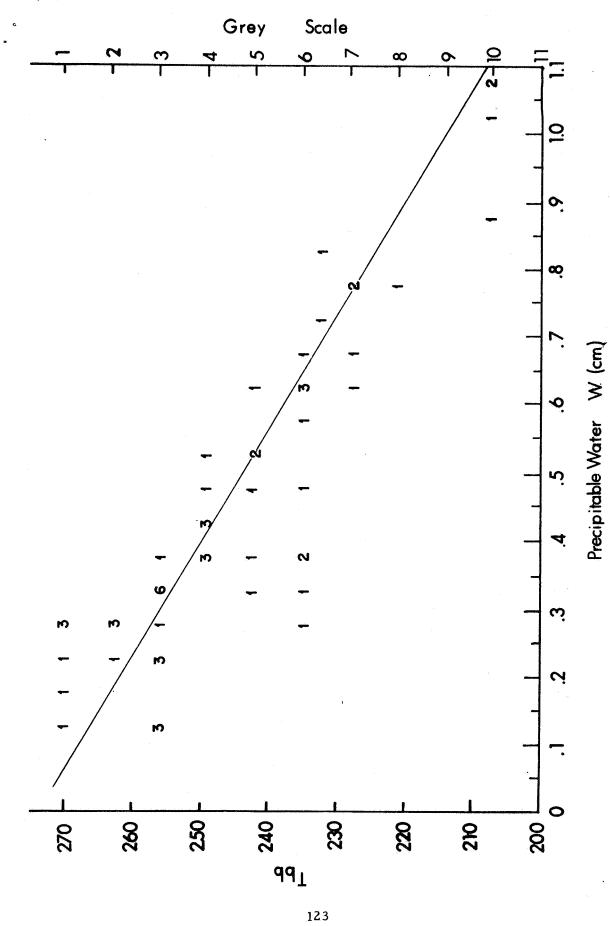
Figure A-1   Scatter Diagram of Precipitable Water vs. 6.4-6.9µ Channel T_{bb}

123

$$W_{7-4} = K \, T_{bb} + C$$

where

K and C = constants

may be fitted to the data for the range of T_{bb} values above $240^{\circ}K$. For values below $\sim 240^{\circ}K$; the effect of cloud contamination seems to become significant but a correlation still exists.

APPENDIX B

B. 1 Experiments in Multichannel Analysis and Data Display by
      Photographic Means

The significance of multichannel analysis of the MRIR data in meteorological applications is evident in the discussions presented in this report. As a consequence, experiments were conducted to determine the feasibility of performing multichannel analyses and data presentation by photographic means. It was found that a color separation technique applied to the analog pictorial presentations of the data can result in a color presentation which facilitates cloud type discrimination.

Figure B-1[†] shows an example of the color separation technique applied to the $0.2-4\mu$, $10-11\mu$ and $6.4-6.9\mu$ channels. The figure shows the grey scale analog presentations of the three channels of the MRIR, together with the geographical reference grid. The color presentation (enlarged) prepared by the three color separation technique is also shown. The following channel-filter pairs were used;

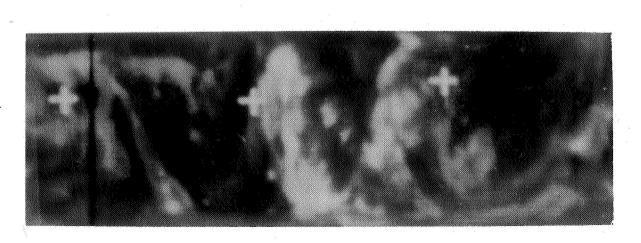| Channel	Filter
$0.2-4\mu$	Green
$10-11\mu$	Blue
$6.4-6.9\mu$	Red

The color presentation was made on Kodak Ektacolor professional paper. Exposure of this paper to red light results in a bluish shade (cyan), while exposures to blue and green light result in yellow and magenta respectively.

The transparencies used in the preparation of the color presentation were essentially "negatives" of the pictorial format shown, i.e., white (bright) areas, such as the major cloud band evident in all three channels, were essentially opaque in the transparencies. Consequently such areas appear whitish-yellow. (The residual yellow tint resulted from the longer exposure time employed with the blue/$10-11\mu$ channel combination needed to achieve color contrast of other features.) On the other hand, when the grey scale contrast is more evident in one channel, then the color of the feature in reproduction is determined primarily by the combination of the colors used in the other two channels. For instance, the cirrus, apparently present only in

---

†   Only a limited number of copies of this report have a color reproduction. Interested parties may contact NASA, GSFC for color reproductions.

Black - Clear
Green - Low Cloud
Red - Thin Middle/High Cloud
Yellow White - Heavy High Cloud (Probably in thick layers)

RED FILTER   6.4 - 6.9 μ

BLUE FILTER   10 - 11 μ

GREEN FILTER   0.2 - 4.0 μ

COLOR
PROCESS

GEO.
GRID

Figure B-1   Three Color Presentation of Channels 1, 2 and 5 Nimbus II Medium Resolution Infrared Experiment (MRIR), 1200 LMT, 20 June 1966.

the 6.4-6.9μ channel, along the southern edge of the major cloud band, is rendered yellowish-red in the color presentation. This color resulted from the "addition" of yellow (blue filter/10-11μ combination) and magneta (green filter/0.2-4μ combination). The resulting color contrast renders the cirrus much more evident.

When the color presentation is compared with the individual channel displays, it may be seen that the three color separation technique holds promise of being a relatively simple method for joint analysis and presentation of multichannel data.

Currently foreseen applications for the color technique include:

1. determination of high cloud, low and clear areas
2. possible delineation of cirrus "blow-off" areas for use in defining wind directions.

In (1), application has already been made to delineation of clear areas for sea surface temperature determination. In this application the three-color approach is accomplished in the computer without the preparation of an actual color print. The application posed in (2) is a possible extension of current National Environmental Satellite Center attempts at wind direction determination using cirrus plumes. The 6.4-6.9μ channel might permit "seeing" the downwind extension of the plume not visible in the photographs.

APPENDIX C

CLEAR AIR TURBULENCE DETECTION USING
NIMBUS II 6.4-6.9μ OBSERVATIONS

C.1   Introduction

Clear Air Turbulence (CAT) continues as a significant problem to both commercial and military aircraft operators. Many approaches toward solution of the problems have been proposed. These approaches fall into two categories:

1.   Delineation or forecasting of CAT areas, using standard radiosonde or other meteorological data to compute various indices which appear to be correlated with CAT.

2.   Airborne detection techniques employing radar, lasers, infrared and/or microwave radiometers, etc.

Ultimately, an effective CAT solution may very well use a combination of the best techniques, or systems, developed from work in both of these categories. On the other hand, existing studies with regard to the use of standard data for forecasting CAT areas suggest that the spacing of radiosonde stations, even over the United States or Europe, will seldom provide accurate delineation of many of the CAT-probable areas.

Early in 1964, Merritt and Wexler (1964) of Allied Research Associates, Inc. proposed a conceptual radiometric system for inflight detection of Clear Air Turbulence (CAT). The proposed system would have utilized radiometric observations in the 6.3μ H_2O spectral region to determine (1) thermal gradients and microscale thermal "cells," and (2) horizontal variations in water vapor. It was hypothesized that CAT should be related to these parameters.

Recent experimental programs, Mather (1967) and Anonymous (1967) using radiometers operating in the 15μ CO_2 band, have shown that the proposed radiometric approach to CAT detection has definite promise. While providing a more representative thermal measurement, the use of the CO_2 band, precludes the use of water vapor as an additional parameter in delineating regions likely to have CAT. The 6.4-6.9μ H_2O observations from the Nimbus II meteorological satellite (described in some detail later) have re-emphasized the validity of the hypothesis that water vapor variations may be valuable indicators of potential CAT areas.

C.2 Turbulence Considerations

The 26 June 1966 case study in Section 3.2.1 presents Figure C-1 which clearly depicts the location of the marked warm dry regions detected by the $6.4\text{-}6.9\mu$ channel. A search of CAT reports provided by Mr. DeVer Colson of ESSA and by United Airlines, for June 1966, produced two significant observations on 26 June within the warm $6.4\text{-}6.9\mu$ band. The locations of these reports are overlayed on Figure C-1. The location of these reports within the warm, active descent, region indicated by the $6.4\text{-}6.9\mu$ observation, is encouraging. Nevertheless, it certainly does not establish a generally useful positive relationship. The significance of these observations appeared to increase, however, when they were compared to the distribution of quantities, which have been shown to be correlated with CAT occurrences. This comparison was made along a cross section intersecting the region where the aircraft reports existed.

Many different CAT correlations and indices have been proposed over the past few years. One of the most promising is the product of (1) the change in wind direction with height $(\Delta\alpha/\Delta z)$ and (2) the magnitude of the wind speed (v). Endlich and McLean(1965) have shown a correlation of .67 using selected Project Jet Stream data. Figure C-2 presents an analysis of $(v\Delta\alpha/\Delta z)$ for the southern cross section located in Figure C-1. This section is in the entrance region of the jet, and passes very close to the locations of the aircraft observed CAT. Note the aircraft observed CAT on Figure C-1. Note the excellent spatial agreement between warm $6.4\text{-}6.9\mu$ areas and the values of $(v\Delta\alpha/\Delta z)$ greater than $.3$ deg. $\sec^{-1}$. Endlich and McLean showed that the probability for CAT occurrences in the moderate (10 ft $\sec^{-1}$) and severe (20 ft $\sec^{-1}$) ranges increases markedly above $.3$ deg. $\sec^{-1}$.

C.3 Discussion

The 26 June case analysis presented in Section 3.2.1 presents some features that appear to be of significant interest to the CAT delineation problem. The dynamics associated with these features are only poorly understood. The $6.4\text{-}6.9\mu$ channel "sees" in unclouded areas, an integral of temperature and moisture for the layer between about 4 km and 13 km. Sample calculations of blackbody temperature (T_{bb}) values in the warm areas, i.e., T_{bb} values greater than $245°K$, show that these
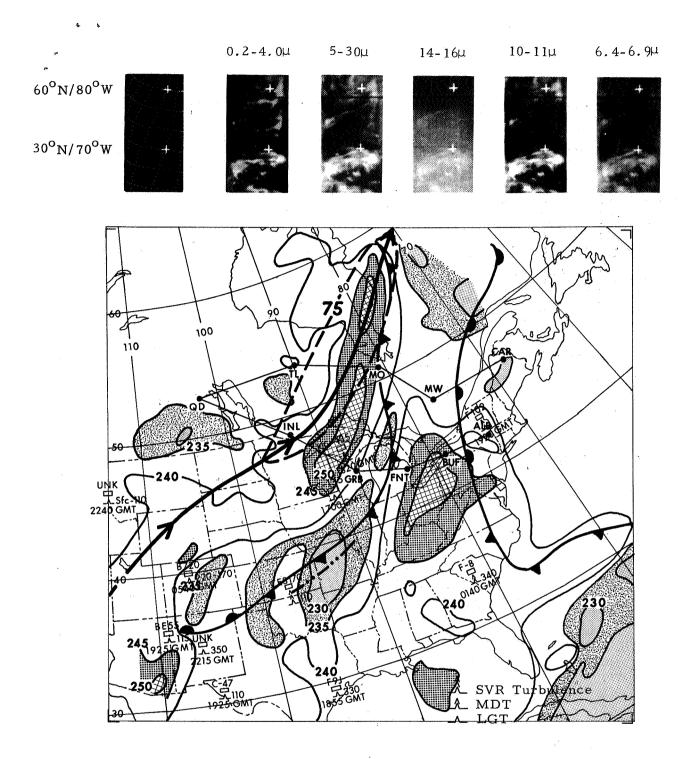
Figure C-1   Analysis of 6.4-6.9μ Channel T_{bb} at 1600 GMT, 26 June 1966. (The superimposed surface fronts and jet streams are adjusted to the time of the satellite pass. Thin lines between stations show the axis of cross section referred to in the text. CAT reports superimposed.)
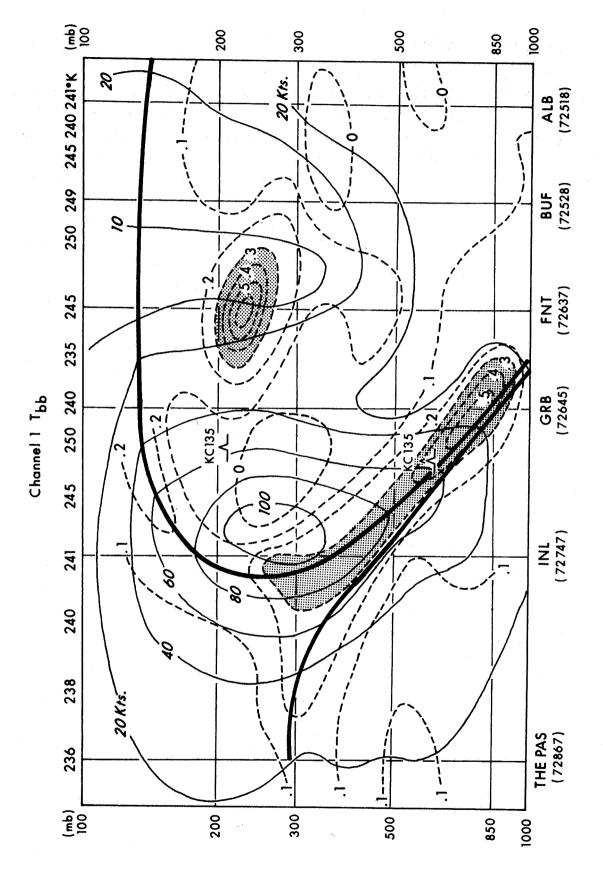
131

Figure C-2   Analysis of v(Δα/Δz) for Cross Section Shown in Figure C-1.

values can only be achieved in a very dry, subsidence type atmosphere. This type of atmosphere occurs in three ways: (a) in slow descent conditions such as are found on the southeast side of major northern hemisphere high pressure systems, (b) in areas where there is strong turning of the wind with height which leads to differential advection of warm and cold air and, therefore, differential vertical velocities, (an example of this type of occurrence appears between FNT and BUF where rapid turning of relatively light winds occurs above 250 mb) and (c) in the area of the jet stream, where dry stratospheric air intrudes into the troposphere through the baroclinic zone as described by Vuorela (1957), Sawyer (1955) and others. The last two (b) and (c) types of subsidence conditions are of interest to the CAT problem.

In terms of possible turbulence mechanics, we must consider what pertinent processes may be occurring in the areas of $6.4\text{-}6.9\mu$ warm bands such as that shown in Figure C-1. Maintenance of turbulence requires that

$$\left(\frac{\partial v}{\partial z}\right)^2 > \frac{g}{\theta} \cdot \frac{\partial \theta}{\partial z}$$

where v is the vector wind and θ is potential temperature. In the strong sloping baroclinic zones associated with the polar front jet stream, $\partial v/\partial z$ is often quite large. It is hypothesized then that strong descent (intrusion of dry stratospheric air) may have two consequences: (a) it may locally increase the thermal gradient (thereby the vertical shear) and (b) it may increase, at least locally, the static stability. If these occur concurrently, in a local sense, CAT will be improbable. If, however, an imbalance occurs where $(\partial v/\partial z)^2$ increases more rapidly than the static stability a CAT-probable condition will occur. The $6.4\text{-}6.9\mu$ observation cannot define when these imbalances will occur. They may, however, define the general areas within which they are most probable.

Detailed study of various turbulence indices in the area of warm bands observed by the $6.4\text{-}6.9\mu$ H_2O channel may provide some answers to the problems speculated on in the previous paragraphs. It may also lead to a technique for improved operational delineation of potentially turbulent regions, based either on the radiation data (when they become operationally available) or perhaps even from conventional observations.

133

REFERENCES

Anonymous, 1967: "The Search for Clear Air Turbulence," Skyline, 25(3), pp. 43-47.

Endlich, R.M. and G.S. Mclean, 1965: "Empirical Relationships Between Gust Intensity in Clear Air Turbulence and Certain Meteorological Quantities," Journal of Applied Meteorology, 4(2), pp. 222-227.

Mather, G.K., 1967: Flight Evaluation of an Infrared Spectrometer as a Clear Air Turbulence Detector, National Research Council of Canada, Aeronautical Report LR-477.

Merritt, E.S., and R. Wexler, 1964: "Radiometric Detection of Clear Air Turbulence," Presented at the Fifth Conference on Applied Meteorology, Atlantic City, N.J., Published in Proceedings of Second Symposium on Remote Sensing at University of Michigan, April 1964.

Sawyer, J.S., 1955: "The Free Atmosphere in the Vicinity of Fronts - Analysis of Observations by the Meteorological Research Flight (1950-52)," Great Britian Meteorological Office, Geophysical Memoirs No. 96.

Vuorela, L.A., 1957: "A Study of Vertical Velocity Distributions in Some Jet Stream Cases Over Western Europe," Geophysics, Helsinki, 6(2), pp. 68-90.